Doctoral Thesis

Solution Self-Assembly of Dendritic-Linear Block Copolymers into Inverse Bicontinuous Cubic Phases

Yunju La

Department of Chemistry

Graduate School of UNIST

2018

Solution Self-Assembly of Dendritic-Linear Block Copolymers into Inverse Bicontinuous Cubic Phases

Yunju La

Department of Chemistry

Graduate School of UNIST

Solution Self-Assembly of Dendritic-Linear Block Copolymers into Inverse Bicontinuous Cubic Phases

A thesis/dissertation
submitted to the Graduate School of UNIST
in partial fulfillment of the
requirements for the degree of
Doctor of Philosophy

Yunju La

12/08/2017 of submission
Approved by

_____

Advisor
Ja-Hyoung Ryu

Solution Self-Assembly of Dendritic-Linear Block Copolymers into Inverse Bicontinuous Cubic Phases

Yunju La

This certifies that the thesis/dissertation of Yunju La is approved.

12/08/2017 of submission

_____

Advisor: Prof. Ja-Hyoung Ryu

_____

Prof. Kyoung Taek Kim: Thesis Committee Member #1

_____

Prof. Hoi Ri Moon: Thesis Committee Member #2

_____

Prof. Young S. Park: Thesis Committee Member #3

_____

Prof. Sung You Hong: Thesis Committee Member #4;

Abstract

Inverse bicontinuous cubic (IBC) phases of lipids and their colloidal forms, referred to as cubosomes, possess internal networks of water channels. These crystalline mesophases have attracted considerable attention owing to their unique nanospace for the encapsulation of guest molecules. Block copolymers (BCPs) are the versatile building block that can be used to generate well-defined three-dimensional structures. Direct solution self-assembly of amphiphilic BCPs into IBC phases is a promising new strategy for creating high crystalline porous polymer materials.

In this dissertation, I describe the self-assembly of dendritic-linear BCPs into IBC phases. The dendritic isomer of second-generation benzyl ether dendrons with six water-soluble peripheral poly(ethylene glycol) (PEG) chains was synthesized. These isomers were converted into macroinitiators for the atom-transfer radical polymerization (ATRP) of styrene. The asymmetric block ratio and bulky dendritic blocks drove the BCPs to form colloidal IBC phases. The internal structures of the resulting polymer cubosomes show crystalline lattices over the long range including primitive cubic, double diamond, and gyroid symmetries depending on the architecture of the dendritic hydrophilic block. Functional groups on the surface of the bilayer membranes were introduced via the coassembly of dendritic-linear block copolymers and linear block copolymers that possess an amino- or thiol-functionalized PEG block. The surface functionalized polymer cubosomes showed successful internalizing of large protein complex such as horseradish peroxidase (HRP).

Furthermore, I devised a new method of solution self-assembly by diffusion of water to the block copolymer solution, which results in the unperturbed formation of mesoporous monoliths with large pore networks weaved in crystalline lattices. The internal networks of large pores within the mesoporous monoliths used as a platform to accommodate guest molecules such as streptavidin and mCherry. The monolith is also used as a scaffold for the synthesis of three-dimensional (3D) skeletal structures of crystalline titania and hierarchically mesoporous silica.

The phase of the self-assembled structures of the branched-linear BCPs was controlled ranging from bilayer structures of positive curvature to inverse mesophases by adjusting the solvent used for self-assembly. Dimethylformamide (DMF) is a pseudo-theta solvent for polystyrene, in which PS adopts a reduced chain dimension compared to the value of the same PS dissolved in dioxane. The morphological transition of self-assembled structures from vesicles to IBC structures and inverse hexagonal phases were fully observed as a result of an increase in the portion of DMF in the solvent mixture. A similar transition also occurred in the formation of mesoporous monoliths.

The internal structure of polymer cubosomes exhibits double networks of water channels. However, the interfacial topology of polymer cubosomes renders one of the two non-intersecting pore networks to be inaccessible to diffusion. The connectivity of the open surface pores was studied by 3D

tomogram of the polymer cubosomes. This topological feature forces the external guests to enter only into the open cubic channel network within the polymer cubosomes. By backfilling the polymer cubosomes with the silica and titania precursor, the single network cubic structure was replicated from the IBC structures.

Contents

List of figures

Figure 1-17. Scheme of two representative synthesis routes for ordered mesoporous materials. (a) Soft-templating method. (b) Hard-templating (nanocasting) method (Ref. 44).

Figure 1-18. Schematic representation of sample fabrication and SEM image of a metal gyroid. The isoprene block (blue) is removed and is then back-filled with gold (yellow). The final structure is obtained by plasma etching (Ref. 50).

Figure 1-19. Anatomy of the structural color-producing nanostructures in (a-c) lycaenid and (d-f) papilionid butterflies. (a, d) Light micrograph of wing cover scales. (b, e) SEM and (c, f) TEM images of surfaces and nanostructures of scales. Insets show simulated (b) (111), (c) (310), (e) (110), and (f) (211) projection of single gyroid structures.

Figure 2-1. Chemical structures and schematic diagrams of dendritic-linear block copolymers and their self-assembly. (a) Chemical structures of block copolymers 1_n and 2_n constructed from the two isomers of benzyl ether dendrons that possess peripheral PEG chains at the 3,5-positions (1_n) and 3,4-positions (2_n) of the outer phenyl groups, and 3_n and 4_n built from dendritic blocks that consist of two peripheral 3,4,5-PEG-benzyl ether units at the 3,5 (3_n) and 3,4 (4_n) positions of the central benzyl unit. The subscript *n* denotes the DP of the PS block. (b) A schematic representation of the self-assembly of dendritic-linear block copolymers into polymer cubosomes in dilute aqueous solution. The lattice diagrams at the bottom show bicontinuous cubic internal structures of the polymer cubosomes (*Im3m*, *Pn3m* and *Ia3d*) investigated in this study. For clarity, the bilayers that surround the water channels are omitted. The green- and red-colored regions indicate two non-intersecting networks of water channels within the bicontinuous structures.

Figure 2-2. TEM images of self-assembled structures from the suspension solution of 1_{185}. (a) Flat lamella structures. (b) Folded lamella structures.

Figure 2-3. (a) Size distributions and (b) autocorrelation functions of the suspensions of 1_{217} and 2_{213}. The average diameter of 1_{217} and 2_{213} were 6.2 μm (dispersity 0.27) and 7.9 μm (0.22), respectively.

Figure 2-4. Representative SEM and TEM images of the polymer cubosomes. (a) TEM images showing the internal structure of the polymer cubosomes of 1_{217} (left). The magnified view of the internal structures and the fast Fourier transform (FFT) (inset) show a cubic (*Im3m*) lattice viewed in the [111] direction (right). (b) TEM images of polymer cubosomes of 2_{213}. The right image shows the view of a double diamond (*Pn3m*) lattice viewed in the [001] direction and the FFT of the image. (c, d) Low-magnification SEM images of polymer cubosomes of 1_{217} (c) and 2_{213} (d). (e) SEM image of the

polymer cubosome of 1_{217} showing a spherical morphology and the perforated shell enclosing the internal bicontinuous structure. (f) SEM images of the polymer cubosomes of 2_{213}. The inset shows a magnified view of the surface pores (scale bar, 100 nm).

Figure 2-5. (a, b) SEM and (c, d) TEM images showing the perforated lamellar shell structures of the polymer cubosomes of 1_{217}. Arrows indicate the thicknesses of the lamellar shells (14.7 nm in c, 14.9 nm in d).

Figure 2-6. Structural analysis of the polymer cubosomes. (a) HR-SEM image of the bicontinuous cubic internal structure of the polymer cubosome of 1_{217} having a primitive cubic (*Im3m*) lattice. The internal structures were observed from the fractured polymer cubosomes during the sample preparation. The views in the [100], [110] and [111] directions are highlighted by white squares. (b) HR-SEM images of a double diamond (*Pn3m*) internal structure of the polymer cubosomes of 2_{213}. Views in the [111] and [100] directions are highlighted by white squares. The inset shows a view in the [110] direction (scale bar, 200 nm). (c) The SAXS result of the dried polymer cubosomes of 1_{217}, which indicates the primitive cubic (*Im3m*) lattice (lattice parameter, a = 93.4 nm). (d) The SAXS result of the dried polymer cubosomes of 2_{213} shows the double diamond (Pn3m) lattice (a = 49.5 nm). (e) N_2 adsorption-desorption isotherms of the dried polymer cubosomes of 1_{217} (filled circles) and 2_{213} (open circles) measured at 77 K. a.u., arbitrary units; STP, standard temperature and pressure.

Figure 2-7. BJH pore size distributions of polymer cubosomes of (a) 1_{217} and (b) 2_{213}.

Figure 2-8. Surface pressure to molecular area (π-A) isotherms of a linear block copolymer and dendritic-linear block copolymers at 300 K.

Figure 2-9. Polymer cubosomes of 3_{223}. (a, b) HR-SEM images showing the internal double-gyroid structures of the polymer cubosome of 3_{223} viewed in the [111] (a) and [110] (b) directions. (c) SAXS results of dried polymer cubosomes of 3_{223}. Peaks were assigned to Ia3d symmetry (a = 82.3 nm). (d) N_2 adsorption-desorption isotherms of the dried polymer cubosomes of 3_{223} measured at 77 K (BET surface area 99 $m^2\ g^{-1}$, pore volume 1.16 $cm^3\ g^{-1}$).

Figure 2-10. SAXS result of the dried polymer cubosomes of 4_{222} assigned to the bicontinuous cubic (Pn3m) lattice.

Figure 2-11. TEM images of self-assembled polymer vesicles of PEG_{45}-PS_{270}.

Figure 2-12. (a-c) TEM images and (d) size distributions of polymer cubosomes of 1_{217} observed from the quenched suspensions at various water contents (a, 15%, b, 30%, and c, 50%). Size distributions measured by DLS experiments indicate that the particle sizes are not correlated to the water content during self-assembly.

Figure 2-13. SEM images of polymer cubosomes of 1_{232} and 2_{245}. (a, b) SEM images showing the emergence of inverse hexagonal phase in the polymer cubosomes of 1_{232}. (c) The polymer cubosomes of 2_{245}. (d) The inverse hexagonal phase within the polymer cubosomes of 2_{245}.

Figure 2-14. SEM and TEM and Gas adsorption profile of self-assemble structures of 1_{232} in the presence of homo PS (10% w/w) as an additive. (a) SEM image showing spiral-shape aggregates. (b) SEM images showing the inverse hexagonal phase (up) and the cross section of hexagonally packed channels (down). (c) TEM images of aggregates. The inset shows hexagonally packed channels. (scale bar = 50m) (d) TEM image showing the long-range order of inverse hexagonal phase. (e) N2 physisorption isotherms measured at 77 K. (BET surface area 27.3 $m^2 g^{-1}$, pore volume 0.12 $cm^3 g^{-1}$.). The inset shows the BJH pore size distribution (the mean pore diameter 17.4 nm).

Figure 2-15. Representative SEM images of the polymer cubosomes of 1_{217}/NH_2-PEG_{45}-PS_{210} (10% w/w).

Figure 2-16. Surface-functionalized polymer cubosomes obtained from the coassembly of 1_{217} and NH_2–PEG_{45}–PS_{210} (10% w/w). (a) SEM image and (b) HR-SEM image showing the surface pores of the polymer cubosomes. (c, d) TEM images showing the internal structures of the polymer cubosomes. (e) 3D reconstructed images of CLSM of the polymer cubosomes after the reaction with Rho-NHS.

Figure 2-17. Surface-functionalized polymer cubosomes. (a) CLSM images of polymer cubosomes of 1_{217} and NH_2–PEG_{45}–PS_{210}/SH–PEG_{45}–PS_{210} (equimolar mixture, 8% w/w) after selectively labelling SH groups with F-MI (λ_{ex} = 492 nm, λ_{em} = 518 nm, left (ex, excitation; em, emission)) and NH_2 groups with Rho-NHS (λ_{ex} = 564 nm, λ_{em} = 589 nm, center). The merged image confirmed the presence of both functional groups in the same polymer cubosome (right). (b) CLSM image of fluorescein-labelled streptavidin within the biotin-labelled polymer cubosomes of 1_{217}/ NH_2–PEG_{45}–PS_{210} (10% w/w). (c) Time course plots of the absorption of radical cation of $ABTS^{\bullet+}$ oxidized by free (black line) and HRP–cubosomes (red line) of 1_{217}/SH–PEG_{45}–PS_{210} (7% w/w). Free HRP or HRP–cubosome was mixed with a solution containing 1.6 mM ABTS and 0.125 mM H_2O_2 in phosphate buffer (pH 7.4). The absorbance was measured at 740 nm. The green trace indicates the background absorption of ABTS and H_2O_2 in the absence of HRP.

a primitive cubic lattice (*Im3m*) and double diamond lattice (*Pn3m*). (e) SEM image for the monolith of 1_{217} at the [100] projection of *Im3m*.

Figure 3-6. Time-course SEM analysis of mesoporous monoliths from 2_{213} after quenching at (a) 10 min, (b) 15 min, (c) 20 min, (d) 25 min, (e) 30 min, and (f) 60 min during SDEMS (scale bars, 500 nm). The regular structures of *Pn3m* were gradually evolved.

Figure 3-7. (a) The photograph shows the polymer monolith of 2_{213} on a glass slide (25 cm^2). (b) The cross-section view of SEM indicates the thickness of the monolith is ~ 400 μm. (c) The top-surfaces of macroporous portions showing perforated bilayers. The inset shows a regular pore arrangement. (d) All other portions showed the regular structures of *Pn3m*, as shown in the SEM image.

Figure 3-8. SAXS data and SEM images of the co-assembled polymer monoliths of 2_{213} / NH_2-PEG_{45}-PS_{210} (93:7 w/w in dioxane). (a) The SAXS result of the co-assembled polymer monoliths shows double diamond (*Pn3m*) lattice (a = 63.2 nm). (b) SEM image of a cross section of the functionalized monoliths. (c) High-magnification SEM image of internal structure shows a double diamond lattice viewed in the [111] direction.

Figure 3-9. (a) Schematic illustration of surface functionalization of the monolith of 2_{213}/NH_2-PEG_{45}-PS_{210} (93:7 w/w in dioxane) with protein complexes. The biotinylated monolith was complexed with fluorescein isothiocyanate-labelled streptavidin homo-tetramer. mCherry-biotin fluorescent protein was further assembled with the streptavidin on the surface of the monolith. Excess proteins was removed by rigorous washing procedures. (b) CLSM images of the biotinylated monolith of 2_{213}/NH_2-PEG_{45}-PS_{210} (93/7 w/w) after binding of fluorescein isothiocyanate-streptavidin (λ_{em} = 519 nm, left of panel). Subsequent binding of biotinylated-mCherry fluorescent protein (λ_{em} = 610 nm, center of panel) showed cherry-colored fluorescence. Two images were merged (right of panel). The image was taken from 127×127×34 μm (width/height/depth) region near the top surface of the monolith. Scale bars, 40 μm. (c) Axial intensity profile of CLSM images along the optical axis was recorded from x, y, z image stacks, revealing the distributions of proteins.

Figure 3-10. 3D skeletal inorganic nanostructures replicated from the monolith of 2_{213}. The monoliths of 2_{213} were used as templates for the fabrication of 3D skeletal porous inorganic nanostructures. The monoliths were immersed in each precursor solutions and excess solutions were removed before the calcination. mS-SiO_2 was schematically drawn to represent the hierarchically porous structure in which hexagonally ordered nanopores were incorporated into the skeletons consisting the self-supporting networks.

Figure 3-11. Photocatalytic porous TiO_2 nanostructures replicated from the monolith of 2_{213}. (a, b) SEM images of S-TiO_2 synthesized within the mesoporous monolith of 2_{213}. Scale bars, 300 nm. The inset in (a) shows a photograph of S-TiO_2 monolith. (scale bar, 5 mm). (c) EDS (Energy-dispersive X-ray spectroscopy) mapping of S-TiO_2 replicated from the monolith of 2_{213}. Scale bars, 50 nm. (d) X-ray diffraction data of the anatase TiO_2 skeletons consisting of the skeletal nanostructures. The inset shows a TEM image of the lattice structures of anatase TiO_2 skeletons. (e) Comparison of the photocatalytic activity of S-TiO_2 with that of bulk TiO_2 under the same experimental conditions. The y axis indicates the optical density of the methylene blue solution, whereas the x axis indicates the ultraviolet light irradiation time.

Figure 3-12. (a-b) Bright filed TEM images and (c) high-angle annular dark-field scanning transmission electron microscopy (HAADF-STEM) image of S-TiO_2. (d-f) SEM images of S-TiO_2 showing the shift of bicontinuous phase to single diamond network. (g) The SAXS result of S-TiO_2 shows single diamond (*Fd3m*) phase.

Figure 3-13. N_2 adsorption-desorption isotherms of S-TiO_2.

Figure 3-14. Hierarchically porous SiO_2 skeletal nanostructures replicated from the monolith of 2_{213}. (a) SEM image of the cross-section view of mS-SiO_2. The inset shows a photograph of the SiO_2 replica (scale bar, 5 mm). (b, c) SEM images of mS-SiO_2. Scale bars, 500nm (a, b) and 100nm (c). (d–f) TEM images of mS-SiO_2 replicated from the monolith of 2_{213}. Scale bars, 100 nm (d, e) and 20nm (f). (g) SAXS results of the monolith of 2_{213} (black, a = 51.7 nm) used as the template and mS-SiO_2 (red, a = 75.8 nm). The peaks were assigned to *Pn3m* (black line) and *Fd3m* (red line) symmetries, respectively. (h) SAXS result of hexagonally ordered nanopores residing in the mS-SiO_2 (a = 3.58 nm). (i) N_2 adsorption–desorption isotherms of mS-SiO_2.

Figure 3-15. (a) Bright field TEM and (b) STEM image of the mS-SiO_2 replicated from the monolith of 2_{213} showing the hexagonally ordered nanopores within the skeleton. (c, d) SEM images mS-SiO_2 of at various projections showing shifted networks to form single diamond phase.

Figure 3-16. (a) Micro- and (b) meso-pore size distributions by the Horvath-Kawazoe (HK) and BJH methods on a N_2 adsorption-desorption isotherm of the mSiO_2-*Fd3m*.

Figure 4-1. (a) A simple phase diagram of self-assembly of $PEG550_3$-PS_n from dioxane solutions. (b–e) SEM images of the polymer cubosomes of (b) $PEG550_3$-PS_{211} (f_{PEG} = 7.5%) and (d) $PEG550_3$-PS_{231}

(f_{PEG} = 6.9 %). The insets show the perforated surface layer of the polymer cubosomes (scale bars, 200 nm). SEM images of the internal structures of the polymer cubosomes of (c) $PEG550_3$-PS_{211} showing [100] projection of *Im3m* and (e) $PEG550_3$-PS_{231} showing [111] projection of *Pn3m*. (f) TEM image of the polymersomes of $PEG550_3$-PS_{177} (f_{PEG} = 8.9 %). (g) SEM image of the hexasomes of $PEG550_3$-PS_{283} (f_{PEG} = 5.6 %). The inset shows the internal H_{II} structure (scale bar, 200 nm).

Figure 4-2. SAXS results of (a) $PEG550_3$-PS_{211} (*Im3m*, a = 82.5 nm), (b) $PEG550_3$-PS_{231} (*Pn3m*, a = 47.9 nm), and (c) $PEG550_3$-PS_{283} (H_{II}, a = 28.8 nm).

Figure 4-3. SEM and TEM images of self-assembled structures of $PEG550_3$-PS_{211} by using THF as a common solvent. (a and c) Fully developed polymer cubosomes as a majority. (b and d) Polymersomes and sponge phase particles as minor structures.

Figure 4-4. (a–e) TEM and SEM images of the self-assembled structures of $PEG550_3$-PS_{177} prepared from the dioxane/DMF mixtures at varying ratios: (a) 0 vol% DMF (vesicle), (b) 2 vol% DMF (vesicles, polymer cubosomes), (c) 5 vol% DMF (*Im3m* + *Pn3m*), (d) 8 vol% DMF (*Pn3m*), and (e) 15 vol% DMF (H_{II}). The inset in (e) shows the internal hexagonal structures (scale bar, 200 nm).

Figure 4-5. TEM images of self-assembled structures of PEG2000-PS_{180} in various mixtures of dioxane and DMF: (a) 0 vol% DMF, (b) 2 vol% DMF. (c) 5 vol% DMF, and (d) 8 vol% DMF.

Figure 4-6. (a–c) SEM images of the internal structures of the polymer cubosomes of $PEG550_3$-PS_{177} prepared from (a) 5 vol% DMF in dioxane showing the [100] projection of *Im3m*, (b) 8 vol% DMF in dioxane showing the [111] projection of *Pn3m*, and (c) 15 vol% DMF in dioxane showing the cross-section view of the inverse hexagonal phase. (d–f) SAXS results corresponding to the polymer cubosomes in (a–c): (d) Mixed phase of *Im3m* and *Pn3m* symmetries (a = 61.5 nm (*Im3m*) and 48.0 nm (*Pn3m*)); (e) *Pn3m* symmetry (a = 46.0 nm); (f) *P6mm* (H_{II}) symmetry (a=27.7 nm).

Figure 4-7. (a, c, e) Low-resolution SEM images of the cross-section of the mesoporous films of $PEG550_3$-PS_{177} prepared by the SDEMS method using DMF/dioxane mixtures as a common solvent. (a) 0 vol% DMF, (c) 10 vol% DMF, and (e) 15 vol% DMF. (The insets show the top layer of the films; scale bars, 500 nm). (b, d, f) High-resolution SEM images of the films of (a), (c), and (e). (b) Stacked lamellae, (d) *Pn3m* symmetry (a=50.6 nm), and (f) *P6mm* symmetry (a=29.3 nm).

Figure 4-8. SAXS results of the mesoporous monoliths of $PEG550_3$-PS_{177} prepared by the SDEMS method from (a) 10 vol% DMF in dioxane (*Pn3m*, a = 50.6 nm), and (b) 15 vol% DMF in dioxane

(*P6mm*, a = 29.3 nm).

Figure 4-9. Schematic illustration for preparation of the mesoporous film of $PEG550_3$-PS_n.

Figure 5-1. SAXS results of the polymer cubosomes of (a) $PEG550_3$-PS_{150} (*Im3m*, a = 60.7 nm) and (b) $PEG550_3$-PS_{168} (*Pn3m*, a = 45.2 nm). The insets show first diffraction peak position of *Im3m* and *Pn3m*. Double headed arrows indicate the full width at half-maximum of the peak (Δq).

Figure 5-2. Low-magnification SEM images of polymer cubosomes of (a) $PEG550_3$-PS_{150} and (b) $PEG550_3$-PS_{168}.

Figure 5-3. SEM images of polymer cubosomes of (a, c) $PEG550_3$-PS_{150} showing Schwarz P surface and (b, d) $PEG550_3$-PS_{168} showing Schwarz D surface.

Figure 5-4. (a) Reconstructed 3D image of the polymer cubosome of $PEG550_3$-PS_{150}. (b) Schematic illustration of Schwarz P surface (*Im3m*, [100] direction) and Schwarz D surface (*Pn3m*, [111] direction). The red- and green-colored regions indicate two non-interpenetrating networks of water channels. (c-f) SEM images of the surface layer and internal structure of polymer cubosomes of (c, d) $PEG550_3$-PS_{150} and (e, f) $PEG550_3$-PS_{168}. Squares and diamonds indicate the open channels (red color) and closed channels (green color) to the surrounding.

Figure 5-5. (a) Sequence of images extracted from the reconstructed 3D image of the polymer cubosome of $PEG550_3$-PS_{150} along the z direction. Red- and green-colored areas indicate the open and closed channel of the polymer cubosome. The inset shows merged image of two non-intersecting cubic channels. (b) Reconstructed 3D images of cutting plane of membranes (left), inverted image showing internal networks (middle), and merged image (right). The red arrows show the pore accessibility of the open channel.

Figure 5-6. SEM images of the silica replica of the polymer cubosomes of $PEG550_3$-PS_{150}. (a) Low-magnification SEM image showing spherical SiO_2 particles. (b, c) High-magnification SEM images showing silica framework on the surface of the replicated structures.

Figure 5-7. Normalized SAXS results of the polymer cubosomes (black line) and SiO_2 replicas (red line). (a) $PEG550_3$-PS_{150} (*Im3m*, a = 60.7 nm, *Pm3m*, a = 56.5 nm). (b) $PEG550_3$-PS_{168} (*Pn3m*, a = 45.2 nm, *Fd3m*, a = 90.7 nm). The colored lines correspond to the expected peak position for different space groups. The numbers above the graph are squares of the moduli of the Miller indices (*hkl*) for

each space groups.

Figure 5-8. Electron micrographs of internal single networks of SiO_2 replicated from polymer cubosomes of $PEG550_3$-PS_n; (a-c) $PEG550_3$-PS_{150}, (d-f) $PEG550_3$-PS_{168}. (a, b) SEM and (c) TEM images showing a single network of simple cubic lattice having six-fold nodes. (d, e) SEM and (f) TEM images showing a single network of single diamond lattice having four-fold nodes.

Figure 5-9. SEM images of TiO_2 frameworks replicated from the polymer cubosomes of $PEG550_3$-PS_{150}.

List of tables

List of schemes

Nomenclature

2D	Two-dimensional
3D	Three-dimensional
a	Lattice constant
ABTS	2,2′-Azinobis(3-ethylbenzothiazoline-6-sulfonic acid)
AFM	Atomic force microscopy
ATRP	Atom transfer radical polymerization
BCPs	Block copolymers
BET	Brunauer– Emmett–Teller
BJH	Barrett–Joyner Halenda
CET	Cryo-electron tomography
CLSM	Confocal Laser Scanning Microscopy
CTAB	Cetyltrimethylammonium bromide
$Đ$	Polydispersity index
DGMO	Diglycerol monooleate
DLS	Dynamic light scattering
DMF	Dimethylformamide
DP_n	Number of repeat units or degree of polymerization
EDS	Energy-dispersive X-ray spectroscopy
FFT	Fast Fourie transform
F-MI	Fluorescein-5-maleimide
f_{PEG}	The ratio of the molecular weight of the PEG domain to that of the PS block
GDO	Glycerol dioleate
GMO	Glyceryl monooleate
GPC	Gel permeation chromatography
HAADF-STEM	High-angle annular dark-field scanning transmission electron microscopy
HK	Horvath-Kawazoe
HR	High-resolution
HRP	Horseradish peroxidase
IBC	Inverse bicontinuous cubic
ICP-MS	Inductively coupled plasma mass spectrometry
K_M	Michaelis constant
l_c	Critical chain length of the hydrophobic domain
MALDI-TOF	Matrix-assisted laser desorption ionization time-of-flight
M_n	Number-average molecular weight
NHS	*N*-hydroxy succinimidyl ester

NMR	Nuclear magnetic resonance
P	Packing parameter
P4VP	Poly(4-vinyl pyridine)
PAA	Poly(acrylic acid)
PBOx	Poly(styreneboroxole)
PEG	Poly(ethylene glycol)
PEO	Poly(ethylene oxide)
PLA	Polylactide
PMDETA	*N*,*N*,*N'*,*N''*,*N''*-Pentamethyldiethylenetriamine
PODMA	Poly(octadecyl methacrylate)
PS	Polystyrene
Rho	Rhodamine
S-	Skeletal
SAXS	Small angle X-ray scattering
SDEMS	Solvent diffusion-evaporation-mediated self-assembly
SEM	Scanning electron microscophy
SIM^{2}PLE	Spinodal-decomposition-induced macro- and mesophase separation plus extraction by rinsing
SINPS	Non-solvent-induced phase separation
STP	Standard temperature and pressure
TEM	Transmission electron microscopy
TEOS	Tetraethyl orthosilicate
T_g	Glass-transition temperature
THF	Tetrahydrofuran
TPMSs	Triply periodic minimal surfaces
V_{max}	Maximum reaction rate
Δq	The full-width at half maximum of the first diffraction peak

Chapter 1. Introduction

1.1 Overview

Porous polymers with well-defined reticulated pores and large specific surface areas have attracted considerable attention owing to their ability to combine the desirable structural features of well-defined inorganic porous materials with the robust physical properties of polymers. The well-defined internal porosity of these materials can be applied to guest encapsulation and templating. In addition, further functionality can be introduced by incorporation of functional group onto the surface of the porous structures. Such materials can be utilized in applications involving drug delivery, water purification, catalysis, and separation.[1–6] Depending on the method of synthesis, the internal space within porous polymers can adopt a two-dimensional (2D) or a three-dimensional (3D) network structure.

Block copolymers are versatile building blocks that can be used to generate well-defined 3D structures. However, the direct self-assembly of block copolymers into porous structures remains an on-going challenge. Currently, most porous polymer materials are prepared through the removal of one block type after the microphase separation of block copolymers in bulk.[7] This method is limited by the fact that the size of the pores depends on the length of the polymer chain removed after the phase-separation.

In the past, the self-assembly of simple lipids such as glyceryl monooleate (GMO) into interesting inverse bicontinuous crystalline phases in an aqueous solution has been reported from a binary mixture of GMO and water.[8] These mesophases and their colloidal forms, referred to as cubosomes, have an infinite network of water channels, which can be used as nanospace for the encapsulation of guest molecules. Unlike the bulk assembly, the pores are relatively large despite the small molecular weight of lipids. Nevertheless, the small molecular weight of lipids limits the stability and pore size (~20 nm) of the assembled structures.[9]

From this perspective, the formation of inverse bicontinuous phases through the self-assembly of block copolymers represents an attractive goal. Block copolymers have higher molecular weights than lipids, and the self-assembled structures produced from block copolymers are, therefore, expected to possess improved stability, with morphologies that are larger in size than those afforded by lipids.[10] Thus, block polymers can permit the construction of larger water channel networks, which are more applicable than lipid cubosomes. In aqueous solutions, amphiphilic block copolymers self-assemble into many forms that exhibit tendencies similar to those of structures assembled from lipids. Amphiphilic block copolymers can be synthesized by covalently connecting the hydrophilic block and the hydrophobic block. In addition, amphiphilic block copolymers that incorporate monomers with

different chemical properties can be used to control the self-assembly process and to give structures with desired functionalities.

Recently, a structure similar to that of lipid cubosome has been reported through the self-assembly of a macromolecule with structural specificities.[11] However, a practical framework for understanding and predicting the conditions required for the creation of inverse structures such as cubosomes has not been developed to date. Therefore, finding the self-assembly conditions that would permit direct formation of polymer cubosomes, which could be employed as porous polymer materials in various fields of applications, remains a fundamental challenge.

Through the careful design of the self-assembly process, it is possible to synthesize not only spherical colloids but also thin films or monoliths that possess internal mesoporous structures. The main objectives of this thesis are to develop a synthetic method for the fabrication of mesoporous polymer materials and to evaluate their potential applications.

1.2 Synthesis of amphiphilic block copolymers

Amphiphiles such as phospholipids, which form bilayers in living cells, are chemical compounds that possess both hydrophilic and hydrophobic properties. Many lipids are capable of self-assembling into structures with different morphologies in aqueous solutions. One of the driving forces for this self-assembly is the hydrophobic effect, which acts to minimize the interface between the hydrophobic portion of the amphiphile and polar water molecules. Therefore, amphiphilic block copolymers that incorporate covalently linked hydrophobic and hydrophilic blocks can exhibit self-assembly behavior that is similar to that of lipids in aqueous solutions.

Atom transfer radical polymerization (ATRP) is a widely used synthetic method for the preparation of block copolymers with relatively uniform and low molecular weight distribution.[12] In this method, the total molecular weight and the ratio of the two sub-units used to construct the block copolymer can be controlled by varying the amounts of the monomer and the initiator used in the polymerization reaction. Depending on the synthesis method, this control over reaction conditions can facilitate the synthesis of block copolymers that adopt various shapes, ranging from dendrimers, stars, and grafts, to linear shapes.[13–15] For example, Kim and coworkers reported the synthesis of dendritic-linear block copolymers and their subsequent self-assembly in aqueous solution.[16] In this work, peripheral poly(ethylene glycol) (PEG) chains were introduced into benzyl ether dendrons to make macroinitiator. Next, the block copolymers were synthesized polymerization of hydrophobic polystyrene in the presence of these macroinitiators under ATRP conditions (Figure 1-1).

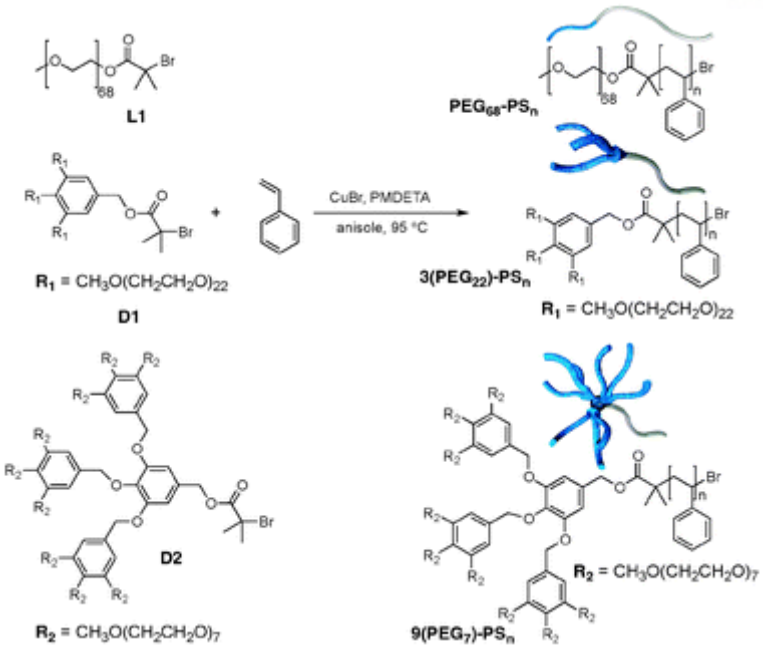

Figure 1-1. ATRP of block copolymers containing a linear or dendritic PEG hydrophilic block. The molecular weight of the PEG segment is fixed at *ca*. 3000 g mol^{-1} (Ref. 16).

1.3 Self-assembly of block copolymers in solution

In the bulk state, block copolymers with immiscible blocks self-assemble into nanostructures through microphase separation. In aqueous media, unlike in the bulk state, more complicated assembly behavior that depends on the nature of the solvent is often exhibited. Perhaps the most typical method used to drive the self-assembly of block copolymers in solution is known as the co-solvent method.[17] In this method, a block copolymer is first dissolved in an organic solvent that is suitable (i.e., common) for both the hydrophilic and the hydrophobic block. Subsequently, an equal amount of water, which is a non-solvent for the hydrophobic block, is slowly added. During the process, aggregation occurs to minimize the contact area that consists of the atoms of the hydrophobic block in contact with the molecules of water. Therefore, the hydrophobic blocks aggregate with each other, while the hydrophilic blocks remain exposed to water. After a few hours, the organic solvent is removed by dialysis against water to afford the final self-assembled structure.

When amphiphiles self-assemble in solution, the morphology of the resulting self-assembled structures is determined by the geometric shape of the amphiphile. The critical packing parameter P ($P = v/a_0 l$, where v is the volume of the hydrophobic domain, a_0 is the effective area of the hydrophilic head, and l is the effective length of the hydrophobic chain) is a numerical representation of the geometric shape of a molecule.[17] If P is lower than 1/3, a cone-like geometry of the amphiphile will guide the formation of micelles in aqueous solution. As the P value increases, the morphology transforms gradually to a cylindrical shape, lamella, and vesicles (Figure 1-2).

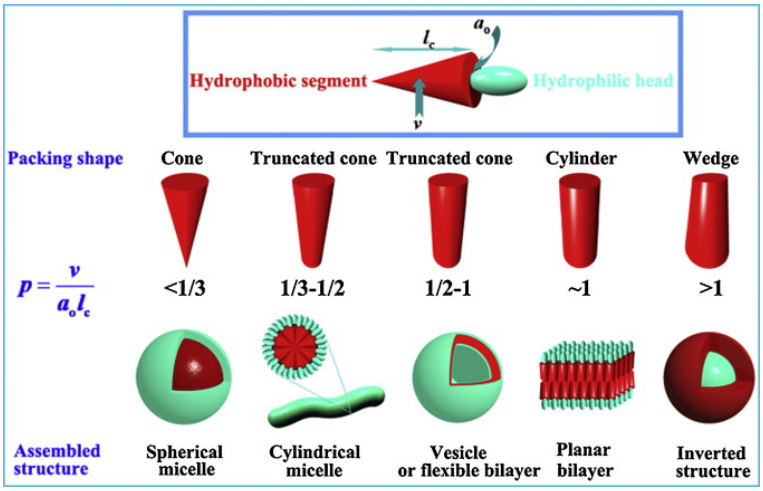

Figure 1-2. The effect of the packing parameter on the structures of assemblies formed (Ref. 17).

The packing parameter theory applies not only to low-molecular-weight surfactants such as lipids but also to amphiphilic block polymers. Kim and coworkers reported the synthesis of sugar-responsive block copolymers that self-assembled into a variety of nanostructures.[18] The self-assembled structures were prepared using tetrahydrofuran (THF) solution as the common solvent. As the degree of polymerization of the hydrophobic poly(styreneboroxole) (PBOx) block increased, i.e., when the *P* value increased, the morphology of the self-assembled structures changed from that of spherical micelles to cylindrical micelles, and finally to polymersomes (Figure 1-3). By adjusting the block ratio, the authors demonstrated that the polymersomes can be used as sugar-responsive delivery vehicles for insulin.

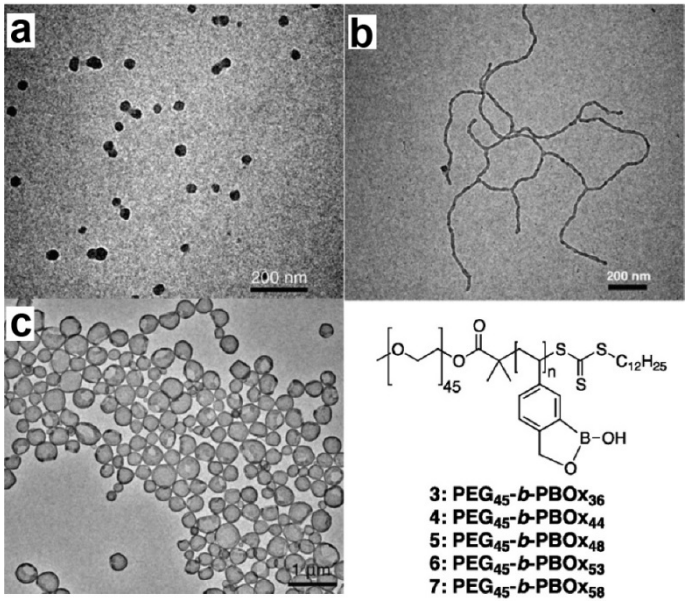

Figure 1-3. TEM images of micelles and polymersomes formed by self-assembly of PEG-*b*-PBOx in water. (a) Spherical micelles of **3**. (b) Cylindrical micelles of **4**. (c) Polymersomes of **7** (Ref. 18).

Eisenberg and coworkers prepared various morphologies such as spherical micelles, vesicles, and bicontinuous structures through the self-assembly of 'crew cut' block copolymers with an asymmetrically large hydrophobic block.[19,20] The polymer used in this study was polystyrene-*b*-poly(acrylic acid) (PS-*b*-PAA). The authors achieved different self-assembled structures by changing the block ratio and the molecular weight of the block copolymer. For example, the authors prepared a series of PS-*b*-PAA with the same polystyrene block length but with different PAA lengths using anionic polymerization. As the ratio of the hydrophilic block to the hydrophobic block decreased, the morphologies of the crew-cut aggregates displayed a morphological change that is illustrated in Figure 1-4. These results indicate that a morphological transition in linear block copolymers can be induced by changing the lipid packing parameter.

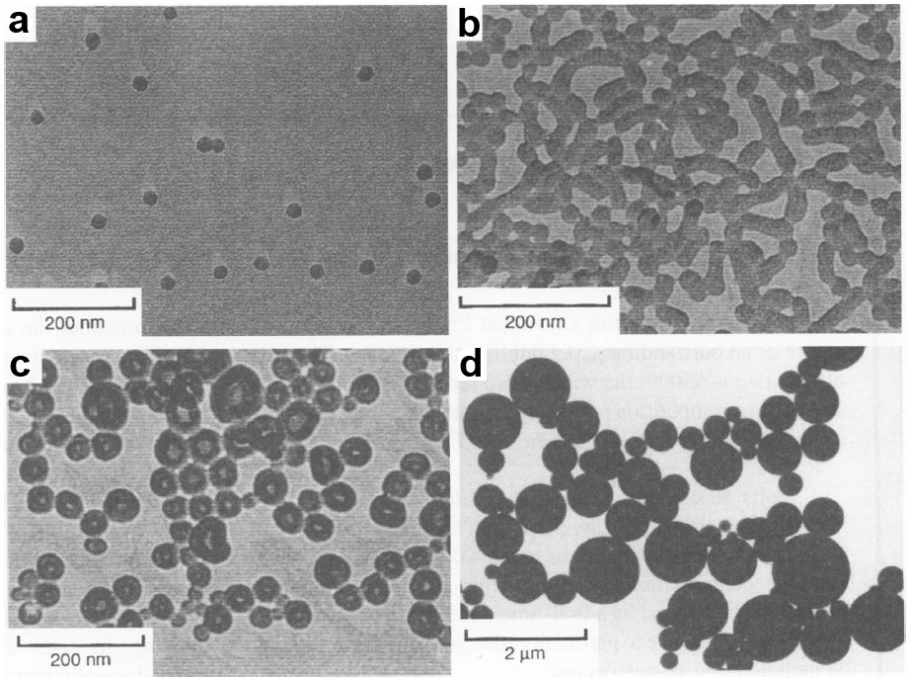

Figure 1-4. Multiple morphologies of the crew-cut aggregates from PS-*b*-PAA block copolymers of (a) 200-*b*-21, (b) 200-*b*-15, (c) 200-*b*-8, and (d) 200-*b*-4 (Ref. 19).

Self-assembly of complex non-linear amphiphiles was reported to produce intriguing nanostructures in solution. Percec and coworkers synthesized amphiphilic Janus dendrimers by coupling tailored hydrophilic and hydrophobic branches, demonstrating that the self-assembly can generate a variety of new morphologies.[21] Among these morphologies, two new structures, namely the polygonal dendrimersome and bicontinuous cubic, were observed that have not been detected in self-assembled structures of linear block copolymers (Figure 1-5).

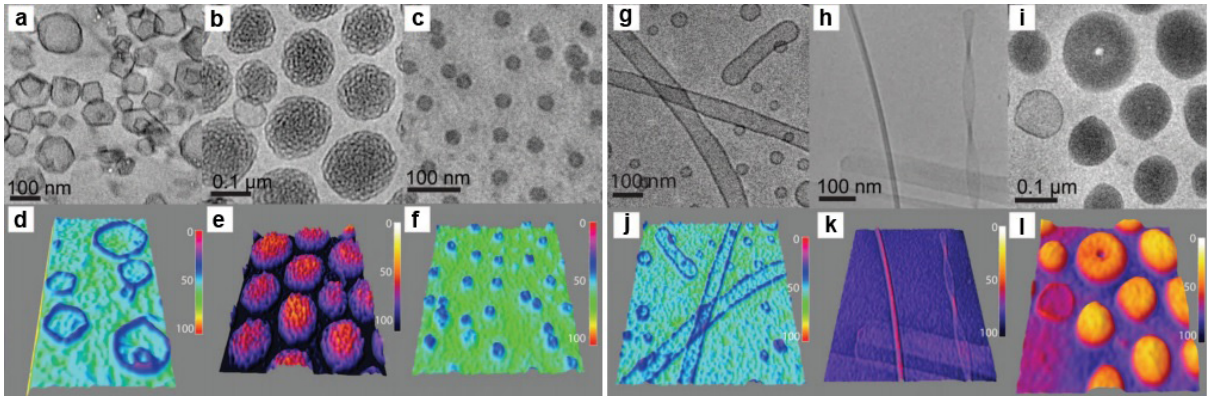

Figure 1-5. Cryo-TEM and 3D intensity profile of assembled structures from various dendrimers. (a and d) Polygonal dendrimersomes. (b and e) Bicontinuous cubic particles. (c and f) Micelles. (g and j) Tubular dendrimersomes. (h and k) Rodlike, ribbon and helical micelles. (i and l) Disklike micelles and toroids (Ref. 21).

Since the critical packing parameter is determined not only by the block ratio but also by the architectures of the employed block copolymers, the self-assembled structures are known to be affected by the design of the block copolymers. Nowadays, various self-assembled morphologies and their applications are being studied by tailoring the structure and assembly conditions of block copolymers.[22–25]

1.4 Inverse bicontinuous structures

For several decades, the self-assembly of block copolymers has been extensively studied for the formation of nanostructures such as micelles, cylindrical micelles, and polymer vesicles, in the range of P values <1.[26–29] When the P value exceeds 1, the packing geometry of the amphiphile adopts a wedge-like form that induces a negative curvature in the bilayer. As a result, the self-assembly process results in the formation of inverse structures (Figure 1-6).

Amphiphile–water systems are known to form inverse crystalline cubic structures that are bicontinuous in terms of the aqueous and the lipid regions.[8] These phases possess an infinite network of water channels. Typically, glyceryl monooleate–water systems exhibit a variety of inverse structures (Figure 1-6). The phase diagram of monoolein was determined for the first time by Lutton in 1965. Recently, Qui and Caffre reported an advanced phase diagram of this system.[30]

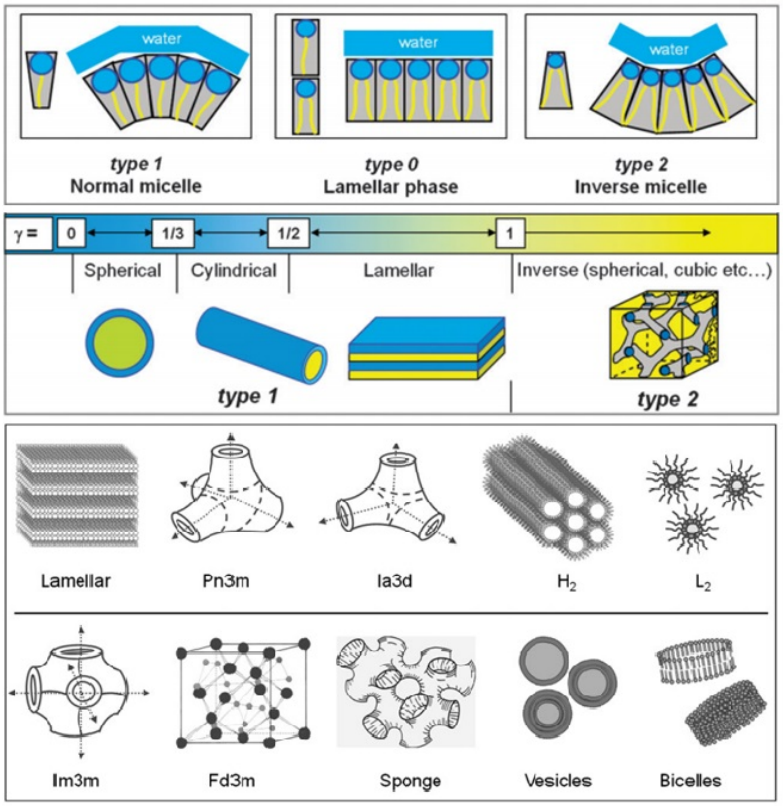

Figure 1-6. Molecular shape and type of amphiphilic self-assemblies. (In figure, γ is same expression of *P*, packing parameter) Double headed arrows indicate the range of most preferred geometries. Monoolein (type 2) shows lamellar, bicontinuous cubic-Pn3m and Ia3d phases, hexagonal (H_2) and fluid isotropic (L_2) phases in the presence of water. Additional structures are also shown by monoolein but in presence of additives (Ref. 8).

Unlike the inverse hexagonal phases, which have a negative mean curvature toward the aqueous interior, inverse cubic phases have zero mean curvature at any point on the surface. As a result of these structural features, the inverse cubic phases are called triply periodic minimal surfaces (TPMSs).[31–33] The basic unit cells of the minimal surfaces have cubic symmetry, and these surfaces divide the space into two equal areas, hence the term bicontinuous. The three types of inverse bicontinuous cubic phases are the primitive (P, *Im3m*), double-diamond (D, *Pn3m*), and gyroid (G, *Ia3d*) (Figure 1-7).[34] The representations of the two internal regions for all three types reveal considerable similarities in the network structures (Figure 1-8). In other words, these structures possess two distinct water channels in aqueous solution. In each structure, the internal network has six-fold, four-fold, and three-fold junctions, respectively.

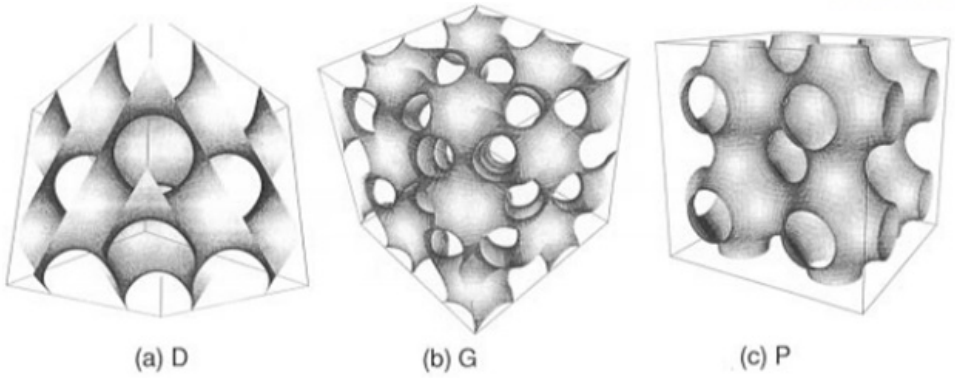

Figure 1-7. The three minimal surfaces, D, G, and P, that represent the three inverse bicontinuous cubic morphologies found in block copolymers and amphiphilies/water systems (Ref. 34).

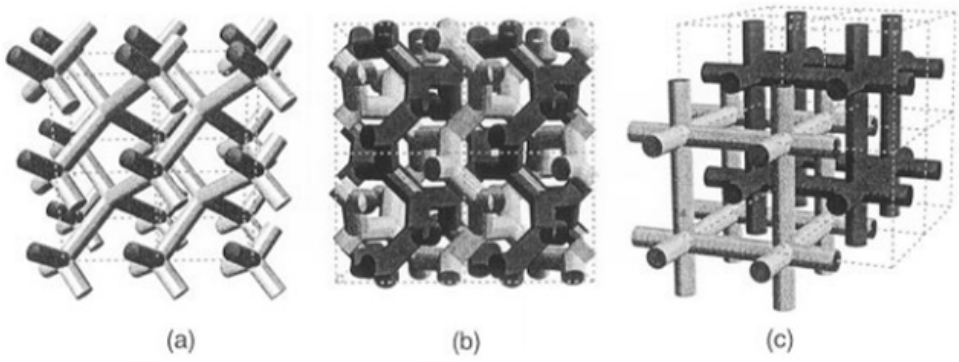

Figure 1-8. Representation of the internal two uniform networks in three bicontinuous cubic morphologies, D, G, and P (Ref. 34).

Although the minimal surfaces have interesting and useful structural features, achieving good dispersion of inverse bicontinuous cubic phases assembled from lipids is challenging as a result of their limited stabilities in aqueous environments.[35] Since the exposure of the hydrophobic domains to the aqueous medium must be avoided, the resulting nanoparticles must be stabilized by the addition of a dispersing agent.

Gustafsson and coworkers reported aqueous dispersions of inverse hexagonal and bicontinuous cubic phases.[36] The authors used a nonionic triblock polymer, $PEO_{98}PPO_{67}PEO_{98}$ (Poloxamer 407), as a dispersing agent. The less water-soluble PPO block is adsorbed on the surface of the particle, while the hydrophilic PEO blocks extend into the solution-contacting area. In this paper, a homogeneous melt of lipids and the dispersing agent was added dropwise into water while stirring. The inverse phases of the particles were studied by small-angle X-ray scattering (SAXS) and cryo-transmission electron microscopy (cryo-TEM). The analysis revealed that particles with 7.4 wt% and 4 wt% of polymer exhibited *Im3m* and *Pn3m* symmetry, respectively. TEM imaging indicated that the particles have a faceted shape with a crystalline internal order (Figure 1-9).

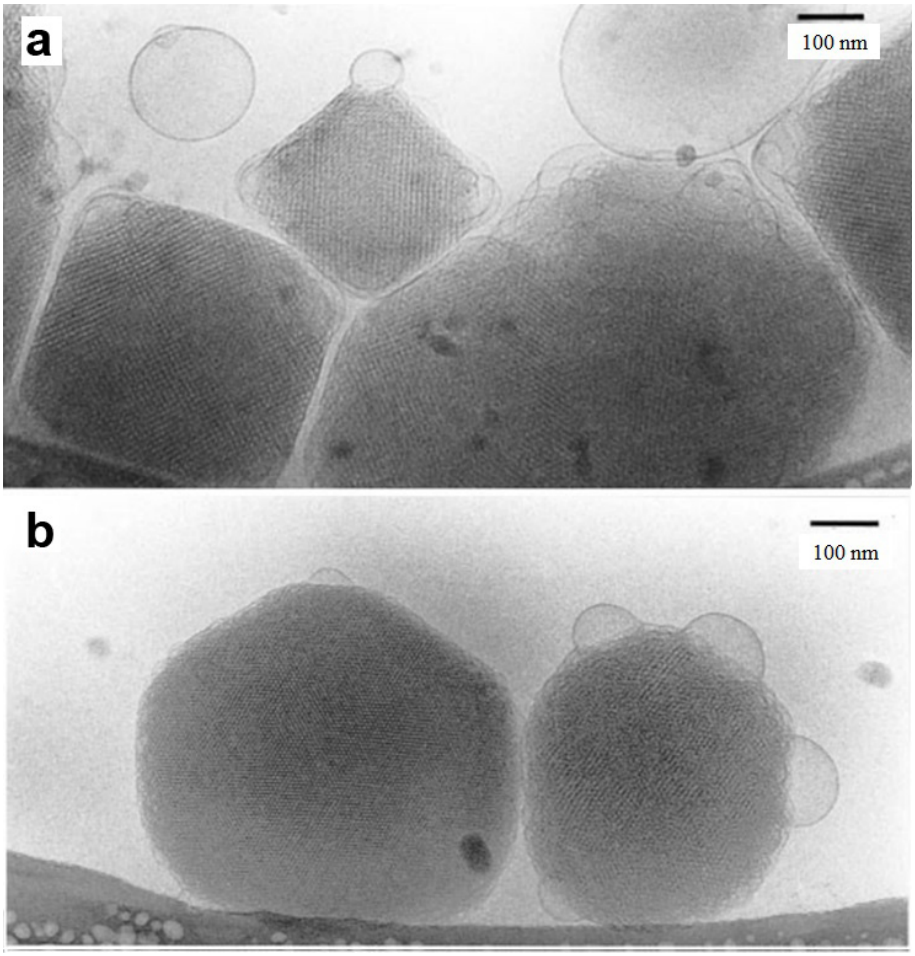

Figure 1-9. Cryo-TEM micrographs of dispersed particles from the cubic phase of monoolein and Poloxamer 407 in water. (a) 7.4 wt% polymer to lipid. Faceted cubic particles showing a clear crystalline structures of *Im3m* (lattice constant, a = 13 nm). (b) 4 wt%. Particles showing hexagonal symmetry which is same projection of the (111) planes of the *Pn3m* (a = 9.6 nm) (Ref. 36).

Although cubic phases formed in the GMO–water have been widely studied, other lipids and monoglycerides have also been reported to form inverse bicontinuous phases. Barauskas and coworkers reported the formation of colloidal inverse bicontinuous phases with other lipids.[37] The authors observed sponge mesophases and inverse hexagonal structures using a mixture of glycerol dioleate (GDO) and diglycerol monooleate (DGMO) (Figure 1-10). They also found phytantriol-based *Im3m* cubic phases upon introduction of small amounts of D-alpha-tocopheryl poly(ethylene glycol) 1000 succinate (Vitamin E TPGS).

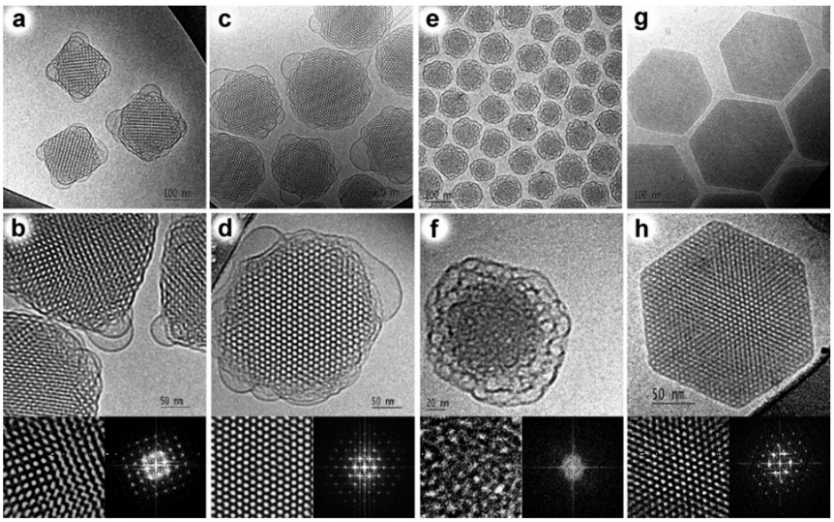

Figure 1-10. Representative cryo-TEM micrographs and Fourier transforms of lipid nanoparticles. (a-d) GMO/Poloxamer 407/water system. *Im3m* phases viewed along [001] and [111] directions (lattice constant, a = 12.9 nm). (e, f) DGMO/GDO/P80/water system. Sponge phase. (g, h) DGMO/GDO/Poloxamer 407/water system. Inverse hexagonal phase (lattice constant, a = 5.5 nm) (Ref. 37).

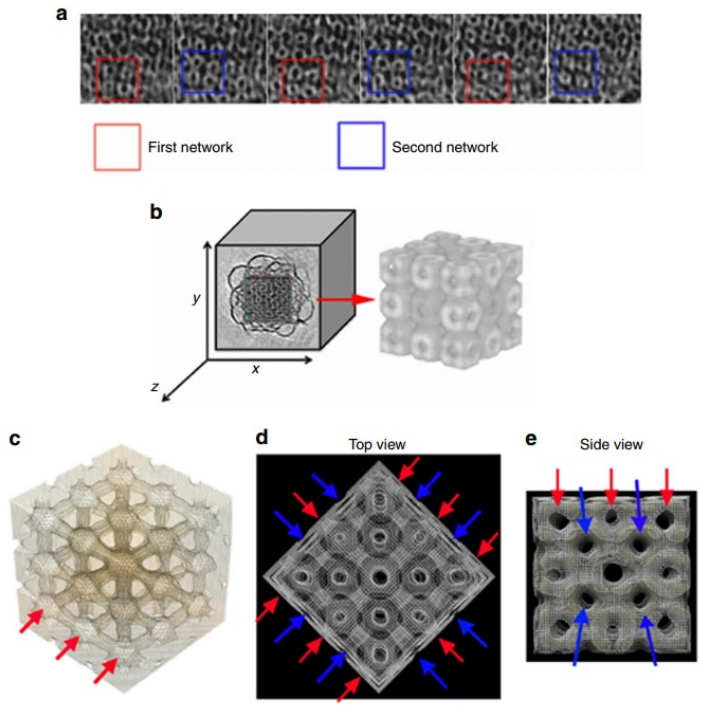

Figure 1-11. 3D organization of the liquid crystal region inside cubosomes. (a) Sequence of images extracted from the tomogram along the z direction. The alternate position of network indicating the sequence of the channels. (b) Original tomogram and its 3D reconstruction showing the unit cells. (c) Extract of the tomogram showing one of the two water channel network. (d, e) Top and side view of the filtered 3D reconstruction where the pores belonging to the two networks are indicated (Ref. 38).

The mathematical model of the triply periodic minimal surfaces is known in which the membrane divides the space into two channels. However, direct observation of the water and lipid networks in the bicontinuous phases has not been reported to date. Recently, Martiel and coworkers performed cryo-electron tomography (CET) on *Im3m* space-group nanoparticles to demonstrate the presence of internal networks.[38] The authors confirmed that the particle interior is constituted by two continuous water channels that are separated by lipid bilayers. The sequence of images extracted from the tomogram along the z-direction shows pores that belong to the water channels. The images allow visualization of two independent networks that are marked in red and blue (Figure 1-11).

The porous features of inverse cubic structures make these porous materials ideal platforms for a large number of applications. However, their low stability and the pore size limit caused by the low molecular weight of the lipids are drawbacks that needs to be addressed.

1.5 Block copolymer-derived inverse structures

To date, analogues of cubosomes have also been observed in the self-assembly of synthetic macromolecules. Holder, Sommerdijk, and Biagini observed spherical aggregates that exhibit internal microphase separation.[39] The formation of these complex morphologies was caused by the aggregation of amphiphilic double-comb diblock copolymers. Analysis of the reconstructed 3D volume confirmed the presence of a bicontinuous network within the aggregates (Figure 1-12).

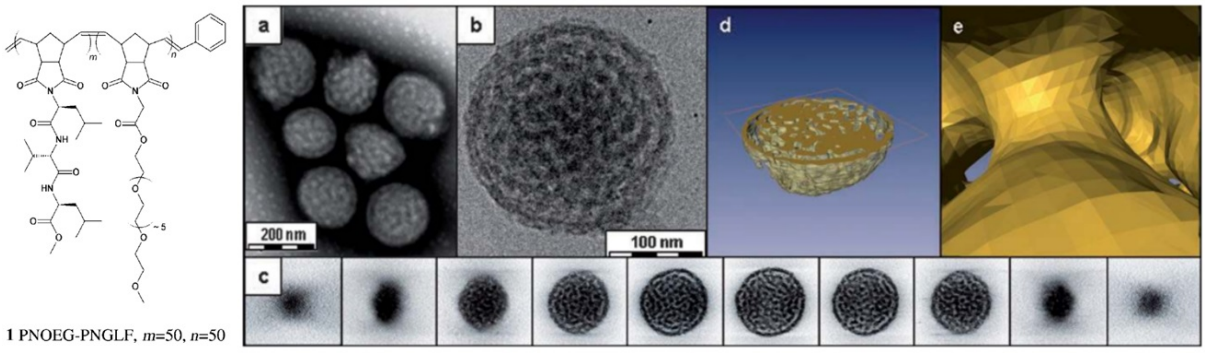

Figure 1-12. TEM analysis of aggregates of double-comb block copolymers. (a) A TEM image using negative staining. (b) Cryo-TEM image. (c) Sequence of z slices showing different cross sections. (d, e) Visualization of the segmented volume showing (d) a cross section of aggregate and (e) a view from within the hydrated channels (Ref. 39).

Following the observation of bicontinuous phase separation of nanoparticles, Sommerdijk and coworkers also reported nanospheres with bicontinuous internal structures formed from a semi-crystalline block copolymer, poly(ethylene oxide)-*block*-poly(octadecyl methacrylate) (PEO_{39}-*b*-$PODMA_{17}$), in aqueous dispersion.[11] The PEO_{39}-*b*-$PODMA_{17}$ was synthesized by ATRP of ODMA,

with PEO as the macroinitiator. Aggregate dispersions of this copolymer were formed using the co-solvent method at 35 °C and the structure of the aggregates was investigated with cryo-TEM and CET. The projection images recorded at 4 °C confirmed the presence of inverse bicontinuous structures. The reconstructed 3D images showed that the internal channels are interconnected (Figure 1-13). Since PDOMA is a temperature-responsive block, the ordered internal structure could not be observed at a temperature of 45 °C, i.e., a temperature that is higher than the transition temperature.

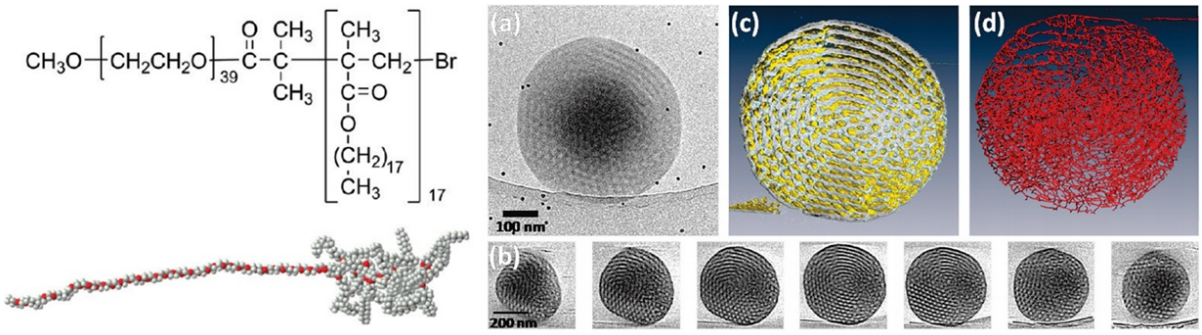

Figure 1-13. Chemical structure and TEM analysis of PEG_{39}-*b*-$PODMA_{17}$ aggregates. (a) Cryo-TEM image at 4 ˚C. (b) Gallery of z slices showing different cross sections. (c) Regenerated 3D visualization showing only an inner section of the whole structure. (d) Skeletonization of c, showing interconnected structures (Ref. 11).

Nevertheless, inverse structures with high crystallinity such as lipid cubosomes were not observed in the self-assembly of block copolymers. While the self-assembly of block copolymers resulted in some inverse structures, a clear set of rules that would ensure that the self-assembly of block copolymers would afford crystalline inverse bicontinuous cubic structures in solution has not been formulated to date.

1.6 Formation of mesoporous film

Porous films are used in applications such as filtration, drug delivery, catalysis, and separation. Thin films with the above-described inverse structure can find application in many fields because these inverse cubic phases have a high crystalline order of internal networks.

Porous polymers, including inverse structures, are typically produced by removing one polymer domain from a self-assembled film through micro-separation of block copolymers in the bulk state. For example, Cussler and coworkers reported ultrafiltration membranes based on cylinder-forming block copolymers.[40] In a polystyrene-*b*-polylactide (PS-PLA) system, PS serves as the continuous matrix and PLA is the etchable block. Once the polymer solution is cast, the concentration at the surface rapidly decreases and microphase separation occurs as a result of rapid evaporation. When the nucleation of the ordered structure is complete, the thickness of the ordered phase increases.

Following the selective etching of perpendicularly oriented cylinders of PLA, the membranes exhibited nanoporous character (Figure 1-14).

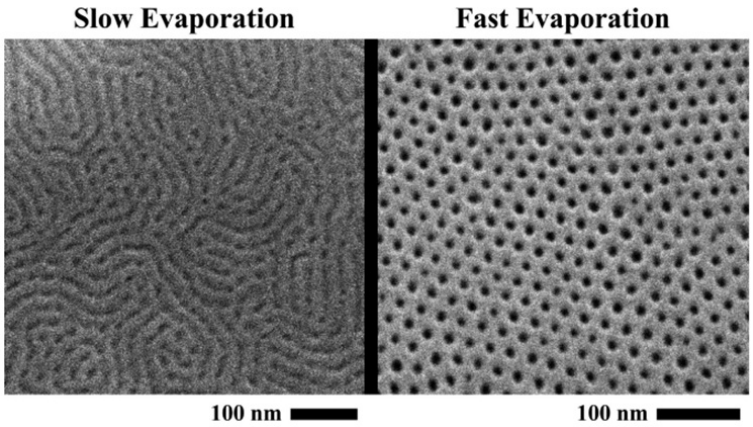

Figure 1-14. SEM micrographs of the top surface of PS-PLA thin films show that evaporating toluene slowly produces a parallel orientation, while rapid evaporation aligns the cylinders in a perpendicular orientation (Ref. 40).

A method for the formation of an asymmetric internal membrane through phase separation has also been reported. Peinemann and coworkers reported the creation of an asymmetric superstructure using non-solvent-induced phase separation (SINPS).[41] In this simple process, a polymer solution is immersed in water to induce phase separation. The authors used polystyrene-*b*-poly(4-vinyl pyridine) (PS-*b*-P4VP), which belongs to the class of non-ionic amphiphilic systems. After casting the film on a glass substrate, solvent evaporation was activated for 10 s, and, subsequently, the film was immersed in a water bath for 12 h, followed by drying at ambient conditions. The resulting membrane was covered by well-ordered cylindrical pores, oriented perpendicular to the film surface, while the interior was composed of a non-ordered sponge-like layer (Figure 1-15).

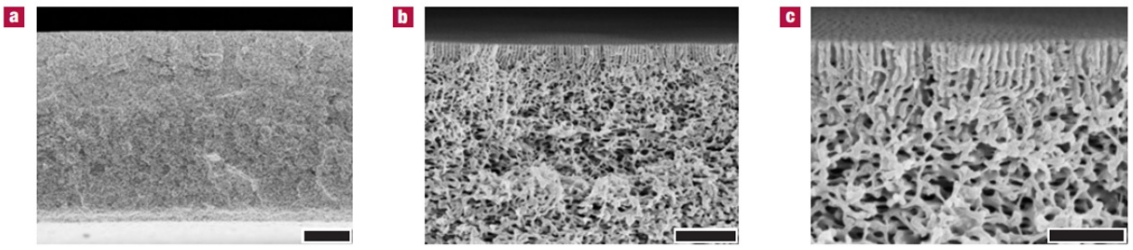

Figure 1-15. SEM images of the cross-sectional morphology of the asymmetric PS-*b*-P4VP diblock copolymer film at different magnifications. The scale bars correspond to (a) 20 μm, (b) 1 μm, and (c) 0.5 μm (Ref. 41).

Recently, Wiesner and coworkers discussed two methods for the formation of porous polymer structures.[42] Unlike SINPS, the second method referred to as SIM^{2}PLE (spinodal-decomposition-induced macro- and mesophase separation plus extraction by rinsing) allows the formation of hierarchically porous polymer monoliths that possess both macropores and ordered mesopores. The authors prepared a xylene solution with poly(styrene)-*block*-poly(ethylene oxide) (PS-*b*-PEO) diblock copolymer and oligomeric PEO (o-PEG) as an additive. After thermal annealing of the film, the product was immersed in a protic solvent to remove the additive (Figure 1-16). The authors found that the films cast at 100 °C have cubic morphology with randomly distributed macropores. SAXS results showed that the film had a cubic lattice with *Pn3m* symmetry.

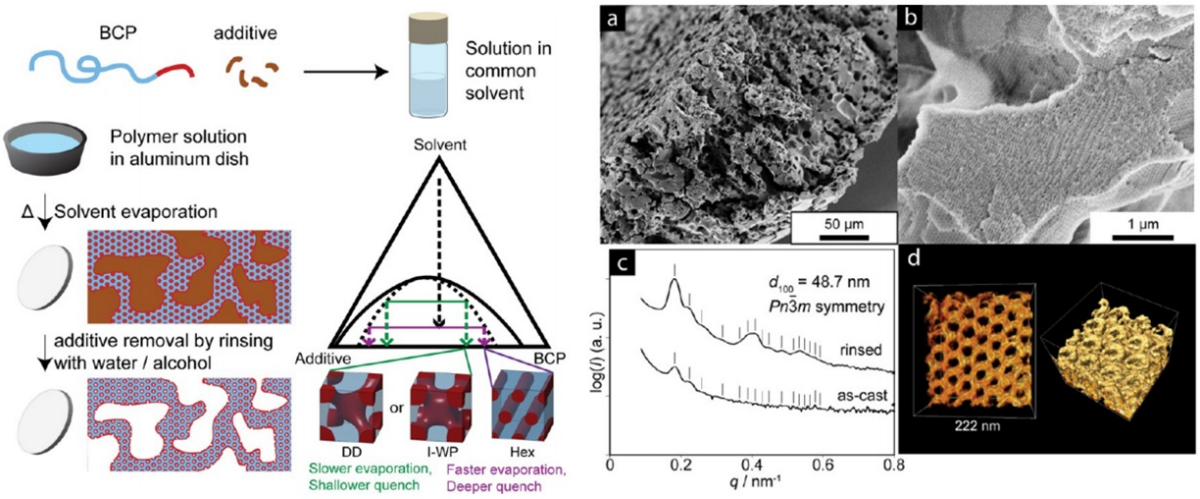

Figure 1-16. Schematic of SIM^{2}PLE procedure and characterization of PS-*b*-PEO + o-PEO hierarchically porous material cast at 100 °C. (a) Low magnification and (b) high magnification SEM images of a fractured cross-section. Tick marks indicate expected peak position for *Pn3m* symmetry. (c) SAXS traces of the as-cast film and films after o-PEO removal. (d) TEM tomographic reconstruction of cubic mesostructures (Ref. 42).

Although many methods have been proposed thus far for the formation of mesoporous films, almost all of them require post-processing treatment such as etching and the resulting materials display no long-range crystallinity. The direct self-assembly of block copolymer into inverse cubic structures may facilitate the development of a new strategy for the generation of porous films. This method has the advantage of producing mesoporous films without the need for post-processing since the volume of water in the self-assembled structure is implemented directly in the form of a porous network.

1.7 Templated synthesis of skeletal inorganic structures

Three-dimensional porous materials can be used in applications such as sensing, photonics, filtration, and catalysis. However, for a specific application, it is often necessary to convert desired porous structures into technically more suitable materials.[43] The field of application of a mesoporous polymer structure is limited by its requirement for an organic solvent. The number of applications can be increased further if the mesoporous structures are replaced with various target materials such as inorganics, metals, and polymers. In this regard, the use of ordered porous materials as sacrificial templates could provide a simple pathway to the production of crystalline network structures of desired lattice and periodicity.

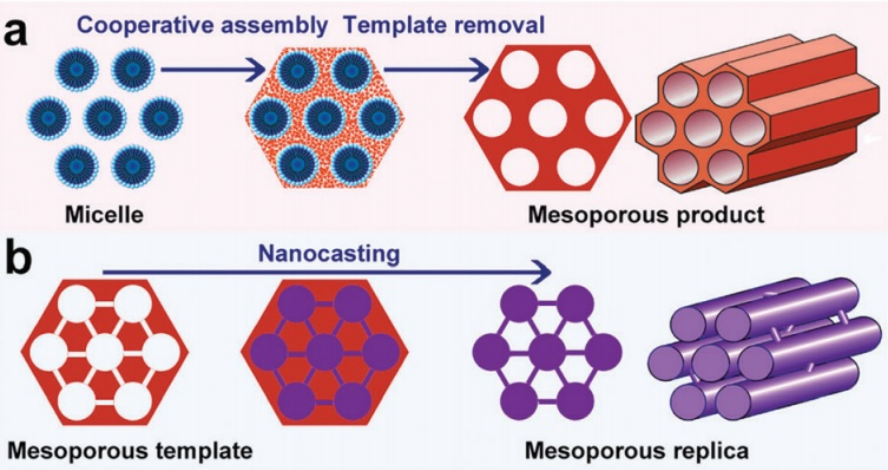

Figure 1-17. Scheme of two representative synthesis routes for ordered mesoporous materials. (a) Soft-templating method. (b) Hard-templating (nanocasting) method (Ref. 44).

A typical templating method for generating mesoporous materials is a sol-gel reaction that employs an inorganic precursor (Figure 1-17).[44] Rational control of the hydrolysis and condensation of inorganic precursors ensures successful infiltration and replication of 3D nanostructures of templates.[45] Over the past decades, the sol-gel process of SiO_2 has attracted significant attention owing to the discovery of novel mesoporous silicas such as MCM-41 and SBA-15.[46,47] The majority of syntheses of mesoporous silica utilize the so-called soft-templating approach, in which a surfactant is used as the pore-generating agent. The soft-templating method can also be used to create hierarchical structures within 3D porous sacrificial templates. To date, mesoporous TiO_2 has been widely studied as a result of its good chemical and thermal stability and desirable optical properties.[48] For example, mesoporous TiO_2 exhibits high photocatalytic activity because of its higher accessibility of active sites and faster diffusion rate compared to bulk TiO_2.[49]

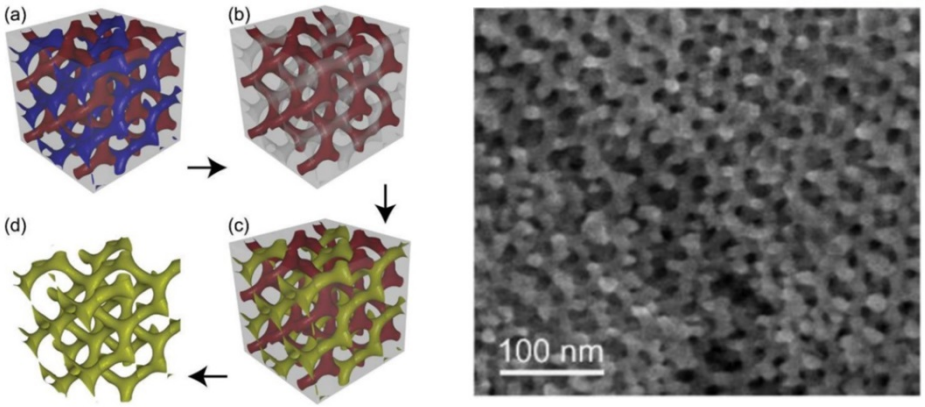

Figure 1-18. Schematic representation of sample fabrication and SEM image of a metal gyroid. The isoprene block (blue) is removed and is then back-filled with gold (yellow). The final structure is obtained by plasma etching (Ref. 50).

In some cases, inverse bicontinuous cubic structures have been replicated with polymeric templates. Steiner and coworkers created 3D gold metamaterial by replacing one of the continuous polymer networks in double gyroid structures.[50] The authors used an isoprene-*b*-styrene-*b*-ethylene oxide (ISO) block copolymers to form polymer film scaffolds. Following the removal of one network consisting of isoprene through UV exposure, the resulting films were back-filled with gold by electrodeposition. The residual polymer was removed by plasma etching (Figure 1-18).

In nature, single network structures can be found in the biophotonic structures of butterfly wing scales and the exoskeletons of beetles.[51,52] Butterfly wings produce vivid structural color that arises as a result of specific nanostructure, with a periodicity of 200 nm or more (Figure 1-19). The wing of the butterfly is formed by the polymerization of chitin that is present on the endoplasmic reticulum of the scale cell, which has a double network structure. Since only one channel is filled with chitin, however, the wings of the butterfly form a single-network skeletal structure.[52]

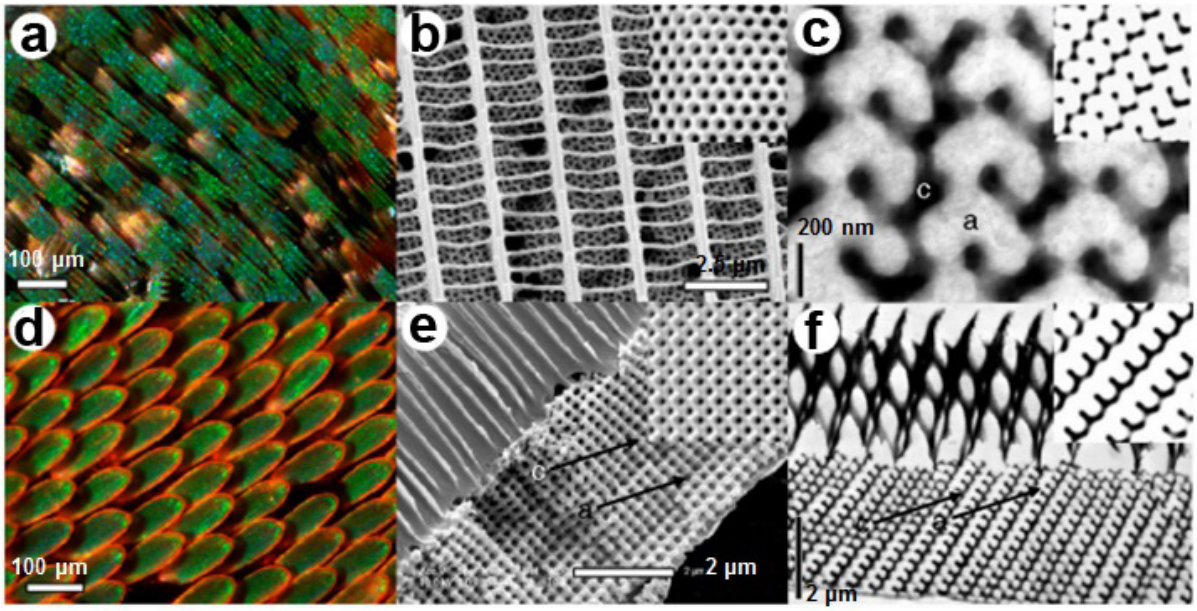

Figure 1-19. Anatomy of the structural color-producing nanostructures in (a-c) lycaenid and (d-f) papilionid butterflies. (a, d) Light micrograph of wing cover scales. (b, e) SEM and (c, f) TEM images of surfaces and nanostructures of scales. Insets show simulated (b) (111), (c) (310), (e) (110), and (f) (211) projection of single gyroid structures.

In the case of inverse structures assembled from polymers, there are two channels in the cubosomes, although only one channel is exposed on the surface. Theoretically, when a precursor is introduced and replicated on only one channel, a single network similar to that observed in the butterfly wing can be synthesized. This approach may offer a convenient method for synthesizing photonic crystals.

1.8 Thesis summary

The inverse bicontinuous cubic phases of lipids possess internal crystalline networks of water channels. These structural features allow these phases to be used in many applications as porous materials. Since the self-assembly behavior of amphiphilic block copolymers is similar to that of lipids, the macromolecules employed can likewise give rise to inverse structures. However, a unified strategy for the generation of polymeric inverse structures with high crystallinity has not been reported to date.

Following the Introduction in Chapter 1, Chapter 2 describes the direct self-assembly of dendritic-linear block copolymer into colloidal inverse bicontinuous cubic structures. These polymer cubosomes exhibit three inverse cubic phases (*Im3m, Pn3m, Ia3d*) that depend on the architecture of the dendritic hydrophilic block. The highly crystalline cubic structures are confirmed by electromagnetic microscopy and X-ray scattering experiments. Finally, functional groups are incorporated onto the surface of the polymer cubosomes in order to permit the utilization of the

internal networks for encapsulation of large molecules such as enzymes.

Chapter 3 reports a simple method for the preparation of mesoporous monoliths composed of inverse bicontinuous cubic structures. This method, named as the 'solvent diffusion-evaporation-mediated self-assembly' (SDEMS), allows direct formation of internal water channels without the requirement for any post-processing for pore generation. The results confirm that the internal large-pore networks can not only accommodates large molecules, but also serve as templates for the synthesis of inorganic networks.

In Chapter 4, the morphological transition of self-assembled structures of branched-linear block copolymers is observed. By utilizing solvent mixtures to dissolve the block copolymer, the affinity of the solvent toward the hydrophobic block is altered, thus affecting the self-assembly process of the block copolymer. A branched-linear block copolymer that self-assemble only into polymer vesicles displays a morphological transition from vesicles to inverse cubic and inverse hexagonal phases as a result of an increase in the proportion of DMF in the solvent mixture. Similar transition is also observed using the SDEMS method. The internal structure of the film is found to change from stacked lamellae to inverse cubic phase and inverse hexagonal phase.

Finally, Chapter 5 describes the synthesis of inorganic single networks using polymer cubosomes as templates. Since the interfacial topology of the polymer cubosome has only one channel exposed to the outside, the guest molecules can only diffuse into one channel of the cubosomes. The results confirm the replication of the single network of polymer cubosomes through a sol-gel reaction with inorganic precursors.

Portions of this thesis have been published.

Chapter 2: La, Y.; Park, C.; Shin, T. J.; Joo, S. H.; Kang, S.; Kim, K. T. "Colloidal inverse bicontinuous cubic membranes of block copolymers with tunable surface functional groups" *Nat. Chem.* **2014**, *6*, 534–541.

Chapter 3: Park, C.; La, Y.; An, T. H.; Jeong, H. Y.; Kang, S.; Joo, S. H.; Ahn, H.; Shin, T. J.; Kim, K. T. "Mesoporous monoliths of inverse bicontinuous cubic phase of block copolymer bilayers" *Nat. Commun.* **2015**, *6*, 6392.

Chapter 4: La, Y.; An, T. H.; Shin, T. J.; Park, C.; Kim. K. T. "A morphological transition of inverse mesophases of a branched-linear block copolymer guided by using cosolvents" *Angew. Chem. Int. Ed.* **2015**, *54*, 10483–10487.

1.9 References

1. Du. N.; Robertson, G. P.; Song, J.; Pinnau, I.; Thomas, S.; Guiver, M. D. Polymers of Intrinsic Microporosity Containing Trifluoromethyl and Phenylsulfone Groups as Materials for Membrane Gas Separation. *Macromolecules* **2008**, *41*, 9656–9662.
2. Rzayev, J.; Hillmyer, M. A. Nanoporous Polystyrene Containing Hydrophilic Pores from an ABC Triblock Copolymer Precursor. *Macromolecules* **2005**, *38*, 3–5.
3. Shannon, M. A.; Bohn, P. W.; Elimelech, M.; Georgiadis, J. G.; Marinas, B. J.; Mayers, A. M. Science and technology for water purification in the coming decades. *Nature* **2008**, *452*, 301–310.
4. Tseng, W. H.; Chen, C. K.; Chiang, Y. W.; Ho, R. M.; Akasaka, S.; Hasegawa, H. Helical Nanocomposites from Chiral Block Copolymer Templates. *J. Am. Chem. Soc.* **2009**, *131*, 1356–1357.
5. Melde, B. J.; Burkett, S. L. Silica Nanostructures Templated by Oriented Block Copolymer Thin Films Using Pore-Filling and Selective-Mineralization Routes. *Chem. Mater.* **2005**, *17*, 4743–4749.
6. Yang, S. Y.; Ryu, I.; Kim, H. Y.; Kim, J. K. Jang, S. K.; Russell, T. P. Nanoporous Membranes with Ultrahigh Selectivity and Flux for the Filtration of Viruses. *Adv. Mater.* **2006**, *18*, 709–712.
7. Wu, D.; Xu, F.; Sun, B.; Fu, R.; He, H.; Matyjaszewski, K. Design and Preparation of Porous Polymers *Chem. Rev.* **2012**, *112*, 3959–4015.
8. Kulkarni, C. V.; Wachter, W.; Iglesias-Salto, G.; Engelskirchen, S.; Ahualli, S. Monoolein: a Magic Lipid? Phys. *Chem. Chem. Phys.* **2011**, *13*, 3004–3021.
9. Negrini, R.; Mezzenga, R. Diffusion, Molecular Separation, and Drug Delivery from Lipid Mesophases with Tunable Water Channels. *Langmuir* **2012**, *28*, 16455–16462.
10. Ahmed, F.; Photos, P. J.; Discher, D. E. Polymersomes as Viral Capsid Mimics. *Drug Dev. Res.* **2006**, *67*, 4-14.
11. McKenzie, B. E.; Nudelman, F.; Bomans, P. H. H.; Holder, S. J.; Sommerjijk, N. A. J. M. Temperature-Responsive Nanospheres with Bicontinuous Internal Structures from a Semicrystalline Amphiphilic Block Copolymer. *J. Am. Chem. Soc.* **2012**, *132*, 10256–10259.
12. Matyjaszewski, K.; Xia, J. Atom Transfer Radical Polymerization. *Chem. Rev.* **2001**, *101*, 2921–2990.
13. Borner. H. G.; Beers, K. Matyjaszewski, K. Synthesis of Molecular Brushes with Block Copolymer Side Chains Using Atom Transfer Radical Polymerization. *Macromolecules* **2001**, *34*, 4375–4383.
14. Blasco, E.; Barrio, J. D.; Pinol, M.; Oriol, L.; Berges, C.; Sanchez, C.; Alcala, R.

Azobenzene-Containing Linear-Dendritic Block Copolymers Prepared by Sequential ATRP and Click Chemistry. *Polymer* **2012**, *53*, 4604–4613.

15. Ding, H.; Park, S.; Zhong, M.; Pan, x.; Pietrasik, J.; Bettinger, C. J.; Matyjaszewski, K. Facile Arm-First Synthesis of Star Block copolymers via ARGET ATRP with ppm Amounts of Catalyst. *Macromolecules* **2016**, *49*, 6752–6760.
16. Jeong, M. G.; van Hest, J. C. M.; Kim, K. T. Self-Assembly of Dendritic-Linear Block Copolymers with Fixed Molecular Weight and Block Ratio. *Chem. Commun.* **2012**, *48*, 3590–3592.
17. Zhang, J.; Li, X.; Li, X. Stimuli-Triggered Structural Engineering of Synthetic and Biological Polymeric Assemblies. *Prog. Polym. Sci.* **2012**, *37*, 1130–1176.
18. Kim, H.; Kang, Y. J.; Kang, S.; Kim, K. T. Monosaccharide-Responsive Release of Insulin from Polymersomes of Polyboroxole Block Copolymers at Neutral pH. *J. Am. Chem. Soc.* **2012**, *134*, 4030–4033.
19. Zhang, L.; Eisenberg, A. Multiple Morphologies of "Crew-Cut" Aggregates of Polystyrene-*b*-poly(acrylic acid) Block Copolymers. *Science* **1995**, *268*, 1728–1731.
20. Mai, Y.; Eisenberg, A. Self-Assembly of Block Copolymers. *Chem. Soc. Rev.* **2012**, *41*, 5969–5985.
21. Percec, V. et al. Self-Assembly of Janus Dendrimers into Uniform Dendrimersomes and Other Complex Architectures. *Science* **2010**, *328*, 1009–1014.
22. Elsabahy, M.; Wooley, K. L. Design of Polymeric Nanoparticles for Biomedical Delivery Applications. *Chem. Soc. Rev.* **2012**, *41*, 2545–2561.
23. Holder, S. J.; Sommerdijk, N. A. J. M. New Micellar Morphologies from Amphiphilic Block Copolymers: Disks, Toroids, and Bicontinuous Micelles. *Polym. Chem.* **2011**, *2*, 1018–1028.
24. Scharcher, F. H.; Rupar, P. A.; Manners, I. Functional Block Copolymers; Nanostructured Materials with Emerging Application. *Angew. Chem. Int. Ed.* **2012**, *51*, 7898–7921.
25. Hales, K.; Chen, Z.; Wooley, K. L.; Pochan, D. J. Nanoparticles with Tunable Internal Structure from Triblock Copolymers of PAA-*b*-PMM-*b*-PS. *Nano Lett.* **2008**, *8*, 2023–2026.
26. Jain, S.; Bates, F. S. On the Origin of Morphological Complexity in Block Copolymer Surfactants. *Science* **2003**, *300*, 460–464.
27. Won, Y.-Y.; Davis, H. T.; Bates, F. S. Giant Wormlike Bubber Micelles. *Science* **1999**, *293*, 960–963.
28. Pochan, D. J.; Chen, Z.; Cui, H.; Hales, K.; Qi, K.; Wooley, K. L. Toroidal Triblock Copolymer Assembly. *Science* **2004**, *306*, 94–97.
29. Seddon, J. M.; Robins, J.; Gulik-Krzywicki, T.; Delacroix, H. Inverse Micellar Phases of Phospholipids and Glycolipids. *Phys. Chem. Chem. Phys.* **2000**, *2*, 4485–4493.
30. Qui, H.; Caffrey, M. The Phase Diagram of the Monoolein/Water System: Metastability and

Equilibrium Aspects. *Biomaterials* **2000**, *21*, 223–234.

31. Deng, Y.; Mieczkowski, M. Three-Dimensional Periodic Cubic Membrane Structure in the Mitochondria of Amoebae Chaos Carolinensis. *Protoplasma* **1998**, *204*, 16–25.
32. Mackay, A. L. Periodic Minimal Surfaces in Bicontinuous Lipid-Water Phases and Nanoparticles. *Curr. Opin. Colloid Interface Sci.* **2005**, *9*,365–369.
33. Larsson, K. Two Cubic Phases in Monoolein-Water System. *Nature* **1983**, *304*, 664.
34. Benedicto, A. D.; O'Brien, D. F. Bicontinuous Cubic Morphologies in Block Copolymers and Amphihpilie/Water Systems: Mathematical Description through the Minimal Surfaces. *Macromolecules* **1997**, *30*, 3395–3402.
35. Larsson, K. Cubic Lipid-Water Phases: Structures and Biomembrane Aspects. *J. Phys. Chem.* **1989**, *93*, 7304–7314.
36. Gustafsson, J.; Ljusberg-Wahren, H.; Almgren, M.; Larsson, K. Submicron Particles of Reversed Lipid Phases in Water Stabilized by a Nonionic Amphiphilic Polymer. *Langmuir* **1997**, *13*, 6964–6971.
37. Barauskas, J.; Johnsson, M.; Tiber, F. Self-Assembled Lipid Superstructures: Beyond Vesicles and Liposomes. *Nano Lett.* **2015**, *5*, 1615–1619.
38. Demurtas, D.; Guichard, P.; Martiel, I.; Mezzenga, R.; Hebert, C.; Sagalowicz, L. Direct Visualization of Dispersed Lipid Bicontinuous Cubic Phases by Cryo-Electron Tomography. *Nat. Commun.* **2015**, *6*, 8915.
39. Parry, A. L.; Bomans, P. H. H.; Holder, S. J.; Sommerdijk, N. A. J. M. Biagini, S. C. G. Cryo Electron Tomography Reveals Confined Complex Morphologies of Tripeptide-containing Amphiphilic Double-Comb Diblock Copolymers. *Angew. Chem. Int. Ed.* **2008**, *47*, 8859–8862.
40. Phillip W. A.; Hillmyer, M. A.; Cussler, E. L. Cylinder Orientation Mechanism in Block Copolymer Thin Films Upon Solvent Evaporation. *Macromolecules* **2010**, *43*, 7763–7770.
41. Peinemann, K. V.; Abetz, V.; Simon, P. F. W. Asymmetric Superstructure Formed in a Block Copolymer via Phase Separation. *Nat. Mater.* **2007**, *6*, 992–996.
42. Dorin, R. M; Sai, H.; Wiesner, U. Hierarchically Porous Materials from Block Copolymers. *Chem. Mater.* **2014**, *26*, 339–347.
43. Losic, D.; Mitchell, J. G.; Voelcker, N. H. Complex Gold Nanostructures Derived by Templating from Diatom Frustules. *Chem. Commun.* **2005**, *0*, 4905–4907.
44. Shi, Y.; Wan, Y.; Zhao, D. Ordered Mesoporous Non-Oxide Materials. *Chem. Soc. Rev.* **2011**, *40*, 3854–3878.
45. Lu, Y. et al. Continuous Formation of Supported Cubic and Hexagonal Mesoporous Films by Sol-Gel Dip-Coating. *Nature* **1997**, *389*, 364–368.
46. Kresge, C. T.; Leonowicz, M. E.; Roth, W. J.; Vartuli, J. C.; Beck, J. S. Ordered Mesoporous Molecular Sieves Synthesized by a Liquid-Crystal Templated Mechanism. *Nature* **1992**, *359*,

710–712.

47. Zhao, D.; Feng, J.; Huo, Q.; Melosh, N.; Fredrickson, G. H.; Chmelka, B. F.; Stucky, G. D. Triblock Copolymer Syntheses of Mesoporous Silica with Periodic 50 to 300 Angstrom Pores. *Science* **1998**, *279*, 548–552.
48. Chen, X.; Mao, S. S. Titanium Dioxide Nanomaterials: Synthesis, Properties, Modifications, and Applications. *Chem. Rev.* **2007**, *107*, 2891–2959.
49. Li, W.; Wu, Z.; Wang, J.; Elzatahry, A. A.; Zhao, D. A Perspective on Mesoporous TiO_2 Materials. *Chem. Mater.* **2014**, *26*, 287–298.
50. Steiner, U. et al. A 3D Optical Metamaterial Made by Self-Assembly. *Adv. Mater.* **2012**, *24*, 24–27.
51. Saranathan, V.; Osuji, C. L.; Mochrie, S. G. J.; Noh, H.; Narayanan, S.; Sandy, A.; Dufresne, E. R.; Prum, R. O. Structure, Function, and Self-Assembly of Single Network Gyroid ($I4_132$) Photonic Crystals in Butterfly Wing Scales. *Proc. Natl. Acad. Sci. U. S. A.* **2010**, *107*, 11676–11681.
52. Saranathan, V.; Seago, A. E.; Sandy, A.; Narayanan, S.; Mochrie, S. G. J.; Dufresne, E. R.; Cao, H.; Osuji, C. O.; Prum, R. O. Structural Diversity of Arthropod Biophotonic Nanostructures Spans Amphiphilic Phase-Space. *Nano Lett.* **2015**, *15*, 3735–3742.

Chapter 2. Colloidal inverse bicontinuous cubic membranes of block copolymers with tunable surface functional groups

2.1 Abstract

Analogous to the complex membranes found in cellular organelles, such as the endoplasmic reticulum, the inverse cubic mesophases of lipids and their colloidal forms (cubosomes) possess internal networks of water channels arranged in crystalline order, which provide a unique nanospace for membrane-protein crystallization and guest encapsulation. Polymeric analogues of cubosomes formed by the direct self-assembly of block copolymers in solution could provide new polymeric mesoporous materials with a three-dimensionally organized internal maze of large water channels. Here we report the self-assembly of amphiphilic dendritic–linear block copolymers into polymer cubosomes in aqueous solution. The presence of precisely defined bulky dendritic blocks drives the block copolymers to form spontaneously highly curved bilayers in aqueous solution. This results in the formation of colloidal inverse bicontinuous cubic mesophases. The internal networks of water channels provide a high surface area with tunable surface functional groups that can serve as anchoring points for large guests such as proteins and enzymes.

2.2 Introduction

Synthesized by covalently connecting both the hydrophilic and hydrophobic blocks, amphiphilic block copolymers self-assemble in solution to form polymer micelles and vesicles in an analogous fashion to lipids. Previously, precise control of the size, shape, and function of these polymer nanostructures has been demonstrated by adjusting the molecular architecture of the block copolymers. The design rules for this were drawn using an analogy to the relationship between the molecular architecture and the morphology of lipidic assemblies.[1-7] In addition to the morphological diversity, recent efforts have been placed on polymer micelles and vesicles with the well-defined internal order within the hydrophobic compartment. Such an ordered array of chemical components is expected to offer benefits for potential applications, for example, biochemical reactors, delivery vehicles, and nanotemplates.[8-12] In an analogous fashion to the templated synthesis of inorganic mesoporous materials, these compositional arrays could be translated into physical structures, such as a mesoporous network, by selectively removing the labile polymer domains.[13,14] The direct formation of mesoporous polymers is highly desirable,[15] but has remained a challenge, especially for the solution self-assembly of block copolymers.

A binary mixture of water and lipid, such as GMO, exhibits the formation of various inverse bicontinuous crystalline phases, in which the infinite network of water channels is arranged into crystalline lattices.[16,17] These lipid cubic membranes are found in cellular organelles such as the

endoplasmic reticulum.[18] Colloidal forms of cubic lipid membranes also appear transiently during fat digestion processes that convert oil into lipids.[19] These complex lipid bilayers have attracted recent attention, in particular for their structural characteristics.[18,20] The inverse cubic mesophases of lipids and their colloidal forms (cubosomes)[21,22] provide a unique nanospace for membrane-protein crystallization and guest encapsulation.[23– 26] In solution, block copolymers behave in an analogous fashion to lipids with a greater length scale, which results in micellar and vesicular structures with the desired chemical and physical properties. In this respect, the self-assembly of block copolymers to give cubosome structures is an attractive goal. Polymeric counterparts of these structures could lead to the direct access of highly defined mesoporous polymer materials with the desired physical and chemical properties owing to the diverse chemical structures of block-copolymer building blocks.

Block copolymers may form inverse cubic mesophases in concentrated solution.[27–29] Analogues of cubosomes have been observed previously from the self-assembly of synthetic macromolecules such as triblock copolymers, semi-crystalline brushed block copolymers and dendritic amphiphiles.[8,30–35] In spite of these reports, a clear rationale that underlies the self-assembly of block copolymers to give inverse mesophases in solution has not been proposed.[36] Consequently, the design of block copolymers to form preferentially complex bilayers and inverse mesophases in solution remains unexplored. We describe here the direct self-assembly of dendritic–linear block copolymers in aqueous solution into colloidal particles of bicontinuous cubic membranes (polymer cubosomes) with the desired crystalline lattice. Three inverse bicontinuous cubic phases (primitive cubic, double diamond, and gyroid) were identified from the polymer cubosomes of our dendritic–linear block copolymers depending on the architecture of the dendritic scaffold in the hydrophilic block. Our experimental results strongly suggest that the presence of an accurately defined dendritic architecture in the hydrophilic block is a key structural element of the solution self-assembly of amphiphilic block copolymers into inverse bicontinuous mesophases. We also show that the bilayer membranes consisting of polymer cubosomes can be equipped with desired surface functional groups, which makes polymer cubosomes an interesting porous platform to host macromolecular guests such as proteins and enzymes.

2.3 Results and discussion

Self-assembly of dendritic–linear block copolymers into polymer cubosomes. In this study, we synthesized isomers of second-generation benzyl ether dendrons with six water-soluble peripheral poly(ethylene glycol) (PEG) chains (Figure 2-1). Each peripheral PEG chain had the same number-average molecular weight (M_n) of 350 g mol^{-1} (number of repeat units or degree of polymerization (DP_n) was seven). These dendritic isomers were converted into macroinitiators for the atom transfer radical polymerization of styrene.[37] The hydrophobic polystyrene (PS) block was grown from the focal point of the hydrophilic dendrons with a controlled molecular weight and narrow size

distribution. The DP_n of the PS blocks was controlled to fit a range of about 180-240, so that the block ratio of the resulting dendritic–linear block copolymers, defined as the ratio of the molecular weight of the PEG domain to that of the PS block (f_{PEG}), was in the range of about 8-11% to ensure that the block copolymers predominantly self-assemble into bilayer structures.[38]

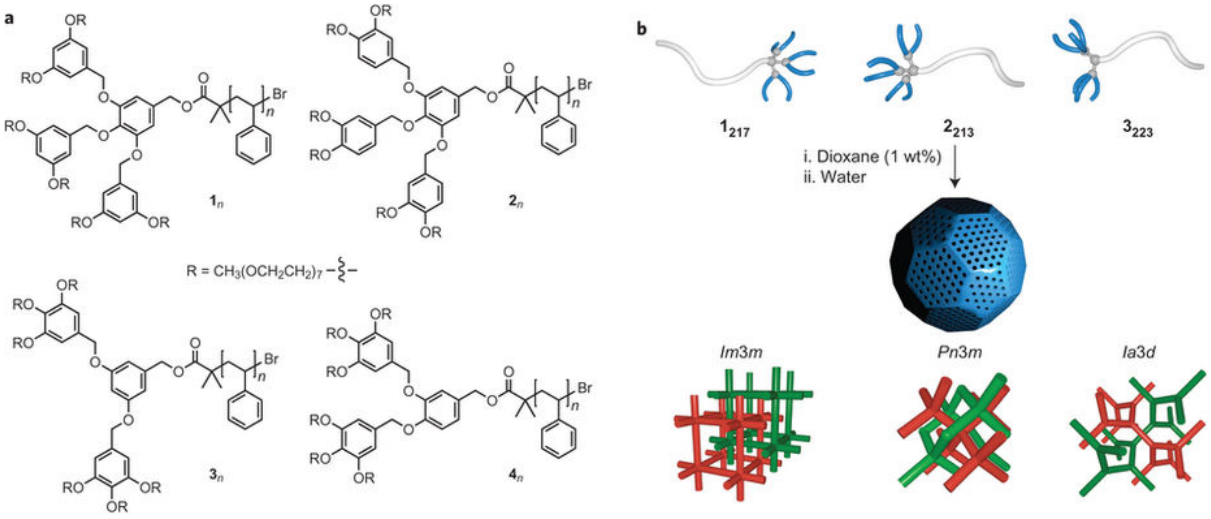

Figure 2-1. Chemical structures and schematic diagrams of dendritic-linear block copolymers and their self-assembly. (a) Chemical structures of block copolymers 1_n and 2_n constructed from the two isomers of benzyl ether dendrons that possess peripheral PEG chains at the 3,5-positions (1_n) and 3,4-positions (2_n) of the outer phenyl groups, and 3_n and 4_n built from dendritic blocks that consist of two peripheral 3,4,5-PEG-benzyl ether units at the 3,5 (3_n) and 3,4 (4_n) positions of the central benzyl unit. The subscript *n* denotes the DP of the PS block. (b) A schematic representation of the self-assembly of dendritic-linear block copolymers into polymer cubosomes in dilute aqueous solution. The lattice diagrams at the bottom show bicontinuous cubic internal structures of the polymer cubosomes (*Im3m*, *Pn3m* and *Ia3d*) investigated in this study. For clarity, the bilayers that surround the water channels are omitted. The green- and red-colored regions indicate two non-intersecting networks of water channels within the bicontinuous structures.

All block copolymers were self-assembled by a simple cosolvent method[5]: to a 1,4-dioxane solution of a block copolymer (typically 1 wt%) was added an equal volume of water for a period of two hours, followed by a dialysis against water. We first studied aqueous suspension solutions prepared from a series of dendritic-linear block copolymers 1_n. On transmission electron microscopy (TEM), the suspension solution of 1_{185} (M_n = 19,100 g mol^{-1}, polydispersity index ($Đ$) = 1.09, f_{PEG} = 10.9%) showed bilayer structures, flat and folded lamella, along with polymer vesicles (Figure 2-2). However, on the increase in the length of the PS block, the block copolymer 1_{217} (M_n = 21,300 g mol^{-1}, $Đ$ = 1.07, f_{PEG} = 9.3%) formed large colloidal particles with an average diameter of 6.2 μm (polydispersity (PD)

= 0.27), as determined by dynamic light scattering (DLS) measurements (Figure 2-3).

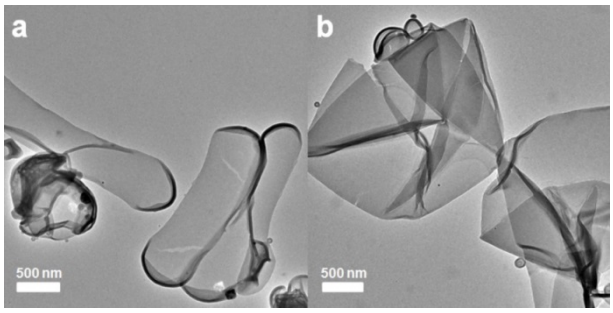

Figure 2-2. TEM images of self-assembled structures from the suspension solution of 1_{185}. (a) Flat lamella structures. (b) Folded lamella structures.

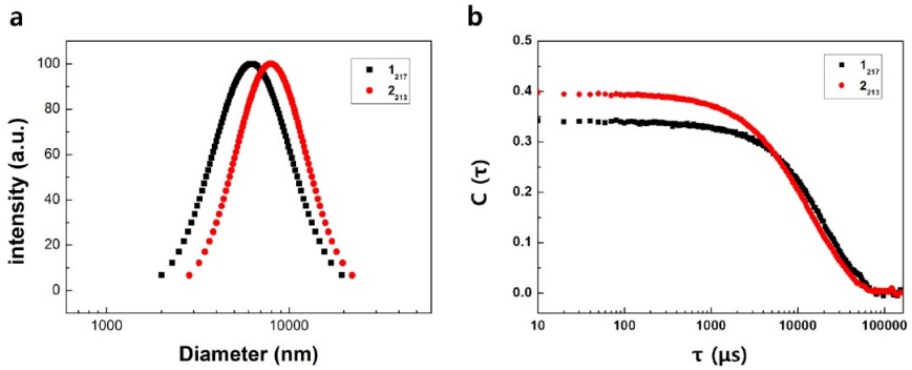

Figure 2-3. (a) Size distributions and (b) autocorrelation functions of the suspensions of 1_{217} and 2_{213}. The average diameter of 1_{217} and 2_{213} were 6.2 μm (dispersity 0.27) and 7.9 μm (0.22), respectively.

The detailed morphology of the colloidal particles was studied using TEM and scanning electron microscopy (SEM). The TEM images of the dried suspension of 1_{217} showed colloidal particles (Figure 2-4a) that had bicontinuous internal structures resembling those seen in cryogenic TEM images of lipid cubosomes.[39] Therefore, owing to this structural similarity, we named our colloidal particles as polymer cubosomes.[8,32] The SEM images of the polymer cubosomes of 1_{217} (coated with a 3 nm thick layer of Pt) clearly revealed details of their hierarchical structure. Low-resolution SEM images showed spherical polymer cubosomes with an average diameter corresponding to that obtained with DLS (Figure 2-4c). To our surprise, high-resolution SEM (HR-SEM) images revealed that the polymer cubosomes had bicontinuous internal structures enclosed in a perforated lamellar shell, the surface of which was inundated with evenly distributed pores approximately 10 nm in diameter (Figure 2-4e). From the SEM and TEM images, the thickness of the perforated shell was estimated to be 15 nm, which suggests that it was a bilayer of 1_{217} (Figure 2-5). SEM images of the polymer cubosomes that fractured during the sample preparation showed a highly ordered crystalline structure residing in the perforated bilayer shell (Figure 2-5 and 2-6a), which was consistent with the TEM observations.

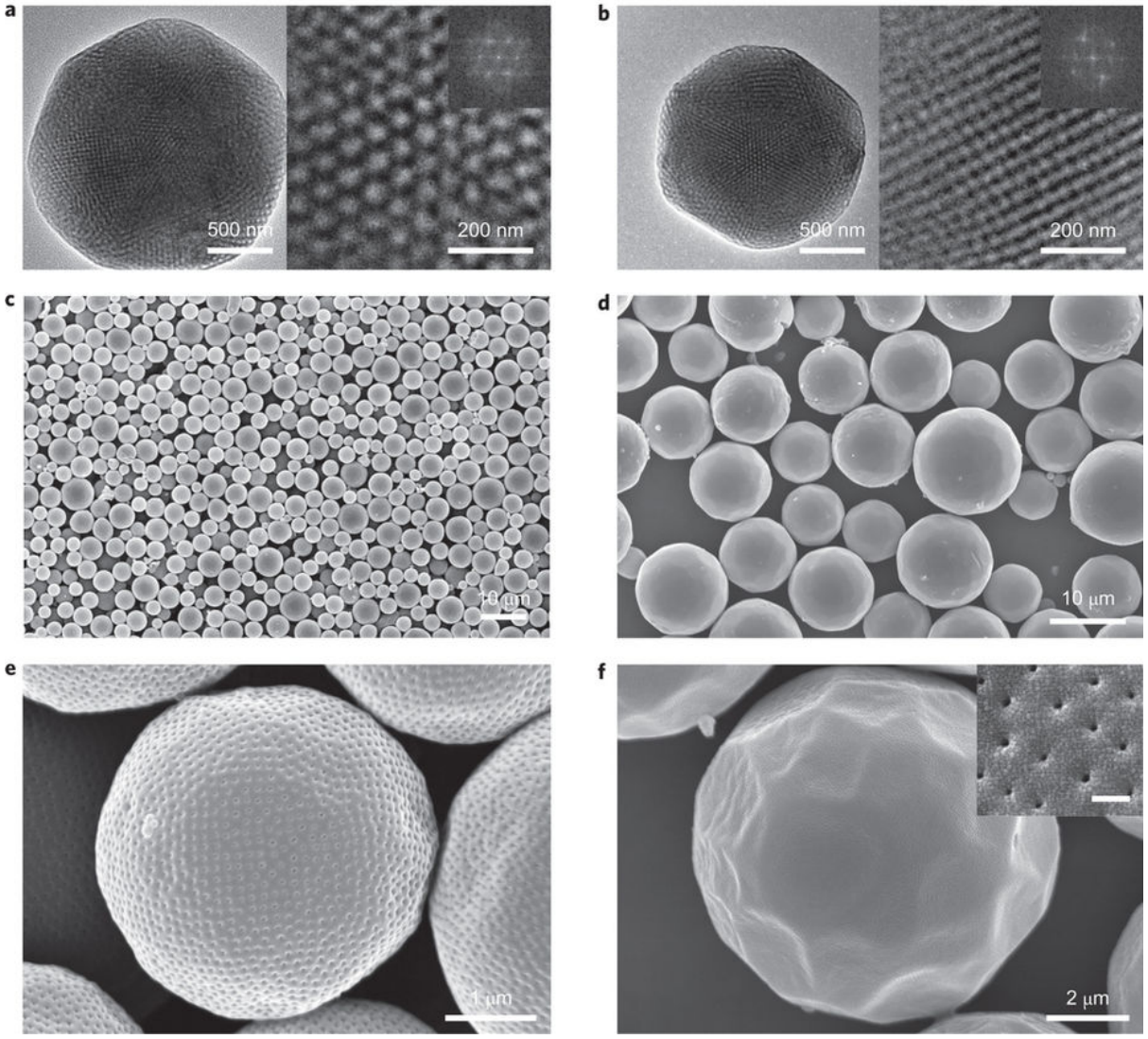

Figure 2-4. Representative SEM and TEM images of the polymer cubosomes. (a) TEM images showing the internal structure of the polymer cubosomes of 1_{217} (left). The magnified view of the internal structures and the fast Fourier transform (FFT) (inset) show a cubic (*Im3m*) lattice viewed in the [111] direction (right). (b) TEM images of polymer cubosomes of 2_{213}. The right image shows the view of a double diamond (*Pn3m*) lattice viewed in the [001] direction and the FFT of the image. (c, d) Low-magnification SEM images of polymer cubosomes of 1_{217} (c) and 2_{213} (d). (e) SEM image of the polymer cubosome of 1_{217} showing a spherical morphology and the perforated shell enclosing the internal bicontinuous structure. (f) SEM images of the polymer cubosomes of 2_{213}. The inset shows a magnified view of the surface pores (scale bar, 100 nm).

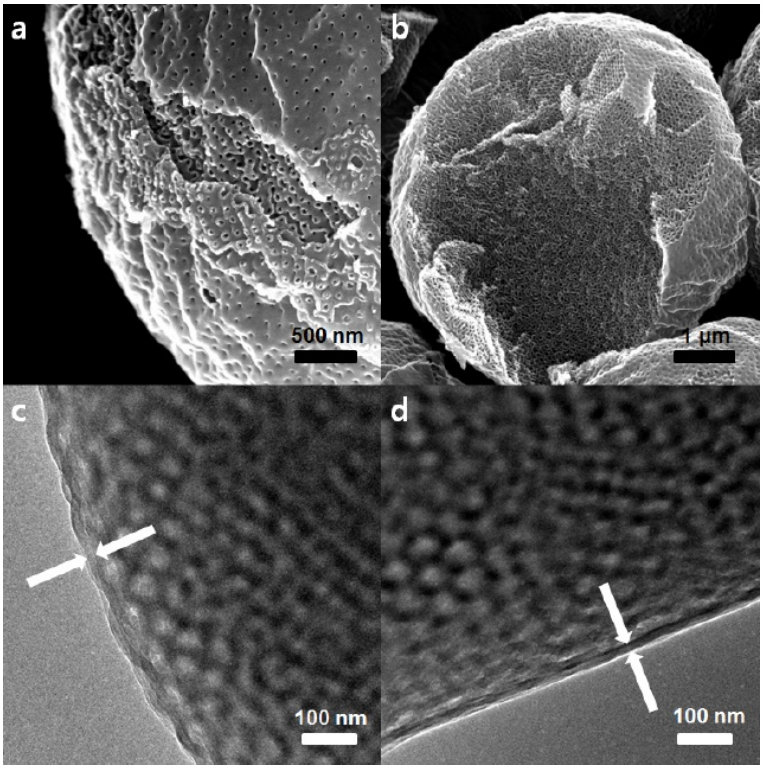

Figure 2-5. (a, b) SEM and (c, d) TEM images showing the perforated lamellar shell structures of the polymer cubosomes of 1_{217}. Arrows indicate the thicknesses of the lamellar shells (14.7 nm in c, 14.9 nm in d).

The internal order of the polymer cubosomes of 1_{217} was studied using synchrotron small-angle X-ray scattering (SAXS, PLS-II 9A beamline). The SAXS results of the dried polymer cubosomes of 1_{217} showed a set of peaks that corresponded to the primitive cubic (*Im3m*) symmetry (lattice parameter (a) = 93.4 nm (Figure 2-6c)), which was in agreement with the TEM and SEM images and confirmed the presence of a highly regular and long-range cubic arrangement of water channels. The structural hierarchy of the polymer cubosomes of 1_{217}, with a bicontinuous cubic internal structure enclosed within a perforated bilayer shell, suggested that the polymer cubosomes should be mesoporous on withdrawal from the water. Under ambient conditions, it was found that the dried polymer cubosomes were physically robust because of the high glass-transition temperature (T_g) of the hydrophobic PS block of high molecular weight (T_g = 101 °C). The mesoporous nature of the dried polymer cubosomes of 1_{217} were substantiated by N_2-adsorption experiments at 77 K. Type IV adsorption isotherms with type H2 hysteresis loops were observed, with a Brunauer– Emmett–Teller (BET) surface area of 112 $m^2\ g^{-1}$ and a pore volume of 1.01 $cm^3\ g^{-1}$ (Figure 2-6e), The Barrett–Joyner Halenda (BJH) pore-size distribution curve showed a broad range of pores with a peak diameter of 50 nm (Figure 2-7).

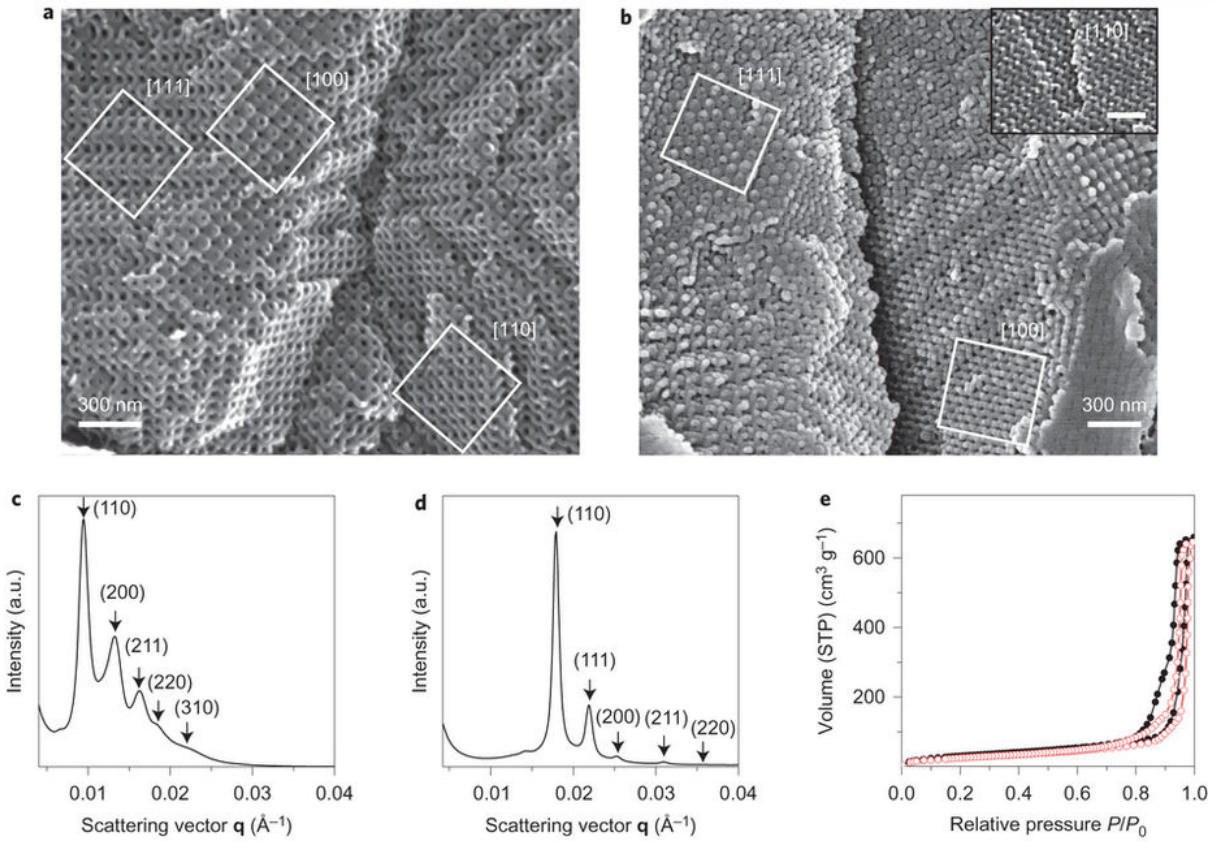

Figure 2-6. Structural analysis of the polymer cubosomes. (a) HR-SEM image of the bicontinuous cubic internal structure of the polymer cubosome of 1_{217} having a primitive cubic (*Im3m*) lattice. The internal structures were observed from the fractured polymer cubosomes during the sample preparation. The views in the [100], [110] and [111] directions are highlighted by white squares. (b) HR-SEM images of a double diamond (*Pn3m*) internal structure of the polymer cubosomes of 2_{213}. Views in the [111] and [100] directions are highlighted by white squares. The inset shows a view in the [110] direction (scale bar, 200 nm). (c) The SAXS result of the dried polymer cubosomes of 1_{217}, which indicates the primitive cubic (*Im3m*) lattice (lattice parameter, a = 93.4 nm). (d) The SAXS result of the dried polymer cubosomes of 2_{213} shows the double diamond (Pn3m) lattice (a = 49.5 nm). (e) N_2 adsorption-desorption isotherms of the dried polymer cubosomes of 1_{217} (filled circles) and 2_{213} (open circles) measured at 77 K. a.u., arbitrary units; STP, standard temperature and pressure.

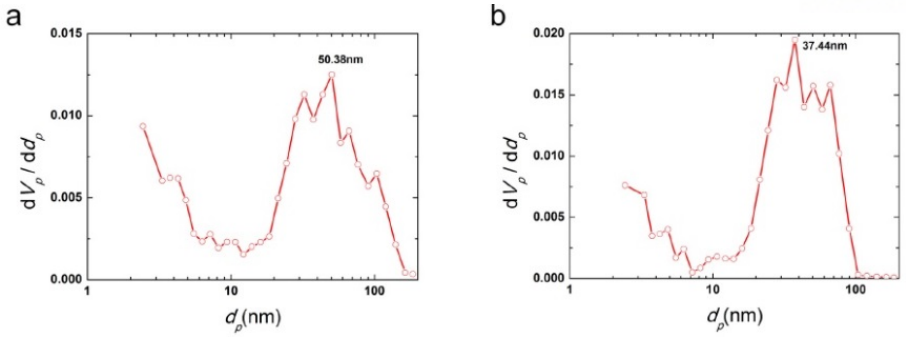

Figure 2-7. BJH pore size distributions of polymer cubosomes of (a) 1_{217} and (b) 2_{213}.

The effect of the architecture of block copolymers on self-assembly. Based on these findings, we surmised that a change in the architecture of the dendritic block, with the length of the PS block kept constant, might enable controlled alteration of the molecular packing of the block copolymers in the condensed phase. As the molecular weights of both dendritic and PS blocks are fixed to constant values, this change would differentiate the local curvature without radically altering the overall morphology of self-assembled bilayers,[37] which could induce phase transitions between different bicontinuous cubic phases. This assumption might be justified by Langmuir isotherm experiments carried out on two structural isomers, 1_{217} and 2_{213} (M_n = 21,300 g mol^{-1}, D = 1.08, f_{PEG} = 9.4% (Figure 2-1)), which gave the area per molecule in a monolayer at an air-water interface of 1,370 Å^2 for 1_{217} and 1,530 Å^2 for 2_{213} (Figure 2-8). The linear diblock copolymer with similar molecular weights on both blocks (PEG_{45}–PS_{210}) showed a molecular area of 950 Å^2.

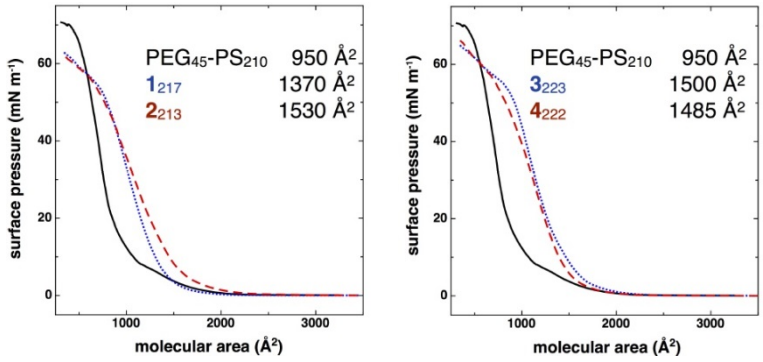

Figure 2-8. Surface pressure to molecular area (π-A) isotherms of a linear block copolymer and dendritic-linear block copolymers at 300 K.

TEM images of the aqueous suspension of 2_{213}, prepared under the same conditions as for 1_{217}, showed polymer cubosomes (average diameter 7.9 μm, PD = 0.22, determined by DLS) (Figure 2-3) with structural characteristics similar to those of 1_{217} (Figure 2-4b). SEM images of the polymer cubosomes of 2_{213} showed the presence of an internal structure of the double diamond lattice (*Pn3m*) (Figure 2-6b), which was later confirmed by the SAXS results obtained from the dried polymer

cubosomes of 2_{213} (a = 49.5 nm (Figure 2-6d)). The dried polymer cubosomes of 2_{213} were also found to be mesoporous by N_2-adsorption experiments at 77 K (BET surface area of 101 m^2 g^{-1} and pore volume of 0.99 cm^3 g^{-1}, a peak pore diameter of 37 nm from the BJH curve (Figure 2-6e and 2-7)).

Encouraged by this result, we decided to investigate further the possibility of finding other inverse mesophases by synthesizing another set of block copolymers, 3_n and 4_n, built from the hydrophilic dendritic blocks with two peripheral 3,4,5-PEG-benzyl ether units at the 3,5- (3n) and 3,4- (4n) positions of the central benzyl unit, respectively (DP_n of PEG = 7 (Figure 2-1)). Under the same conditions, both block copolymers self-assembled into polymer cubosomes. SAXS and SEM studies of the polymer cubosomes of 3_{223} (M_n = 23,700 g mol^{-1}, D = 1.06, f_{PEG} = 9.1%) confirmed the internal lattice of gyroid structures (Ia3d, a = 82.3 nm (Figure 2-9)), and the polymer cubosomes of 4_{222} (M_n = 23,400 g mol^{-1}, D = 1.06, f_{PEG} = 9.1%) showed the internal bicontinuous structures of *Pn3m* symmetry (a = 52.3 nm (Figure 2-10)). These polymer cubosomes were also found to be mesoporous by N_2-adsorption/desorption experiments, which showed similar results to those obtained previously (Figure 2-9).

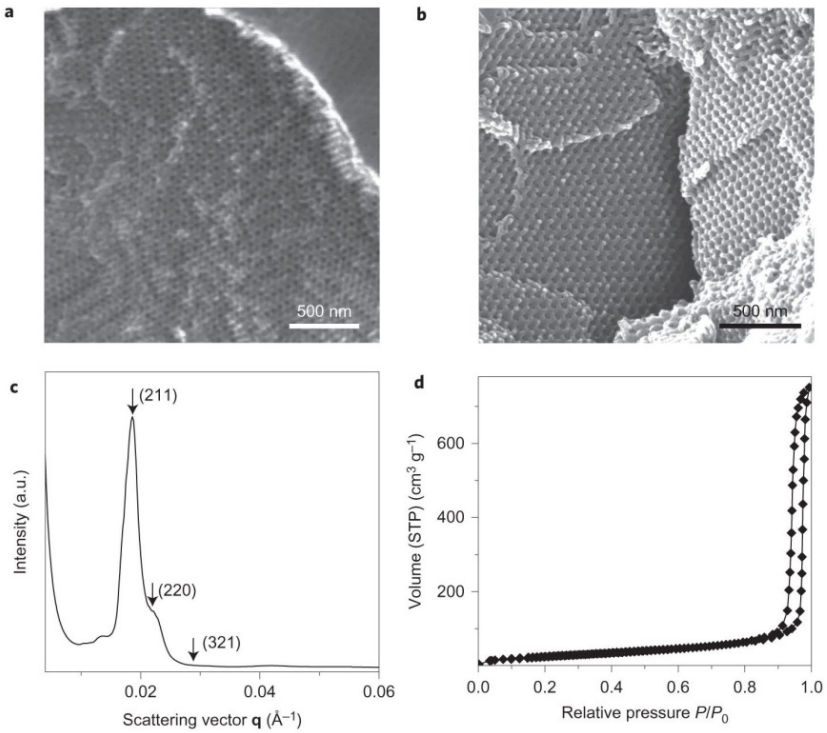

Figure 2-9. Polymer cubosomes of 3_{223}. (a, b) HR-SEM images showing the internal double-gyroid structures of the polymer cubosome of 3_{223} viewed in the [111] (a) and [110] (b) directions. (c) SAXS results of dried polymer cubosomes of 3_{223}. Peaks were assigned to Ia3d symmetry (a = 82.3 nm). (d) N_2 adsorption-desorption isotherms of the dried polymer cubosomes of 3_{223} measured at 77 K (BET surface area 99 m^2 g^{-1}, pore volume 1.16 cm^3 g^{-1}).

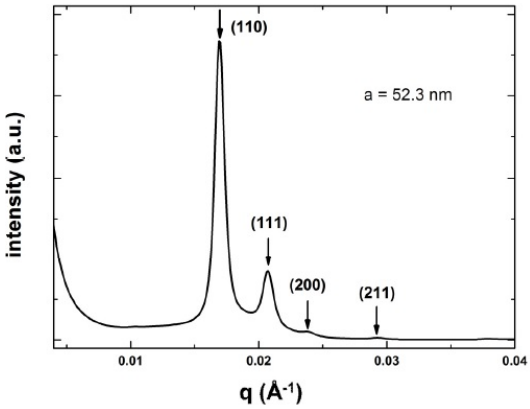

Figure 2-10. SAXS result of the dried polymer cubosomes of 4_{222} assigned to the bicontinuous cubic (Pn3m) lattice.

Given that linear diblock copolymers PEG_{45}–PS_n possessing similar f_{PEG} values to those of dendritic–linear block copolymers (n = ~180-270, f_{PEG} = ~7.1-10.6%), only formed polymer vesicles under same experimental conditions[38] (Figure 2-11), our results suggested that the presence of the dendritic benzyl ether architecture in the hydrophilic block plays an essential role in the formation of inverse bicontinuous cubic phases in dilute solution.

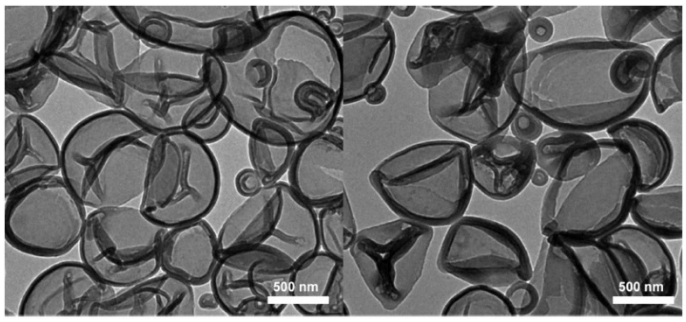

Figure 2-11. TEM images of self-assembled polymer vesicles of PEG_{45}-PS_{270}.

The structure–morphology relationship of lipidic self-assembly could be qualitatively explained by the molecular architecture of the lipid, defined by the critical packing parameter ($P = v/a_0l$, where v is the volume of the hydrophobic chain, a_0 is the effective area of a hydrophilic headgroup and l is the effective length of the molecule)[1]. As P increases, the morphology of the self-assembled structure of lipids transforms from spheres to rod-like micelles and vesicles. When P exceeds 1, the self-assembled bilayer of lipids develops a negative curvature, which results in the formation of inverse bicontinuous structures.[17,40] Our experimental results showed a close resemblance to the self-assembly of lipids such as glyceryl monooleate, which exhibited the formation of inverse bicontinuous cubic structures described as minimal surface structures of negative Gaussian curvature and include double-diamond (*Pn3m*), gyroid (*Ia3d*) and primitive cubic (*Im3m*) phases.[16,17]

Mechanism of the formation of polymer cubosomes. To investigate the details of the self-assembly of dendritic–linear block copolymers in dilute solution, we used a kinetic quenching method by taking drops (~20 μL) of suspension solution during the different stages of water addition, followed by immediate dilution with excess water (2 mL). This method enabled the capture of a snapshot of the self-assembly that resulted from vitrification of the high molecular weight PS blocks at the time of dilution with excess water. Even in the early stage of self-assembly (water content ~15%), we observed similar polymer cubosomes with less well-defined internal structures compared to those observed at a 50% water content (Figure 2-12) by TEM experiments. DLS results did not show any gradual increase of the average diameter during water addition. The reduction of the rate of water addition (20% of the typical rate) into a dioxane solution of block copolymers did not alter the internal phase, but only affected the average diameter and size distribution of polymer cubosomes. These results ruled out the possibility that the polymer cubosomes were formed during dialysis and also suggested that the formation of polymer cubosomes was a result of the direct self-assembly of dendritic–linear block copolymers into mesophases rather than that of the secondary self-assembly of bilayers or polymersomes into bicontinuous structures.

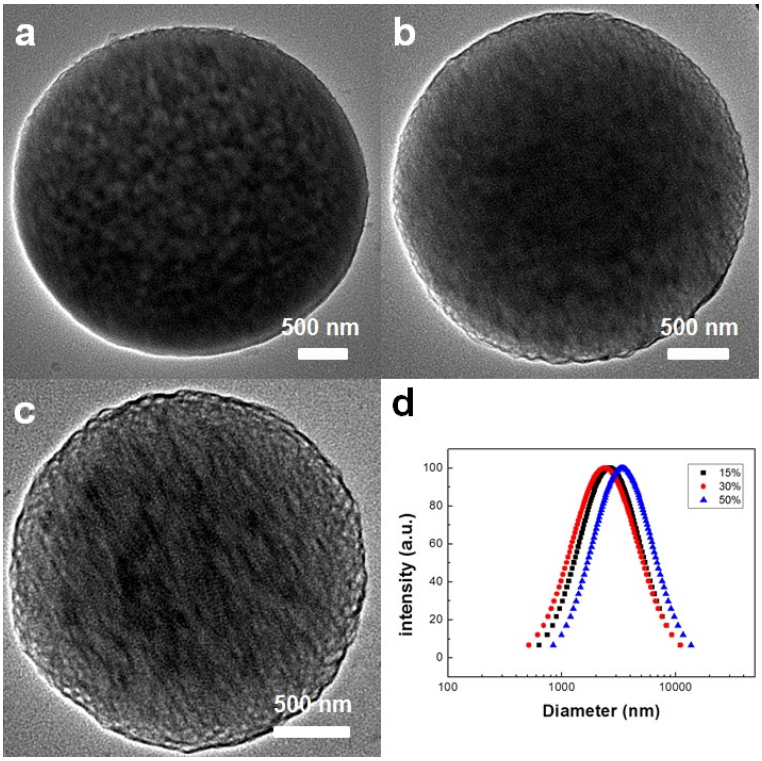

Figure 2-12. (a-c) TEM images and (d) size distributions of polymer cubosomes of 1_{217} observed from the quenched suspensions at various water contents (a, 15%, b, 30%, and c, 50%). Size distributions measured by DLS experiments indicate that the particle sizes are not correlated to the water content during self-assembly.

The phase behaviour of dendritic–linear block copolymers in aqueous solution was affected mainly by their block ratio. For example, both 1_{232} and 2_{245} (f_{PEG} of 8.9% for 1_{232} and 8.4% for 2_{245}) showed the emergence of an inverse hexagonal phase within the polymer cubosomes (Figure 2-13). The phase transition from an inverse bicontinuous cubic to an inverse hexagonal phase was more pronounced when, for example, 1_{232} was self-assembled in the presence of homo-PS (M_n = 12,000 g mol^{-1}) as an additive (10% w/w). As shown from lipidic assemblies,[39] an increase in the volume fraction of the hydrophobic compartment, caused by added hydrophobes, induced a complete phase transition of the internal structure into an inverse hexagonal internal phase, which was observed by SEM and TEM (Figure 2-14). These results indicated that self-assembled structures of dendritic– linear block copolymers undergo a morphological transition from bilayer lamellae and vesicles to inverse bicontinuous cubic structures and inverse hexagonal structures on a gradual decrease of f_{PEG} values.

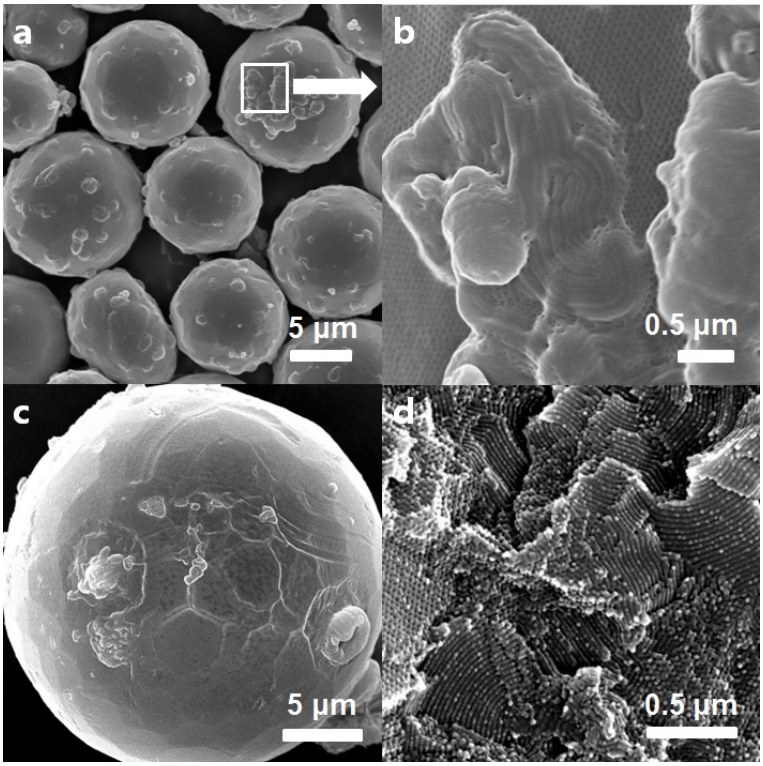

Figure 2-13. SEM images of polymer cubosomes of 1_{232} and 2_{245}. (a, b) SEM images showing the emergence of inverse hexagonal phase in the polymer cubosomes of 1_{232}. (c) The polymer cubosomes of 2_{245}. (d) The inverse hexagonal phase within the polymer cubosomes of 2_{245}.

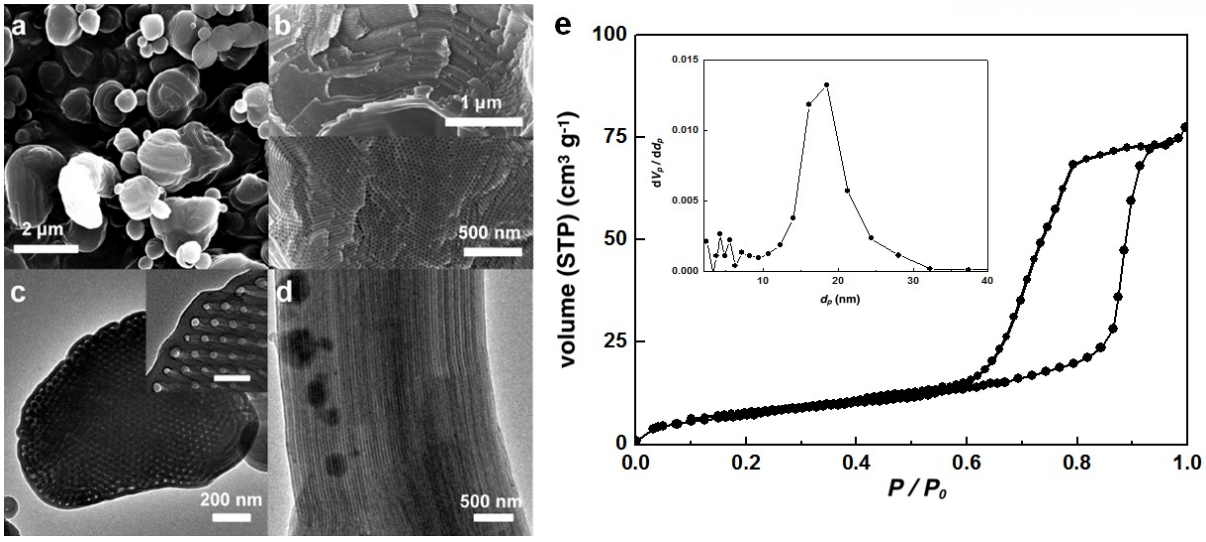

Figure 2-14. SEM and TEM and Gas adsorption profile of self-assemble structures of 1_{232} in the presence of homo PS (10% w/w) as an additive. (a) SEM image showing spiral-shape aggregates. (b) SEM images showing the inverse hexagonal phase (up) and the cross section of hexagonally packed channels (down). (c) TEM images of aggregates. The inset shows hexagonally packed channels. (scale bar = 50m) (d) TEM image showing the long-range order of inverse hexagonal phase. (e) N2 physisorption isotherms measured at 77 K. (BET surface area 27.3 m^2 g^{-1}, pore volume 0.12 cm^3 g^{-1}.). The inset shows the BJH pore size distribution (the mean pore diameter 17.4 nm).

Surface functionalization of polymer cubosomes. The polymer cubosomes reported here had a well-defined internal structure that consisted of interconnected networks of water channels arranged in a cubic crystalline order and with a surface area in excess of 100 m^2 g^{-1}. The perforated outer shell connected the internal networks of large water channels to the surroundings in all directions. To utilize the internal volume of the polymer cubosomes to accommodate large guests, such as enzymes and protein complexes, we introduced functional groups on the surface of the bilayer membranes that constituted the polymer cubosomes via the coassembly of 1_{217} and linear block copolymers that possess an α-amino (NH_2)- or thiol (SH)-functionalized PEG block (NH_2–PEG_{45}–PS_{210}, SH–PEG_{45}–PS_{210}, M_n = 23,000 g mol^{-1}, f_{PEG} = 9.2%).[41] The coassembly of 1_{217} with these end-functionalized block copolymers (up to 10% w/w) did not disrupt the crystalline lattices of the resulting functionalized polymer cubosomes as observed by SEM and TEM (Figure 2-15 and 2-16). From the molecular areas of PEG_{45}– PS_{210} (950 $Å^2$) and 1_{217} (1,370 $Å^2$) determined by Langmuir isotherms at the air-water interface, these polymer cubosomes could have up to 1.6 μmol g^{-1} of surface functional groups if 10 wt% of the end-functionalized linear block copolymers were used for coassembly.

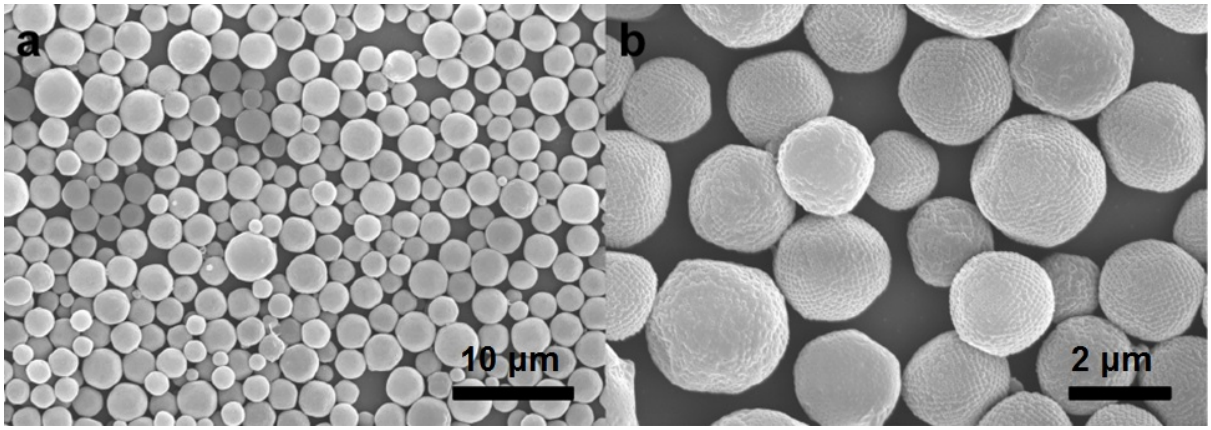

Figure 2-15. Representative SEM images of the polymer cubosomes of 1_{217}/NH_2-PEG_{45}-PS_{210} (10% w/w).

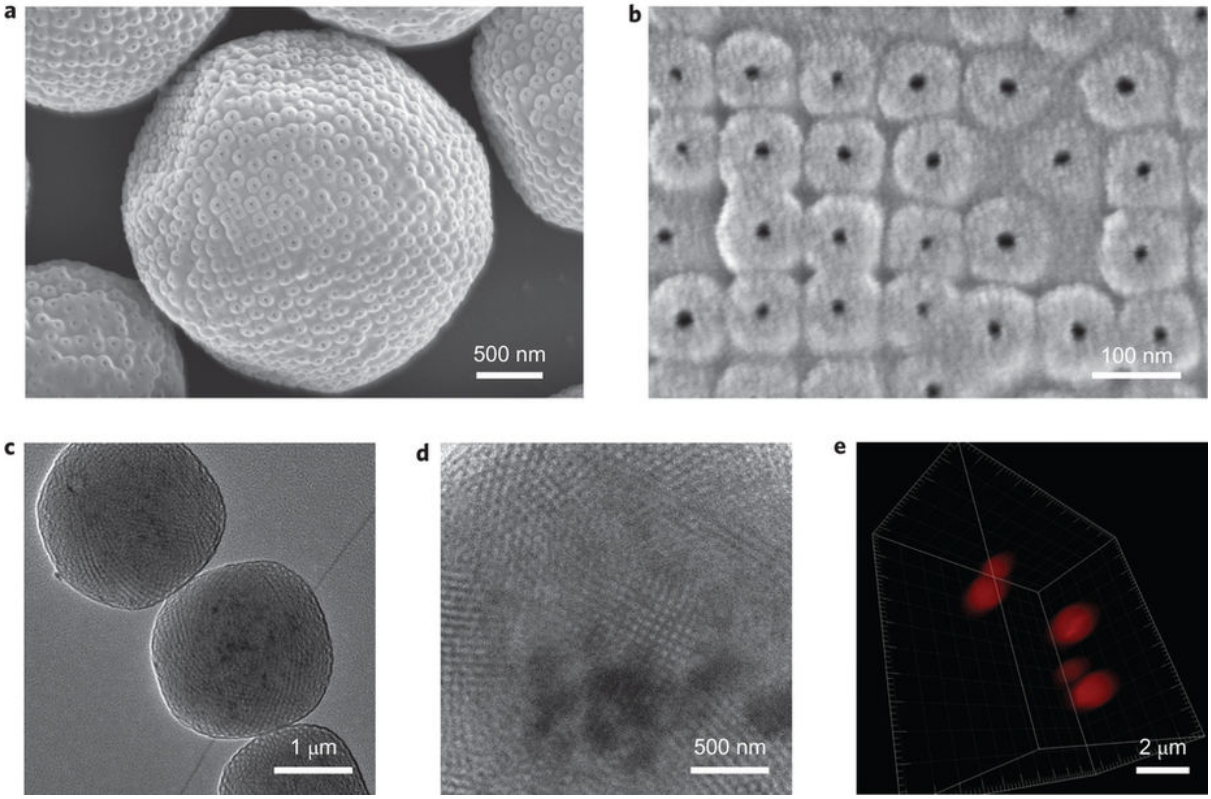

Figure 2-16. Surface-functionalized polymer cubosomes obtained from the coassembly of 1_{217} and NH_2–PEG_{45}–PS_{210} (10% w/w). (a) SEM image and (b) HR-SEM image showing the surface pores of the polymer cubosomes. (c, d) TEM images showing the internal structures of the polymer cubosomes. (e) 3D reconstructed images of CLSM of the polymer cubosomes after the reaction with Rho-NHS.

The successful incorporation of the functional groups on the internal surface of the polymer cubosomes was confirmed by confocal laser scanning microscopy (CLSM) after the covalent labelling of surface functional groups in phosphate buffer (pH 7.4) using fluorescein-5-maleimide (F-MI) for

the SH groups and rhodamine-N-hydroxy succinimidyl ester (Rho-NHS) for NH_2 groups (Figure 2-16e). Also, these functional groups could be introduced into polymer cubosomes of 1_{217} in tandem by using a mixture of NH_2–PEG_{45}–PS_{210} and SH–PEG_{45}–PS_{210} for coassembly. After orthogonally labelling these functional groups with an equimolar mixture of F-MI and Rho-NHS in the buffer, the resulting polymer cubosomes showed fluorescence of both dyes on the CLSM, which confirmed the coexistence of both functional groups in the polymer cubosomes (Figure 2-17a).

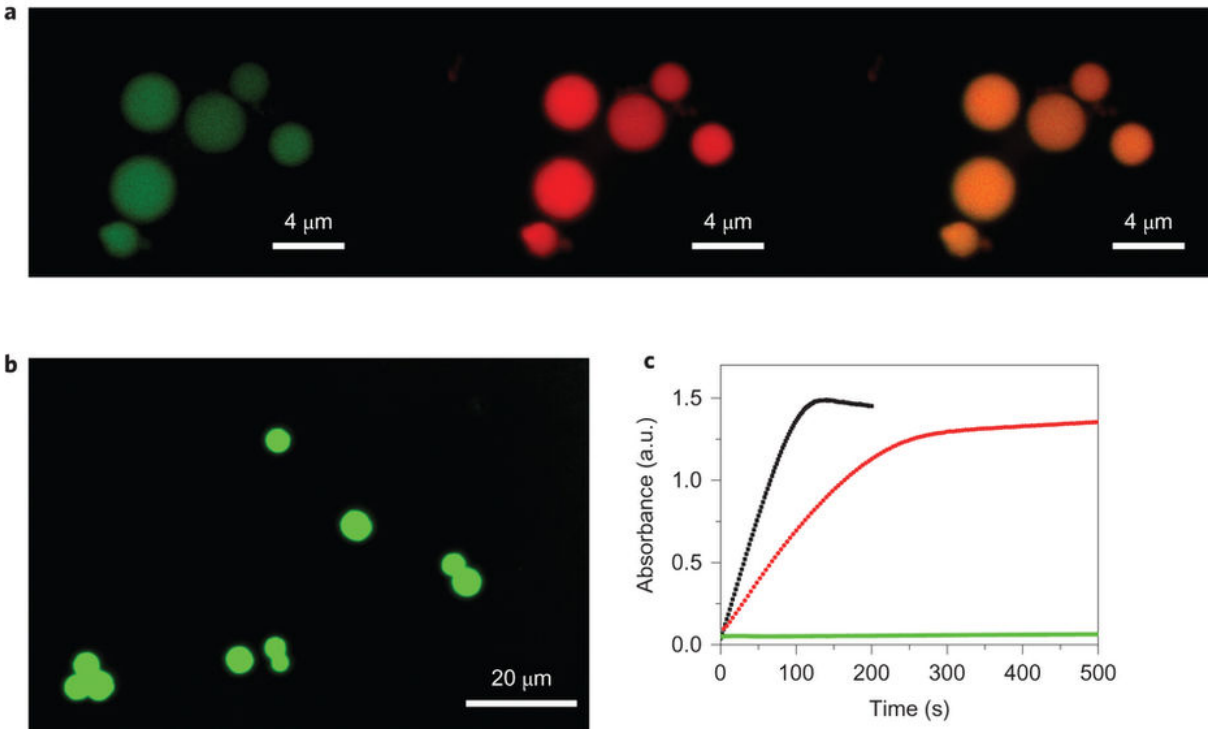

Figure 2-17. Surface-functionalized polymer cubosomes. (a) CLSM images of polymer cubosomes of 1_{217} and NH_2–PEG_{45}–PS_{210}/SH–PEG_{45}–PS_{210} (equimolar mixture, 8% w/w) after selectively labelling SH groups with F-MI (λ_{ex} = 492 nm, λ_{em} = 518 nm, left (ex, excitation; em, emission)) and NH_2 groups with Rho-NHS (λ_{ex} = 564 nm, λ_{em} = 589 nm, center). The merged image confirmed the presence of both functional groups in the same polymer cubosome (right). (b) CLSM image of fluorescein-labelled streptavidin within the biotin-labelled polymer cubosomes of 1_{217}/ NH_2–PEG_{45}–PS_{210} (10% w/w). (c) Time course plots of the absorption of radical cation of $ABTS^{\bullet+}$ oxidized by free (black line) and HRP–cubosomes (red line) of 1_{217}/SH–PEG_{45}–PS_{210} (7% w/w). Free HRP or HRP–cubosome was mixed with a solution containing 1.6 mM ABTS and 0.125 mM H_2O_2 in phosphate buffer (pH 7.4). The absorbance was measured at 740 nm. The green trace indicates the background absorption of ABTS and H_2O_2 in the absence of HRP.

Once the presence of functional groups on the bicontinuous internal structure of the polymer cubosomes was established, we compartmentalized a protein guest, fluorescein-labelled streptavidin homotetramer, within the water channels of the polymer cubosomes of 1_{217}/NH_2–PEG_{45}–PS_{210} (10% w/w). The polymer cubosomes were first reacted with NHS–PEG_4–biotin to afford the surface-bound biotin acting as anchoring points of streptavidin via a strong non-covalent interaction between them. Fluorescein-labelled streptavidin homotetramer was internalized through the surface pores (average diameter >10 nm (Figure 2-16b)) by mixing the protein solution with a suspension of the biotin-labelled polymer cubosomes (Figure 2-17b). After purification, no retention of streptavidin was observed within the polymer cubosomes of 1_{217}/NH_2–PEG_{45}– PS_{210} without surface-bound biotin.

We also demonstrated that the polymer cubosomes could be a platform for biochemical reactors by internalizing the enzyme maleimide-activated horseradish peroxidase (HRP, 44.1 kDa) in the SH-functionalized polymer cubosomes (1_{217}/SH–PEG_{45}–PS_{210}, 7% w/w). The amount of surface-bound HRPs on the polymer cubosomes was quantified by inductively coupled plasma mass spectrometry (ICP-MS), which showed a value of 0.76 μmol g^{-1} and indicated that about 70% of the surface SH groups were functionalized. The presence of surface-bound HRP was confirmed by colorimetric assay conducted by the enzymatic oxidation of ABTS (2,2′-azinobis(3-ethylbenzothiazoline-6-sulfonic acid) diammonium salt) in the presence of H_2O_2 as an oxidant. From the kinetic analysis of the oxidation of ABTS, the apparent Michaelis constant (K_M = 0.29 mM) and maximum reaction rate (V_{max} = 0.005 μM s^{-1}) were determined, which were reduced values in comparison to the measured values of free HRP solution at the same concentration (Figure 2-17c and Table 2-1). However, these catalytic constants were substantially higher than those reported in the literature for HRP physically adsorbed within the internal pores (7.6 nm diameter) of mesoporous silica particles (SBA-15).[42] The fast kinetics of HRP bound at the end of the long PEG chain protruding from the internal surface of the polymer cubosomes suggests a low diffusion barrier in the polymer cubosomes promoted by the cubic networks of large water channels open to the environment.

Table 2-1. Comparison of apparent catalytic constants of free HRP and HRP-cubosome at room temperature (Obtained from the Lineweaver-Burk plots)

	K_M (M)	V_{max} (M/s)	K_M/V_{max} (s)
Free HRP	4.0×10^{-4}	200×10^{-10}	20×10^{3}
HRP-Cubosome	2.9×10^{-4}	50×10^{-10}	58×10^{3}

$$\frac{1}{v} = \frac{1}{V_{max}} + \frac{K_M}{V_{max}}\frac{1}{[S_0]}$$

The Michaelis-Menten equation was applied and the kinetic parameters were interpreted using a Lineweaver-Burk plot, where v, $Vmax$, K_M, and $[S_0]$ are the initial rate of enzyme catalyzed conversion, the maximum reaction rate, Michaelis constant, the initial substrate concentration, respectively.

2.4 Summary

In summary, we have shown that amphiphilic block copolymers built from a hydrophilic dendritic block directly self-assembled into colloidal particles of inverse bicontinuous membranes (polymer cubosomes) in aqueous solution. These polymer cubosomes exhibited highly defined crystalline internal structures of inverse bicontinuous cubic phases. Depending on the architecture of the dendritic scaffold in the hydrophilic block, we observed three bicontinuous cubic structures (double-diamond, gyroid, and primitive cubic phases) analogous to the inverse bicontinuous phases observed from lipid assemblies. These polymer cubosomes were found to be mesoporous, as characterized by N_2-adsorption experiments. By coassembly with α-NH_2- or SH-functionalized linear block copolymers, our block copolymers formed highly defined mesoporous colloidal polymer structures with surface functional groups that can anchor external guests, such as proteins and enzyme.

These results demonstrate that the polymer cubosomes, mesoporous polymeric materials with unprecedented internal structural orders and tunable surface functionalities, may offer new platforms for bioreactors, storage vehicles, sensors and nanotemplates. Polymer cubosomes, which are directly formed from the simple solution self-assembly of block copolymers into inverse cubic mesophases, can be distinguished from most inorganic and polymeric porous materials, which are synthesized using sacrificial templates as pore generators. The architectures of block copolymers based on the dendritic hydrophilic block play a crucial role in the preferential formation of inverse cubic mesophases in solution; this resembles the formation of complex bilayers exhibited by lipids. Our report may open new avenues to investigate and utilize the interesting properties of inverse mesophases of block copolymers, which have not been widely available from the conventional solution self-assembly of block copolymers.

2.5 Experimental

Reagents and equipment. All reagents and chemicals were purchased from commercial sources and used as received. THF was distilled over Na/benzophenone before use. Methylene chloride was distilled over CaH_2. All reactions were performed under N_2 unless otherwise noted. NMR (nuclear magnetic resonance) spectra were recorded on a Varian VNMRS 600 spectrometer with $CDCl_3$ as a solvent. Molecular weights of block copolymers were measured on an Agilent 1260 Infinity GPC system equipped with a PL gel 5 μm mixed D column (Polymer Laboratories) and differential refractive index detectors. THF was used as an eluent with a flow rate of 1 mL min^{-1}. A PS standard (Polymer Laboratories) was used for calibration. MALDI-TOF was performed on a Bruker Ultraflex III TOF-TOF mass spectrometer equipped with a nitrogen laser (335 nm) and operating in a reflectance mode. Internal calibration was performed using a Bruker peptide calibration standard (mass range 1000-4000 Da). The analytical sample was obtained by mixing a THF solution of analyte (5-10 mg mL^{-1}) with a THF solution of matrix (sinapinic acid, 10 mg mL^{-1}) in a 1/5 v/v ratio. The

prepared solution of the analyte and matrix (0.5 μL) was loaded on the MALDI plate and allowed to dry at 23 °C before the plated was inserted into the vacuum chamber of the MALDI instrument. The laser steps and voltages applied were adjusted depending on both the molecular weight and the nature of analyte. Transmission electron microscopy (TEM) was performed on a JEOL JEM-2100 microscope at an acceleration voltage of 200 kV. Sample specimens were prepared by placing a drop of the solution on a carbon-coated Cu grid (200 mesh, EM science). After 30 min, remaining solution on a grid was removed with a filter paper, and the grid was air-dried for 18 h. Scanning electron microscopy (SEM) images were obtained on a FEI Nova NanoSEM 230 microscope and Hitachi S-4800 FE SEM at an acceleration voltage of 10 kV. The sample was placed on a conductive carbon layer and coated with Pt with a thickness of 3 nm by using a K575X Sputter Coater. Confocal laser scanning fluorescence microscopy (CLSM) was performed on a FluoView 1000 Confocal Microscope (Olympus). Dynamic light scattering (DLS) experiments were carried out on a BI-200SM equipped with a diode laser (637 nm, 4 mW). All DLS data were handled on a Dispersion Technology Software (Brookhaven Instruments). The surface pressure/area isotherms were performed using a film balance (KSV NIMA) with a platinum Wilhelmy plate. The subphase was prepared from house-purified water which was subsequently passed through a Milli-Q water purification system equipped with an organic removal cartridge. The subphase water temperature was maintained at 25 (± 0.5) °C. In a typical experiment 20 μL of the polymer solution (1 mg mL^{-1}) was spread evenly over the water surface in small drops. After a further 30 min delay to allow for the evaporation of the solvent, compression at a constant rate of 10 mm/min (12.5 mm^2 s^{-1}) began. The Porous structures of the samples were analyzed by a nitrogen adsorption experiment at − 196 °C using a BEL BELSORP-Max system. The surface areas and pore size distributions of the samples were calculated by using the Brunauer-Emmett-Teller (BET) equation and the Barrett-Joyner-Halenda (BJH) method, respectively. Small angle X-ray scattering data were obtained on the SAXS beamline (PLS-II 9A) at Pohang acceleration laboratory (Pohang, Korea).

Synthesis of Dendrons and Block Copolymers. Dendrons 1 and 2 and their macroinitiators were synthesized in multi-gram quantity by following the literature methods.[37]

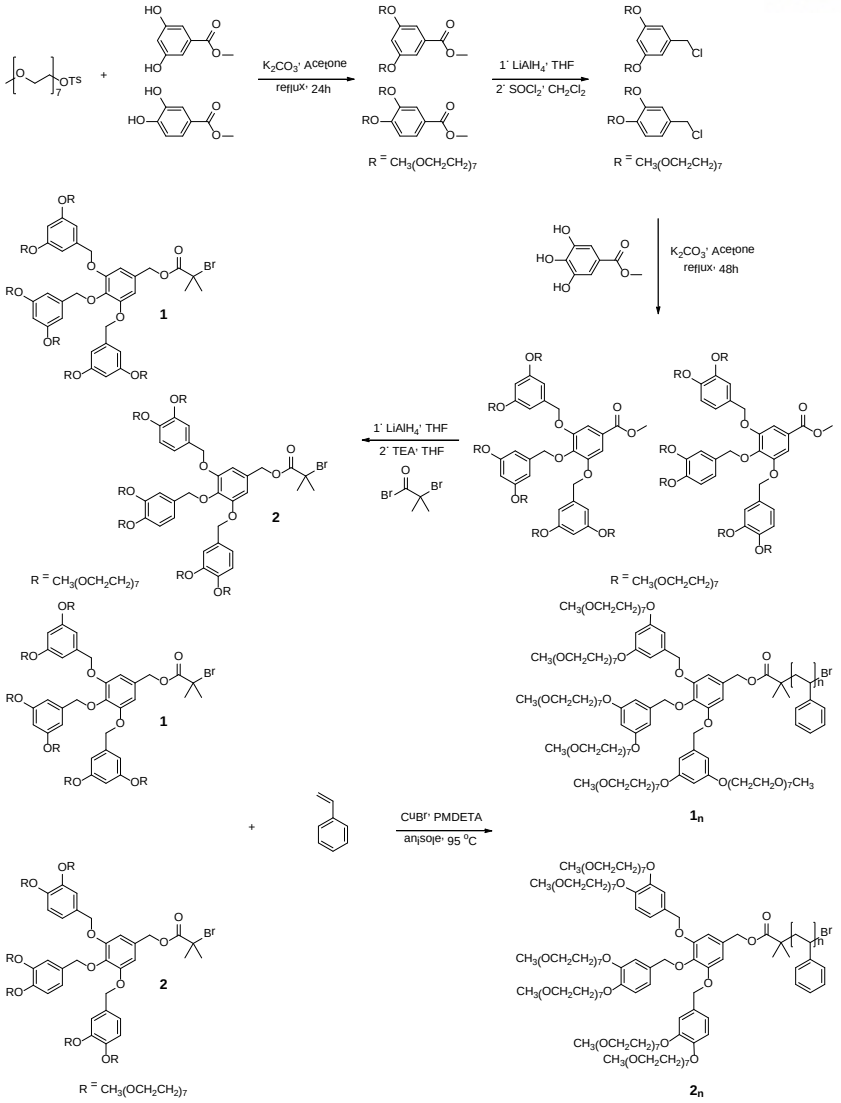

Scheme 2-1. Synthesis of dendritic macroinitiators (**1** and **2**) and dendritic-linear block copolymers (**1**$_n$ and **2**$_n$).

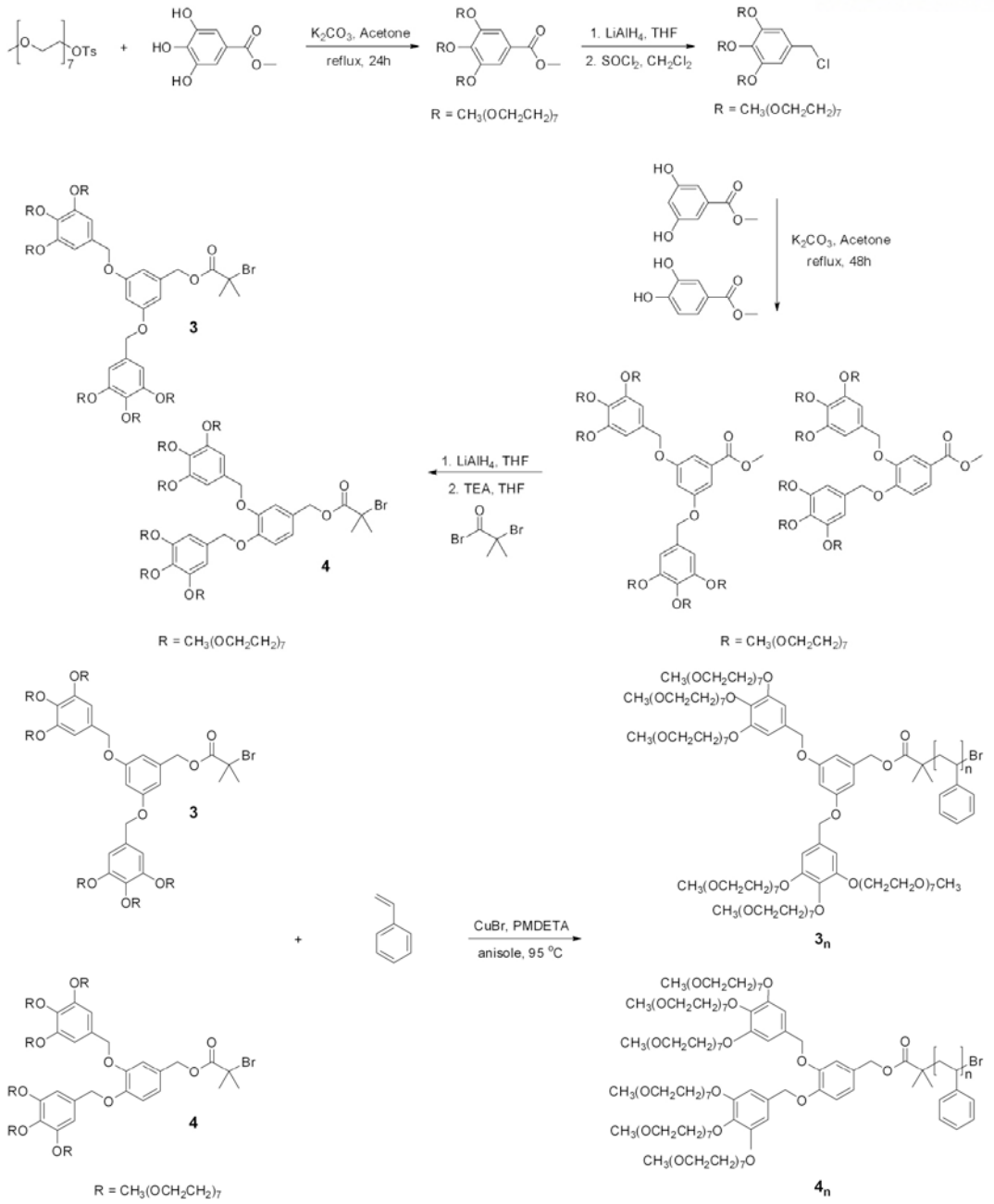

Scheme 2-2. Synthesis of dendritic macroinitiators (**3** and **4**) and dendritic-linear block copolymers (**3**$_n$ and **4**$_n$).

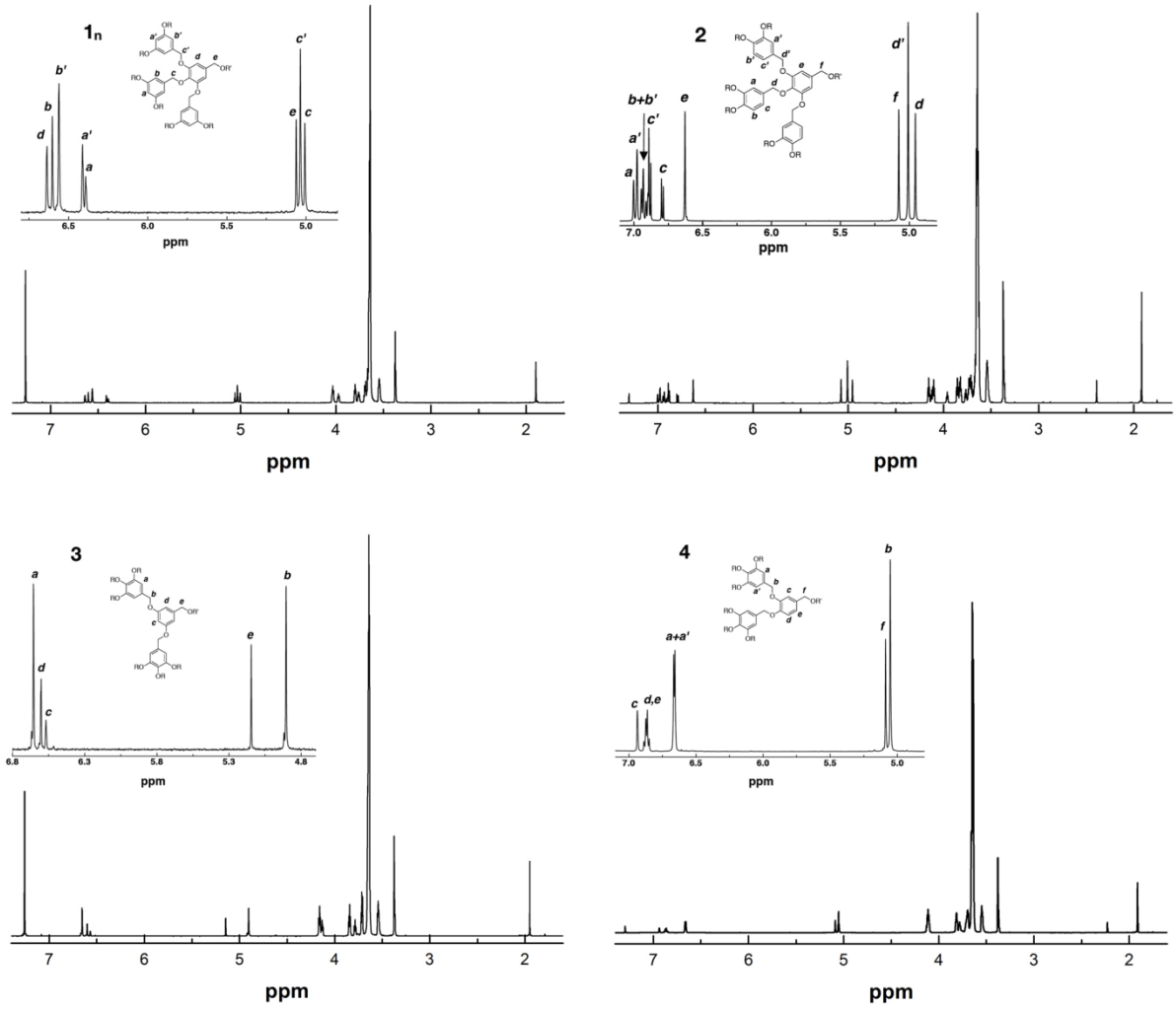

Figure 2-18. ^{1}H NMR spectra of dendritic macroinitiators (R = $CH_3(OCH_2CH_2)_7$)

1. ^{1}H NMR (δ=ppm, 600 MHz, $CDCl_3$) 6.63 (s, 2H), 6.60 (s, 2H), 6.56(s, 4H), 6.41(s, 2H), 6.39(s, 1H) 5.06 (s, 2H), 5.03 (s, 4H), 5.00 (s, 2H), 4.03 (t, 8H, *J* = 4.8Hz), 3.97(t, 4H, *J* = 4.8Hz), 3.81-3.50 (m, -CH_2CH_2O-), 3.37 (m, 18H), 1.90 (s, 6H). ^{13}C NMR (δ=ppm, 150 MHz, $CDCl_3$) 171.2, 160.0, 159.7, 152.7, 140.1, 139.4, 138.0, 131.1, 107.4, 106.2, 105.4, 101.4, 101.0, 74.8, 71.8, 71.1, 70.9-70.1, 69.6, 69.6, 67.4, 67.3, 67.2, 59.0, 55.8, 30.7. M_n (GPC) = 3278 g mol^{-1}, $Đ$ = 1.03, M_n (MALDI-TOF) = 2930 g mol^{-1}.

2. ^{1}H NMR (δ=ppm, 600 MHz, $CDCl_3$) 7.00 (s, 1H), 6.97 (s, 2H), 6.93 (d, 2H, *J* = 8.4Hz), 6.90 (d, 1H, *J* = 8.2Hz), 6.88 (d, 2H, *J* = 8.2Hz), 6.79 (d, 1H, *J* = 8.1Hz), 6.62(s, 2H), 5.07 (s, 2H), 5.00 (s, 4H), 4.15 (t, 4H, *J* = 5.1Hz), 4.11 (dt, 6H, *J* = 9.8, 5.1Hz), 3.96 (t, 2H, *J* = 4.9Hz), 3.88-3.50 (m, -CH_2CH_2O-), 3.37 (m, 18H), 1.91 (s, 6H). ^{13}C NMR (δ=ppm, 150 MHz, $CDCl_3$) 171.2, 152.8, 148.9, 148.7, 148.6, 148.5, 138.2, 131.2, 130.9, 130.3, 121.5, 120.6, 114.6, 114.5, 114.3, 113.8, 107.7, 74.7, 71.9, 71.1, 70.9-70.1, 69.7, 69.7, 69.6, 68.8, 68.8, 68.5, 67.3, 59.0, 55.9, 30.7. M_n (GPC) = 2842 g mol^{-1}, $Đ$ = 1.03, M_n (MALDI-TOF) = 2727 g mol^{-1}.

3. ^{1}H NMR (δ=ppm, 600 MHz, $CDCl_3$) 6.66 (s, 4H), 6.60 (s, 2H), 6.57 (s, 1H), 5.15 (s, 2H), 4.91 (s, 4H), 4.16 (t, 8H, *J* = 4.8Hz), 4.13 (t, 4H, *J* = 4.8Hz), 3.87-3.50 (m, -CH_2CH_2O-), 3.38 (m, 18H), 1.95 (s, 6H). ^{13}C NMR (δ=ppm, 150 MHz, $CDCl_3$) 171.2, 159.9, 152.7, 138.1, 137.7, 132, 107.1, 106.5, 101.8, 77.3, 77.1, 76.9, 71.8, 70.7-70.1, 58.9, 55.8, 30.7. M_n (GPC) = 2558 g mol^{-1}, $Đ$ = 1.03, M_n (MALDI-TOF) = 2623 g mol^{-1}.

4. ^{1}H NMR (δ=ppm, 600 MHz, $CDCl_3$) 6.93 (s, 1H), 6.86 (dd, 2H, *J* = 14.9, 8.4Hz), 6.66 (d, 4H, *J* = 5.6Hz), 5.08 (s, 2H), 5.05 (s, 4H), 4.11 (m, 12H), 3.88-3.50 (m, -CH_2CH_2O-), 3.36(m, 18H), 1.91 (s, 6H). ^{13}C NMR (δ=ppm, 150 MHz, $CDCl_3$) 171.3, 152.7, 148.8, 137.9, 132.7, 132.6, 128.7, 121.5, 114.9, 106.6 77.2, 77, 76.8, 70.7-70.4, 69.7, 69.6, 59.0, 55.9, 30.7. M_n (GPC) = 2464 g mol^{-1}, $Đ$ = 1.05, M_n (MALDI-TOF) = 2571 g mol^{-1}.

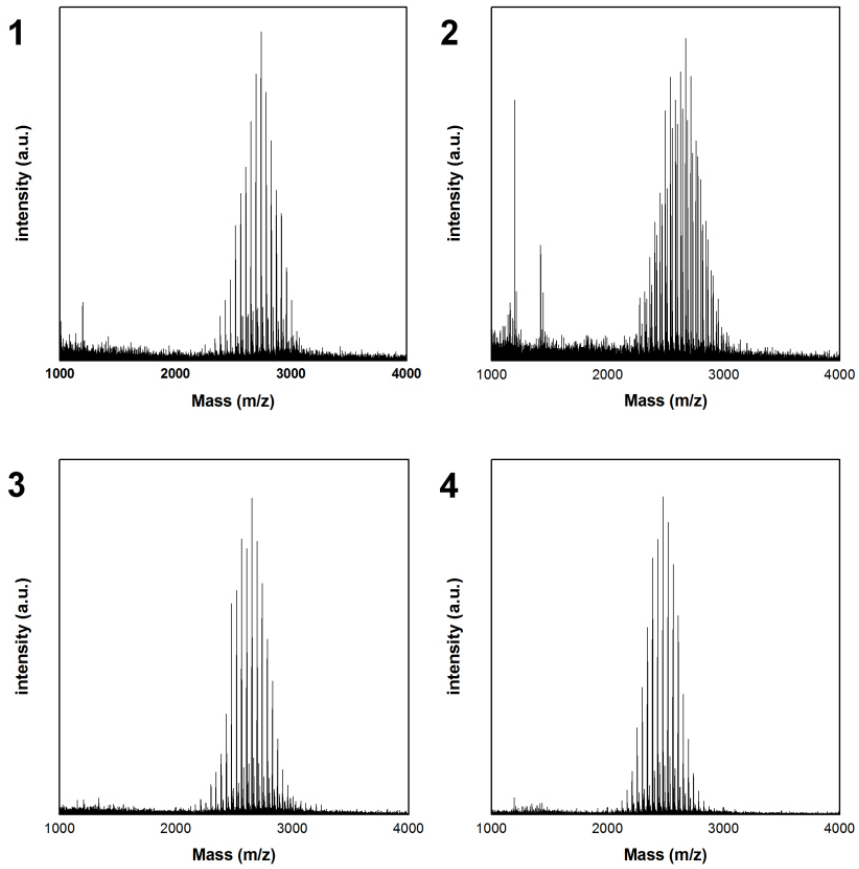

Figure 2-19. MALDI-TOF spectra of macroinitiators **1**,**2**,**3**, and **4**.

Polymerization of styrene was performed with macroinitiators under a standard ATRP condition. Representative procedure: CuBr (7 mg, 0.05 mmol) and *N,N,N′,N″,N″*-pentamethyldiethylenetriamine (PMDETA) (12 mg, 0.075 mmol) were mixed with 1 mL of anisole in a 20 mL Schlenk tube with a magnetic bar. The tube was sealed with a rubber septum. This mixture was bubbled with N_2 for 15 min with gentle stirring. To this solution, the solution of styrene (5 mL) and **1** (120 mg, 0.035 mmol) was added via a syringe. The green solution was degassed by bubbling N_2 for 20 min. After degassing, the tube was immersed in a preheated oil bath (95 °C), and the polymerization proceeded at this temperature. The progress of polymerization was monitored by taking GPC at an interval of 1 h. When the molecular weight of the block copolymer reached to the desired value, the reaction was quenched by exposing the solution to air in an ice/water bath and diluted with $CHCl_3$ (15 mL). The cooled solution was filtered through a pack of aluminum oxide (basic) with $CHCl_3$ to remove the Cu catalyst. The filtered solution was concentrated on a rotavap, and the resulting residue was diluted with 20 mL CH_2Cl_2. This solution was precipitated into methanol (400 mL). The white powder was collected by vacuum filtration and dried in vacuo. All block copolymers were characterized by ^{1}H NMR and GPC to evaluate the molecular weight and the size distribution. The molecular characteristics of the block copolymers are listed in **Table 2-2**.

Table 2-2. Characterization of dendritic-linear block copolymers

sample	M_n (g/mol)[a]	DP_n (PS)[b]	$Đ$[a]	f_{PEG}[c]	Phase[d]
$\mathbf{1}_{185}$	19190	185	1.09	10.9	v,l
$\mathbf{1}_{217}$	21380	217	1.07	9.3	c
$\mathbf{1}_{232}$	24460	232	1.06	8.9	lc,h
$\mathbf{2}_{180}$	19240	180	1.11	11.4	v,l
$\mathbf{2}_{213}$	21320	213	1.08	9.4	c
$\mathbf{2}_{245}$	24130	245	1.12	8.4	lc,h
$\mathbf{3}_{223}$	23790	223	1.06	9.1	c
$\mathbf{3}_{242}$	24970	242	1.06	8.4	lc,h
$\mathbf{4}_{222}$	23480	222	1.06	9.1	c
$\mathbf{4}_{254}$	24930	254	1.08	8.0	lc,h

[a] The number average molecular weight and molecular weight distribution determined by GPC (THF, 35 °C, 1 mL min^{-1} flow rate) using PS standards. [b] The number average degree of polymerization of PS block determined by ^{1}H NMR integration. [c] The molecular weight ratio of the PEG domain to that of the PS block (M_n(PEG) = 2150 g/mol). [d] Observed morphology of self-assembled structures of the suspension solution prepared from dioxane solution of the block copolymer (0.5 wt%). v: vesicle, l: lamella, c: cubosomes, lc: large cubosomes, h: hexasomes

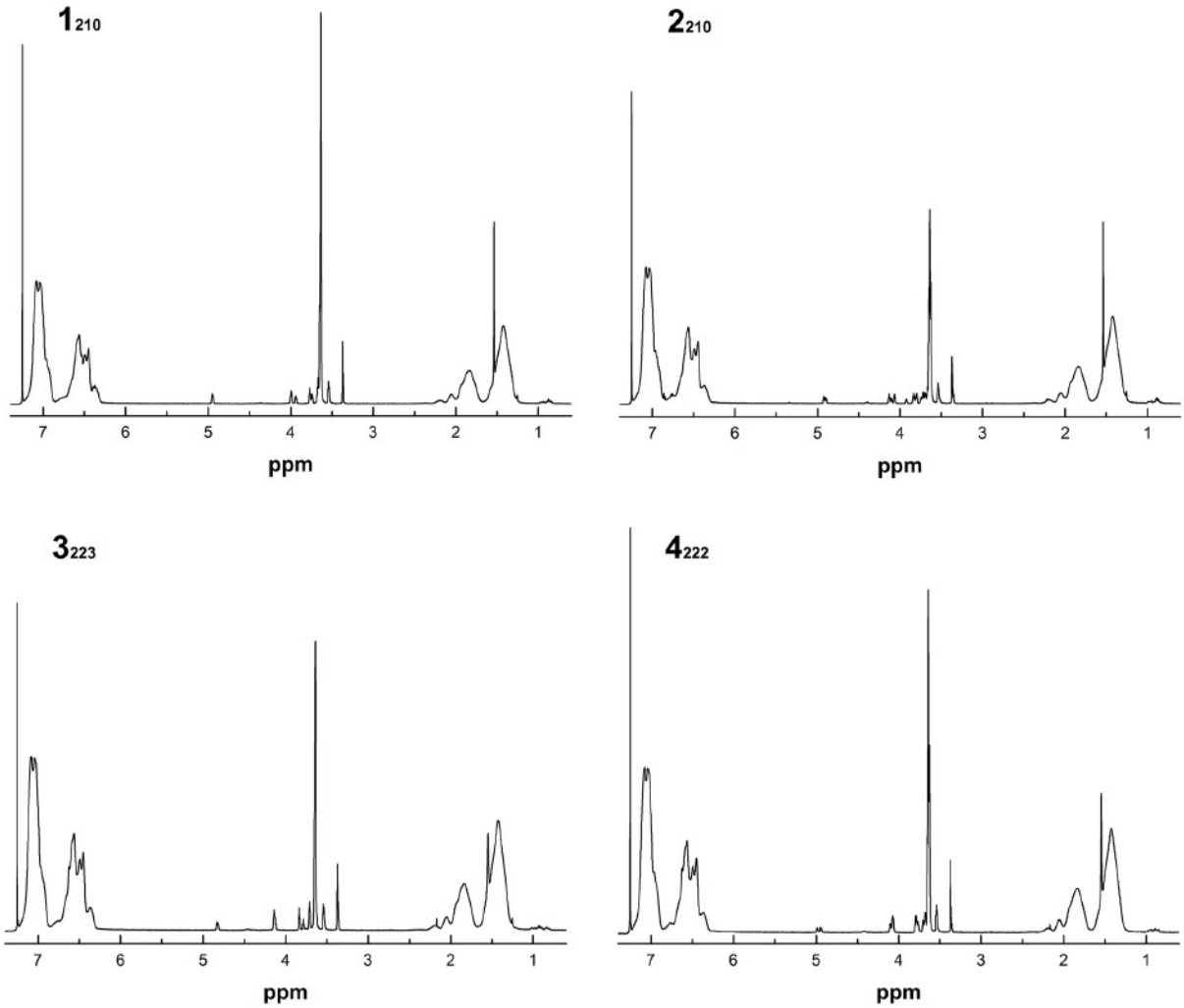

Figure 2-20. ^{1}H NMR spectra of dendritic-linear block copolymers.

Preparation of NH_2-PEG_{45}-PS_{210} and SH-PEG_{45}-PS_{210}. 2,4-Dinitrophenylthioacetic acid and α-alkyne-ω-bromide polystyrene (M_n = 21,000 g mol^{-1}) were respectively synthesized according to literature procedures.[43,44] α, ω-Azido PEG (M_n = 2,000 g mol^{-1}) was subjected to azide–alkyne Huisgen cycloaddition with α-alkyne-ω-bromide polystyrene (M_n = 21,000 g mol^{-1}) in the presence of CuBr and PMDETA. The resulting N_3-PEG_{45}-PS_{210} was transformed to NH_2-PEG_{45}-PS_{210} (M_n = 23,000 g mol^{-1}) under Staudinger reaction condition. α-Hydroxyl-ω-azido PEG (M_n = 2,000 g mol^{-1}) was conjugated with 2,4-dinitrophenylthioacetic acid by Steglich esterification. After 20 h the solution was precipitated into cold diethyl ether. The polymer was filtered and dried to yield an off-white solid. The resulting polymer was coupled with α-alkyne-ω-bromide polystyrene (M_n = 21,000 g mol^{-1}) in the presence of CuBr and PMDETA. To obtain SH-PEG_{45}-PS_{210} (M_n = 23,000 g mol^{-1}), the protecting group of thiol was removed through an exchange reaction of the protected chain-end with a large excess of ethanethiol in the presence of triethylamine. The presence of α-functional group was confirmed by GPC with a UV detector, which showed a presence of labeled dyes on the position of

block copolymers in the chromatograms. All block copolymers were characterized by ^{1}H NMR and GPC to evaluate the molecular weight and the size distribution. NH_2-PEG_{45}-PS_{210} DP_n (PS) = 220 (^{1}H NMR). M_n = 23,971 g mol^{-1}, $Đ$ = 1.12 (GPC). SH-PEG_{45}-PS_{210} DP_n (PS) = 201 (^{1}H NMR). M_n = 23,793 g mol^{-1}, $Đ$ = 1.09 (GPC).

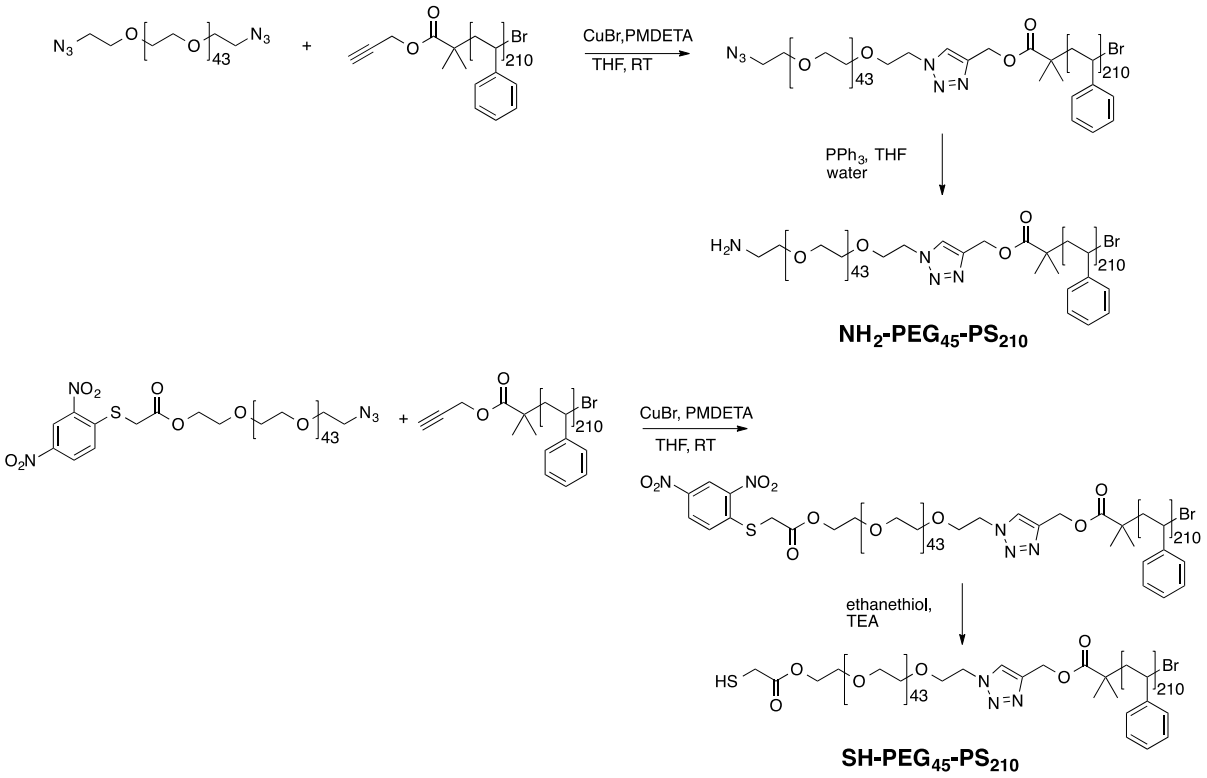

Scheme 2-3. Synthesis of α-functionalized PEG-PS block copolymers.

Self-assembly of dendritic–linear block copolymers into polymer cubosomes. In a typical procedure, 1_{217} (20 mg) was dissolved in 1,4-dioxane (2 mL) in a 15 mL capped vial with a magnetic stirrer. The solution was stirred for three hours at room temperature. A syringe pump was calibrated to deliver water at a speed of 1 mL h^{-1}. The vial cap was replaced by a rubber septum. Water (2 mL, MilliQ, 18.1 MΩ) was added to the organic solution with vigorous stirring (850 revolutions per minute) by a syringe pump with a 5 mL syringe equipped with a steel needle. The resulting suspension solution was subjected to dialysis (molecular weight cutoff (MWCO) ~12-14 kDa (SpectraPor)) against water for 24 hours with frequent changes of water. The procedure could be scaled up to 100 mg with a proportionally increased amount of solvents and rate of water addition. For coassembly with α-functionalized linear block copolymers, the block copolymer mixture was prepared by mixing dioxane solutions of a linear-dendritic block copolymer (10 mg mL^{-1}) and the α-functionalized linear block copolymer (2 mg mL^{-1}) in an appropriate ratio (2 mL). This mixture was stirred for three hours at room temperature. Water was added to it via a syringe pump, as described above, followed by dialysis against water. Polymer cubosomes settled down in water during storage

under gravity and could be redispersed on shaking the aqueous solution.

Covalent labelling of surface functional groups of polymer cubosomes. An equimolar mixture of Rho-NHS and F-MI was dissolved in PBS (pH 7.4). This solution was mixed with the polymer cubosomes of 1_{217}/(NH_2-PEG_{45}-PS_{210}/SH-PEG_{45}-PS_{210}) (an equimolar mixture of linear block copolymers, 8% w/w) dispersed in PBS. The mixture was aged for 16 hours at room temperature. The excess fluorescent dyes were removed from the suspension by repeated centrifugation on a centrifugal filter (MWCO = 100 kDa (Amicon)) and dilution with buffer and methanol until the aliquot did not show any fluorescence. The polymer cubosomes of 1_{217} without surface functional groups did not show any retention of dyes on fluorescence microscopy after the same procedure of purification. The labelled polymer cubosomes were visualized on a confocal laser scanning microscope (FluoView 1000, Olympus).

Biotinylation of polymer cubosomes and streptavidin compartmentalization. The polymer cubosomes of 1_{217}/NH_2-PEG_{45}-PS_{210} (10% w/w) were prepared by the method described above. The NH_2-functionalized polymer cubosomes were reacted with NHS-PEG_4-biotin (Thermo Scientific) in PBS (pH 7.4) for 24 hours at room temperature. The excess reagent was removed from the suspension by repeated centrifugation and dilution with PBS and methanol. This biotin–polymer cubosomes were mixed with a PBS solution of fluorescein-labelled streptavidin homotetramer (Sigma) for 24 hours at 4 °C. The unbound streptavidin was removed by centrifugation on a centrifugal filter (MWCO = 100 kDa (Amicon)). The centrifugation was repeated until the filtered portion showed no fluorescence.

Conjugation of HRP to polymer cubosomes. A PBS solution of the cubosome of 1_{217}/SH-PEG_{45}-PS_{210} (7% w/w, 1 mg mL^{-1}, pH 7.4) was added to HRP-maleimide (1 mg, 44.1 kDa) in a vial. The mixture was stirred for three days. The solution was then centrifuged and washed several times with PBS solution until no free HRP could be detected in the supernatant. As detected by ICP-MS, about 70% of all available thiol sites were occupied by HRP-maleimide. To measure the enzymatic activity, equivalent amounts of HRP from free HRP or HRP-cubosome were mixed with a PBS solution (pH 7.4) of 1.67 mM ABTS in a quartz cell, and 0.125 mM hydrogen peroxide was added to initiate the oxidative reaction. Time-course absorption changes of $ABTS^{\bullet+}$ at 740 nm were collected on a JASCO V-670 spectrophotometer. The Michaelis–Menten equation was applied, and the kinetic parameters were interpreted using a Lineweaver–Burk plot.

2.6 References

1. Israelachivili, J. N. Intermolecular and Surface Forces (Academic Press, 1992).
2. Zhang, L.; Eisenberg, A. Multiple Morphologies of "Crew-Cut" Aggregates of Polystyrene-*b*-Poly(acrylic acid) block copolymers. *Science* **1995**, *268*, 1731.
3. Zhang, L.; Bartels, C.; Yu, Y.; Shen, H.; Eisenberg, A. Mesosized Crystal-like Structure of Hexagonally Packed Hollow Hoops by Solution Self-Assembly of Diblock Copolymers. *Phys. Rev. Lett.* **1997**, *79*, 5034–5037.
4. Yu, K.; Bartels, C.; Eisenberg, A. Trapping of Intermediate Structures of the Morphological Transition of Vesicles to Inverted Hexagonally Packed Rods in Dilute Solutions of PS-*b*-PEO. *Langmuir* **1999**, *15*, 7157–7167.
5. Mai, Y.; Eisenberg, A. Self-Assembly of Block Copolymers. *Chem. Soc. Rev.* **2012**, *41*, 5969–5985.
6. Schacher, F. H.; Rupar, P. A.; Manners, I. Functional Block Copolymers: Nanostructured Materials with Emerging Applications. *Angew. Chem. Int. Ed.* **2012**, *51*, 7898–7921.
7. Moffit, M.; Khougaz, K.; Eisenberg, A. Micellization of Ionic Block Copolymers. *Acc. Chem. Res.* **1996**, *29*, 95–102.
8. Hales, K.; Chen, Z.; Wooley, K. L.; Pochan, D. J. Nanoparticles with Tunable Internal Structure from Triblock Copolymers of PAA-*b*-PMA-*b*-PS. *Nano Lett.* **2008**, *8*, 2023–2026.
9. Cui, H.; Chen, Z.; Zhong, S.; Wooley, K. L.; Pochan, D. J. Block Copolymer Assembly via Kinetic Control. *Science* **2007**, *317*, 647–650.
10. Li, Z.; Kesselman, E.; Talmon, Y.; Hillmyer, M. A.; Lodge, T. P. Multicompartment Micelles from ABC Miktoarm Stars in Water. *Science* **2004**, *306*, 98–101.
11. Christian, D. A. et al. Spotted Vesicles, Striped Micelles and Janus Assemblies Induced by Ligand Binding. *Nat. Mater.* **2009**, *8*, 843–849.
12. Wang, X. et al. Cylindrical Block Copolymer Micelles and Co-Micelles of Controlled Length and Architecture. *Science* **2007**, *317*, 644–647.
13. Jackson, E. A.; Hillmyer, M. A. Nanoporous Membranes Derived from Block Copolymers: from Drug Delivery to Water Filtration. *ACS Nano* **2010**, *4*, 3548–3553.
14. Seo, M.; Hillmyer, M. A. Reticulated Nanoporous Polymers by Controlled Polymerization-Induced Microphase Separation. *Science* **2012**, *336*, 1422–1425.
15. Peinemann, K-V.; Abetz, V.; Simon, P. F. W. Asymmetric Superstructure Formed in a Block Copolymer via Phase Separation. *Nature Mater.* **2007**, *6*, 992–996.
16. Larsson, K. Cubic Lipid–Water Phases: Structures and Biomembrane Aspects. *J. Phys. Chem.* **1989**, *93*, 7304–7314.
17. Kulkarni, C. V.; Wachter, W.; Iglesias-Salto, G.; Engelskirchen, S.; Ahualli, S. Monoolein: a Magic Lipid? *Phys. Chem. Chem. Phys.* **2011**, *13*, 3004–3021.

18. Almsherqi, Z. A., Kohlwein, S. D.; Deng, Y. Cubic Membranes: a Legend Beyond the Flatland of Cell Membrane Organization. *J. Cell Biol.* **2006**, *173*, 839–844.
19. Lindstroöm, M., Ljusberg-Wahren, H.; Larsson, K. Aqueous Lipid Phases of Relevance to Intestinal Fat Digestion and Absorption. *Lipids* **1981**, *16*, 749–754.
20. van Meer, G., Voelker, D. R.; Freigenson, G. W. Membrane Lipids: Where They Are and How They Behave. *Nature Rev. Mol. Cell Biol.* **2008**, *9*, 112–124.
21. Gustafsson, J., Ljusberg-Wahren, H., Almgren, M.; Larsson, K. Cubic Lipid–Water Phase Dispersed into Submicron Particles. *Langmuir* **1996**, *12*, 4611–4613.
22. Spicer, P. T. in Dekker Encyclopedia of Nanoscience and Nanotechnology (eds Schwarz, J. A.; Contescu, C.; Putyera, K.) 881–892 (Marcel Dekker, 2004).
23. Landau, E. M.; Rosenbusch, J. P. Lipidic Cubic Phases: a Novel Concept for the Crystallization of Membrane Proteins. *Proc. Natl Acad. Sci. U. S. A.* **1996**, *93*, 14532–14535.
24. Caffrey, M. Crystallizing Membrane Proteins for Structure Determination: Use of Lipidic Mesophases. *Annu. Rev. Biophys.* **2009**, *38*, 29–51.
25. Angelova, A.; Angelov, B.; Papahadjopoulos-Sternberg, B.; Ollivon, M.; Bourgaux, C. Proteocubosomes: Nanoporous Vehicles with Tertiary Organized Fluid Interfaces. *Langmuir* **2005**, *21*, 4138–4143.
26. Spicer, P. T. Progress in Liquid Crystalline Dispersions: Cubosomes. *Curr. Opin. Colloid Interface Sci.* **2005**, *10*, 274–279.
27. Battaglia, G.; Ryan, A. J. Effect of Amphiphile Size on the Transformation from a Lyotropic Gel to a Vesicular Dispersion. *Macromolecules* **2006**, *39*, 798–805.
28. Battaglia, G.; Ryan, A. J. The Evolution of Vesicles from Bulk Lamellar Gels. *Nature Mater.* **2005**, *4*, 869–876.
29. Jain, S.; Gong, X.; Scriven, L. E.; Bates, F. S. Disordered Network State in Hydrated Block-Copolymer Surfactants. *Phys. Rev. Lett.* **2006**, *96*, 138304.
30. Alexandridis, P.; Olsson, U.; Lindman, B. Structural Polymorphism of Amphiphilic Copolymers: Six Lyotropic Liquid Crystalline and Two Solution Phases in a Poly(oxybutylene)-*b*-Poly(oxyethylene)–Water–Xylene System. *Langmuir* **1997**, *13*, 23–34.
31. Percec, V. et al. Self-assembly of Janus Dendrimers into Uniform Dendrimersomes and Other Complex Architectures. *Science* **2010**, *328*, 1009–1014.
32. McKenzie, B. E.; Nudelman, F.; Bomans, P. H. H.; Holder, S. J.; Sommerdijk, N. A. J. M. Temperature-Responsive Nanospheres with Bicontinuous Internal Structures from a Semicrystalline Amphiphilic Block Copolymer. *J. Am. Chem. Soc.* **2010**, *132*, 10256–10259.
33. Parry, A. L.; Bomans, P. H. H.; Holder, S. J.; Sommerdijk, N. A. J. M.; Biagini, S. C. G. Cryo Electron Tomography Reveals Confined Complex Morphologies of Tripeptide-Containing Amphiphilic Double-Comb Diblock Copolymers. *Angew. Chem. Int. Ed.* **2008**, 47, 8859–8862.

34. Dehsorkhi, A.; Castelletto, V.; Hamley, I.W. & Harris, P. J. F. Multiple Hydrogen Bonds Induce Formation of Nanoparticles with Internal Microemulsion Structure by an Amphiphilic Copolymer. *Soft Matter* **2011**, *7*, 10116–10121.
35. Denkova, A. G.; Bomans, P. H. H.; Coppens, M-O.; Sommerdijk, N. A. J. M.; Mendes, E. Complex Morphologies of Self-Assembled Block Copolymer Micelles in Binary Solvent Mixtures: the Role of Solvent–Solvent Correlations. *Soft Matter* **2011**, *7*, 6622–6628.
36. McKenzie, B. E.; Holder, S. J.; Sommerdijk, N. A. J. M. Assessing Internal Structure of Polymer Assemblies from 2D to 3D CryoTEM: Bicontinuous Micelles. *Curr. Opin. Colloid Interface Sci.* **2012**, *17*, 343–349.
37. Jeong, M. G.; van Hest, J. C. M.; Kim, K. T. Self-Assembly of Dendritic–Linear Block Copolymers with Fixed Molecular Weight and Block Ratio. *Chem. Commun.* **2012**, *48*, 3590–3592.
38. Kim, K. T. et al. Polymersome Stomatocytes: Controlled Shape Transformation of Polymer Vesicles. *J. Am. Chem. Soc.* **2010**, *132*, 12522–12524.
39. Almgren, M.; Edwards, K.; Karlsson, G. Cryo Transmission Electron Microscopy of Liposomes and Related Structures. *Colloids Surf. A* **2000**, *174*, 3–21.
40. Kulkarni, C. V. et al. Engineering Bicontinuous Cubic Structures at the Nanoscale–the Role of Chain Splay. *Soft Matter* **2010**, *6*, 3191–3194.
41. Georgieva, J. V. et al. Peptide-Mediated Blood–Brain Barrier Transport of Polymersomes. *Angew. Chem. Int. Ed.* **2012**, *51*, 8339–8342.
42. Ikemoto, H.; Chi, Q.; Ulstrup, J. Stability and Catalytic Kinetics of Horseradish Peroxidase Confined in Nanoporous SBA-15. *J. Phys. Chem. C* **2010**, *114*, 16174–16180.
43. Trollsås, M.; Hawker, C. J.; Hedrick, J. L. A Mild and Versatile Synthesis for the Preparation of Thiol-Functionalized Polymer. *Macromolecules* **1998**, *31*, 5960–5963.
44. Rocha, N.; Mendonca, P. V.; Mendes, J. P.; Simoes, P. N.; Popov, A. V.; Guliashvili, T.; Serra, A. C.; Coelho, J. F. J. Facile Synthesis of Well-Defined Telechelic Alkyne-Terminated Polystyrene in Polar Media using ATRP with Mixed Fe/Cu Transition Metal Catalyst. *Macromol. Chem. Phys.* **2013**, *214*, 76–84.

Chapter 3. Mesoporous monoliths of inverse bicontinuous cubic phases of block copolymer bilayers

3.1 Abstract

Solution self-assembly of block copolymers into inverse bicontinuous cubic mesophases is a promising new approach for creating porous polymer films and monoliths with highly organized bicontinuous mesoporous networks. Here we report the direct self-assembly of block copolymers with branched hydrophilic blocks into large monoliths consisting of the inverse bicontinuous cubic structures of the block copolymer bilayer. We suggest a facile and scalable method of solution self-assembly by diffusion of water to the block copolymer solution, which results in the unperturbed formation of mesoporous monoliths with largepore (>25nm diameter) networks weaved in crystalline lattices. The surface functional groups of the internal large-pore networks are freely accessible for large guest molecules such as protein complexes of which the molecular weight exceeded 100 kDa. The internal double-diamond (*Pn3m*) networks of large pores within the mesoporous monoliths could be replicated to self-supporting three-dimensional skeletal structures of crystalline titania and mesoporous silica.

3.2 Introduction

Porous polymer films and monoliths with internal bicontinuous nanoporous networks are increasingly important materials for applications such as desalination of water, ultrafiltration, chromatography, drug delivery, catalysis and nanotemplating.[1–7] In addition, polymer films and monoliths that have a three-dimensional (3D) crystalline array of internal nanoporous networks can serve as soft templates for creating mesoporous semiconductor crystals for highly efficient optical and optoelectronic materials and multifunctional hybrid materials.[8–12] In spite of recent advances in synthesizing porous polymers with internal bicontinuous porous networks,[13–20] microphase separation of block copolymers (BCPs) in bulk, followed by a selective removal of the labile polymer domains, remains a dominant method to create a cubic crystalline array of bicontinuous nanopores in polymer films and monoliths.[21,22] This method relies on the slow motion of BCPs in bulk, which might impede rapid synthesis of large monoliths with highly organized bicontinuous arrays of pores such as bicontinuous cubic structures.[23] Although solution self-assembly of BCPs has been widely used to create nanostructures with the desired morphology and functions,[24,25] this method generally yielded low-dimensional nanostructures, and, thus, has rarely been adopted as a method for the creation of highly ordered 3D periodic porous polymers.

Peinemann, Abetz, and others[14,26–31] reported the synthesis of 3D porous polymers by non-solvent-induced phase separation of BCPs, which gives an integral asymmetric membrane with a highly

ordered thin layer on top of a non-ordered sponge-like layer. Recently, Wiesner and co-workers[13,17] developed SIM^{2}PLE (spinodal-decomposition-induced macro- and mesophases separation plus extraction by rinsing) method based on the phase separation of BCPs and spinodal decomposition between BCPs and oligomeric additives, rendering the resulting structures to be hierarchically porous polymer monoliths composed of ordered mesopores and randomly distributed macropores. Still, however, direct self-assembly of BCPs in solution into the dense inverse bicontinuous cubic (IBC) structures of the BCP bilayer in the form of films and monoliths has remained a challenge.

Solution self-assembly of BCPs has shown the formation of inverse mesophases, which resulted in the formation of colloidal nano- and microparticles having internal bicontinuous pore networks.[32–37] The direct self-assembly of BCPs into IBC structures consisting of the BCP bilayers is an emerging method to create highly regular bicontinuous porous polymers without any aid of post processes to generate internal pore networks and surface functional groups.[36,37] We recently showed that the dendritic-linear BCPs composed of a dendritic block with peripheral hydrophilic poly(ethylene glycol) (PEG) chains and a glassy polystyrene (PS) hydrophobic block (Figure 3-1a) preferentially self-assemble into inverse bicontinuous mesophases, in which the constituting BCP bilayers form the IBC structure, a 3D-flexed periodic structures of the membrane having zero mean curvature.[32,36] This self-assembly results in the formation of microscaled colloidal particles having internal non-interpenetrating networks of water channels weaved in a cubic crystalline order. The internal structures of the resulting colloidal particles (polymer cubosomes) consist of the IBC structure of the BCP bilayers, and show crystalline lattices over the long range including primitive cubic (P surface), double-diamond (D surface) and gyroid (G surface) symmetries. Peinemann and co-workers[37] also reported the formation of polymer cubosomes having internal P surface by self-assembly of poly(acrylic acid)-*b*-PS in dilute solution, which exhibited high sorption capabilities for proteins. This new synthetic strategy based on direct self-assembly of BCPs in solution could be greatly beneficial to the creation of porous polymers with 3D-ordered porous networks. However, the solution self-assembly of BCPs has rendered the resulting porous polymers to be colloidal particles rather than films and monoliths.

We report here the direct solution self-assembly of amphiphilic dendritic-linear BCPs into mesoporous monoliths entirely composed of triply periodic IBC structures of the BCP bilayer. Utilizing the preferential self-assembly of dendritic-linear BCPs into inverse mesophases in solution,[36] we devise a simple and scalable method for the preparation of large mesoporous monoliths by self-assembly of the BCPs into the IBC structures, which is driven by the diffusion of a poor solvent (water) into the BCP solution under controlled humidity. This method allows the unperturbed growth of the porous monolith with an internal 3D cubic crystalline array of networks of large water channels (>25 nm) of a double-diamond lattice (*Pn3m*) with the desired surface functional groups. The internal network of the water channels may be used as a platform to accommodate guest molecules such as

protein complexes, and the monolith is also demonstrated as a scaffold for the synthesis of 3D skeletal nanostructures of inorganic oxides with hierarchical porous networks.

3.3 Results and discussion

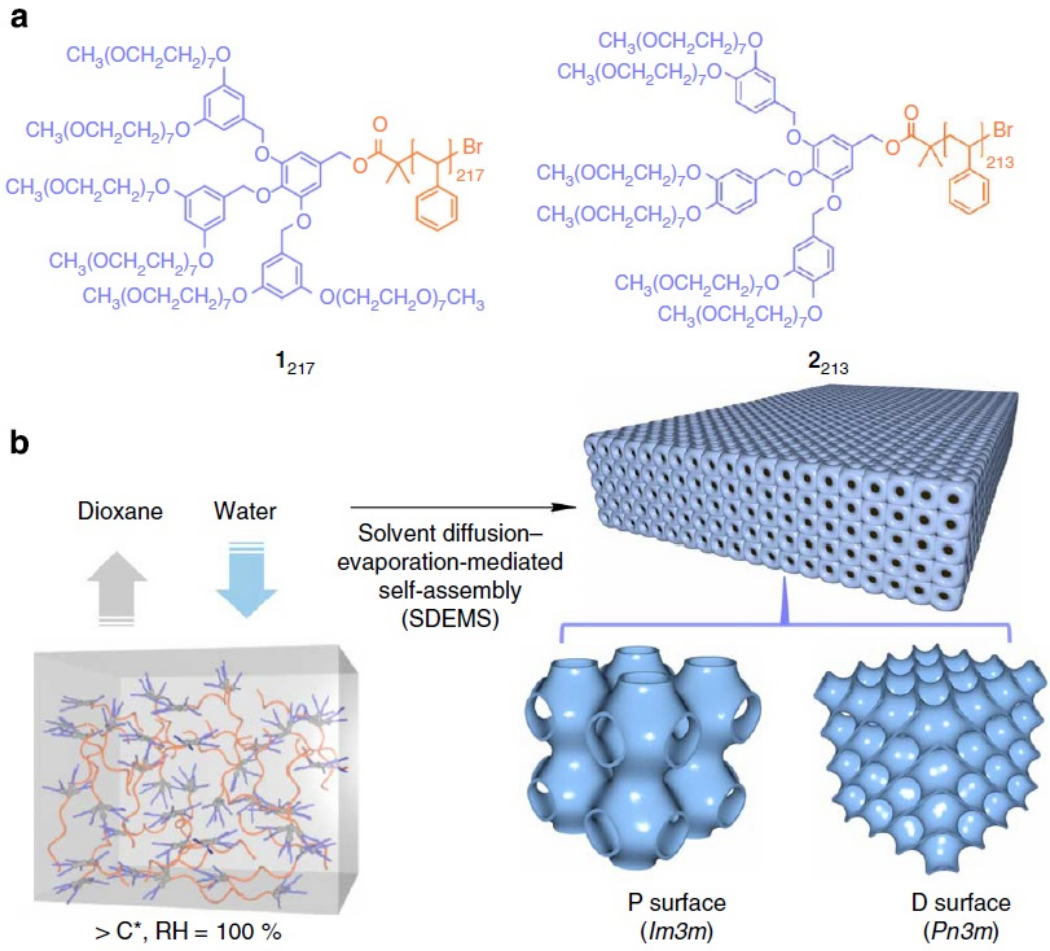

Figure 3-1. SDEMS of dendritic-linear BCPs. (a) Chemical structures of dendritic-linear BCPs used in this study. The subscript indicates the average number of repeat units in the PS block. The weight fraction of the PEG domain is 9.3% for 1_{217} and 9.4% for 2_{213}. (b) Schematic illustration of SDEMS process and the monolith consisting of the IBC structures of the BCP bilayers.

Solvent diffusion–evaporation-mediated self-assembly of BCPs. In the routine practice for the self-assembly of dendritic-linear BCPs such as 1_{217} and 2_{213} (Figure 3-1a) in dilute solution (cosolvent method), water, a poor solvent for the hydrophobic PS block, is gradually introduced to the BCP solution dissolved in dioxane, a common solvent for both of the polymer blocks. The addition of water destabilizes the PS blocks and consequently results in the aggregation of these PS blocks to form the core of the bilayer membrane, which has a corona composed of the PEG domain. This process inevitably requires physical agitation of the solution to ensure a homogeneous mixing of the two solvents, which renders the resulting self-assembled structures to be colloidal polymer cubosomes with microscaled sizes.[36] Therefore, the inverse bicontinuous structures formed in solution by self-assembly of BCPs remained colloidal particles rather than macroscopic objects such as films and monoliths.

To avoid this formation of colloidal particles in solution, we devised a method to introduce water into the dioxane solution of the BCP without physical agitation or perturbation. We imagined that, under saturated humidity (relative humidity = 100%), water vapor in the atmosphere would diffuse into the dioxane solution of 1_{217} cast on a stationary substrate, with dioxane evaporating into the atmosphere. When the critical water content within the dioxane solution is reached (~15 vol%), the self-assembly of 1_{217} would be initiated from the air-solution interface where the water content is presumably highest. We assumed that the formation of the IBC phases of the BCP would proceed downwards from the interface caused by diffusion of water. This method would ensure unperturbed growth of the monolith consisting of the IBC structure of the BCP because of the fast kinetics of self-assembly of 1_{217} in solution.

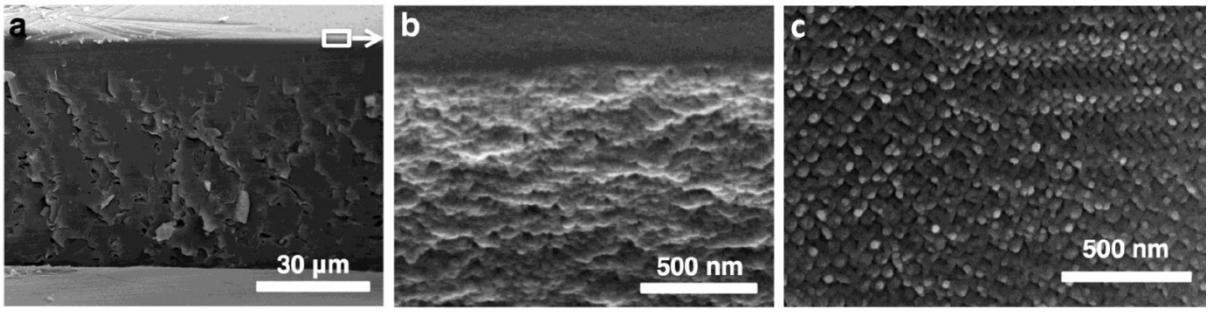

Figure 3-2. SEM images of (a) the cross-section, (b) the top portion, and (c) the bottom side views of the monolith from 1_{217} after premature quenching of the self-assembly.

We tested our method, namely 'solvent diffusion-evaporation mediated self-assembly' (SDEMS; Figure 3-1b), by placing a dioxane solution (12 wt%) of 1_{217} cast on a glass substrate (0.5 mm wet film thickness) in a sealed humidity chamber (relative humidity = 100%, 23 °C). After 1 h, the glass substrate was removed from the chamber and immersed into water to quench the assembly process by vitrification of the PS blocks. After removing dioxane by solvent exchange in water, we obtained the opaque monolithic film of 1_{217}. Observed on scanning electron microscopy (SEM), this monolithic film revealed that the internal IBC structures consisting of the bilayer of 1_{217} resided under the top layer (~10 μm thick) without any defined mesostructures (Figure 3-2). When the same dioxane solution of 1_{217} was placed in the same chamber filled with dry N_2, we did not observe any formation of the IBC structures of the BCP. Instead, a transparent film without any mesoscaled internal structure was observed after solvent evaporation. We also observed the formation of polymer cubosomes instead of monoliths when the dilute dioxane solution of 1_{217} (0.5–3 wt%) was used for the SDEMS (Figure 3-3). This observation indicated that the formation of the inverse bicontinuous mesophase of 1_{217} was the result of the self-assembly of the BCP in solution rather than the microphase separation of the BCP in bulk during the solvent evaporation.

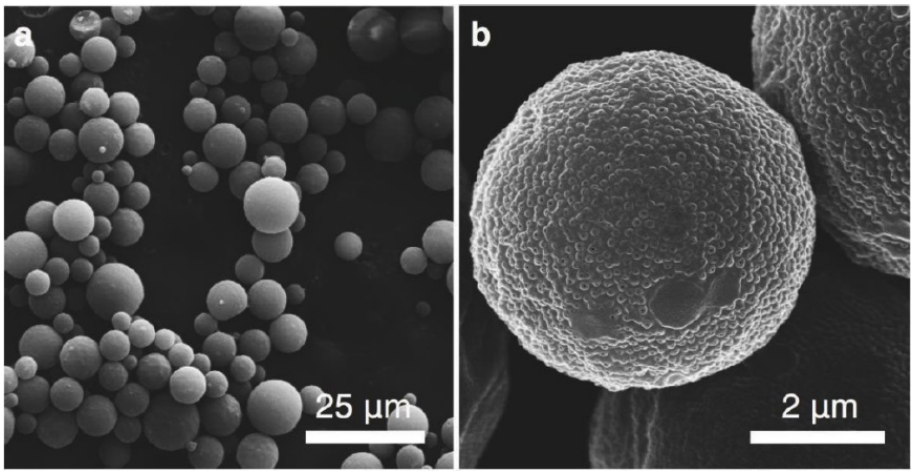

Figure 3-3. SEM images of polymer cubosomes prepared from the dilute dioxane solution (1 wt%) of 1_{217} under SDEMS condition. The average diameter of cubosomes is ~ 6.6 μm. The outer surface of the cubosomes shows the porous structure from the perforated lamella.

As the rate of dioxane evaporation under saturated humidity during the SDEMS process is directly related to the rate of the increase of water content, we expected that the kinetics of self-assembly of BCPs could be controlled by reducing the rate of dioxane evaporation. To prevent a premature quenching of the self-assembly of the BCP by a rapid increase of the water content, resulting in the formation of a featureless bulk of the BCP at the air-solution interface, we presaturated the humidity chamber with a mixture of water and dioxane (1:1 v/v) with an expectation that the dioxane vapor in the atmosphere would reduce the vapor pressure of the solvent, and thus slow down the rate of evaporation of the organic solvent.

Under these conditions, a dioxane solution of 2_{213} (12 wt%) was cast on a glass disk (2.5 cm diameter, 0.3mm wet film height), and the coated disk was placed in a humidity chamber presaturated with a dioxane/water mixture (1:1 v/v) at 23 °C. After 1 h, the resulting disk was removed from the humidity chamber and immersed in excess water to remove residual dioxane, which yielded an opaque monolithic film on the substrate (Figure 3-4a inset). SEM images of the resulting monolith showed that the top layer of the monolith consisted of a perforated BCP bilayer, which exhibited an array of nanopores (~10nm diameter) over the entire top surface (8.5×10^9 pores per cm^2 obtained by image analysis; Figure 3-4a). Below the top perforated bilayer, a highly crystalline inverse bicontinuous structure of polymer bilayers was observed over the entire thickness of the monolith (40 μm; Figure 3-4b-e). We also observed that the disordered domains and macroscopic defects gradually appeared within the monolith of 2_{213} as the thickness of the monolith increased (Figure 3-4b). We attributed this increased disorders within the monolith to the fact that the motion of polymer chains might be kinetically limited by the concentration gradient of water as the self-assembly progressed from the air-solution interface to the substrate by diffusion of water from the interface.

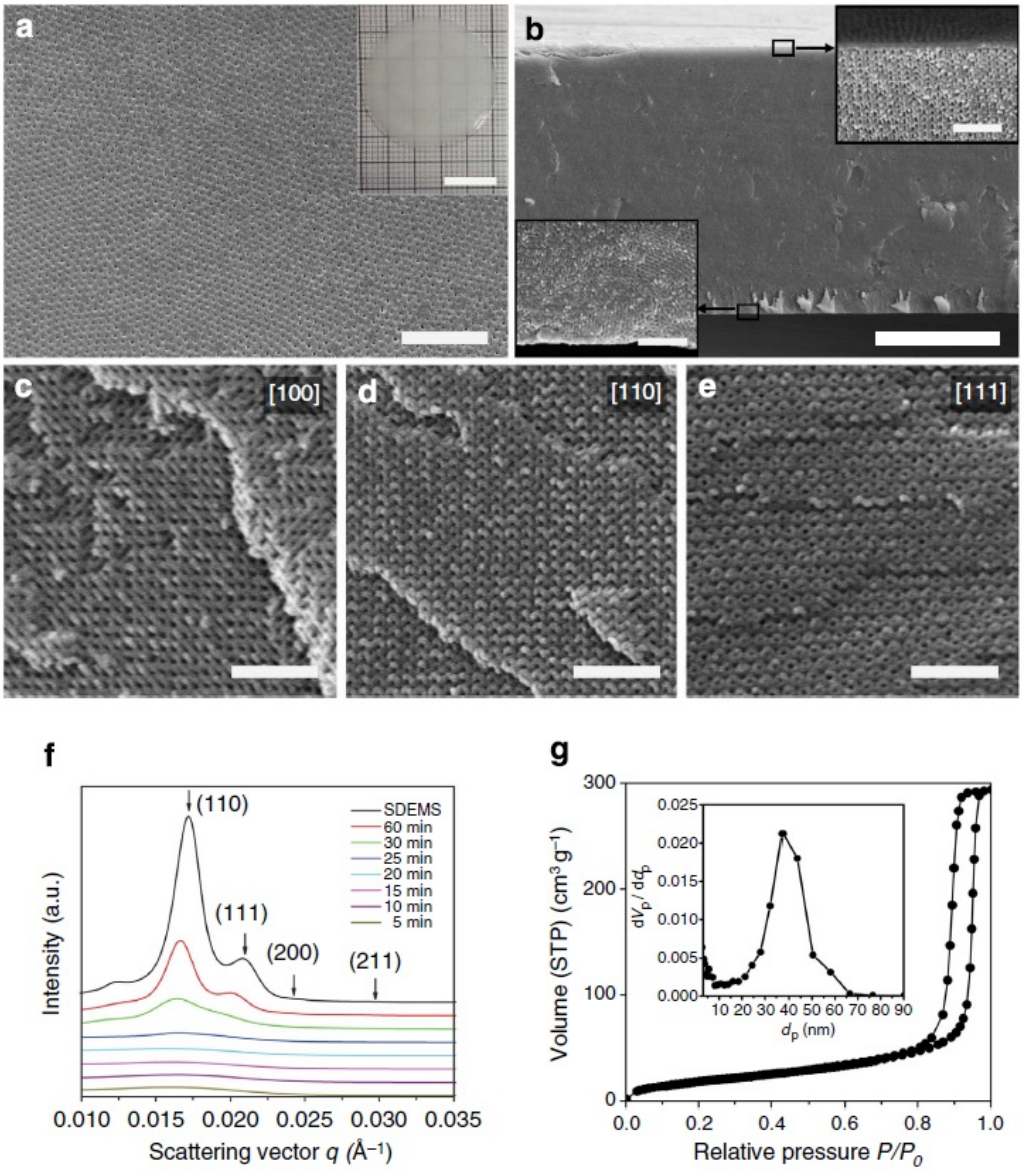

Figure 3-4. Structural characterization of the monolith of 2_{213}. (a) SEM images of the top layer of the monolith showing a perforated polymer layer having evenly distributed nanopores (~10 nm) in a long range. Scale bar, 1 μm. The inset shows a photograph of the polymer monolith of 2_{213} prepared on a glass substrate (2.5 cm diameter, scale bar, 1 cm). (b) SEM image of the cross-section view of the monolith. Scale bar, 20 μm. The part highlighted by squares was magnified to show detailed morphology of the top and bottom edges (insets, scale bars, 500 nm). (c–e) SEM images of the internal crystalline structures of the monolith of 2_{213} of a *Pn3m* lattice showing views at [100] (c), [110] (d) and [111] (e) directions. Scale bars, 300 nm (c–e). (f) SAXS results (5–60 min) by time-interval quenching of the self-assembled structures by immersion of the monoliths of 2_{213} in liquid N_2. Black line indicates the SAXS pattern obtained by SDEMS without quenching by N_2. The peaks were indexed to *Pn3m* symmetry. (g) N_2 adsorption–desorption isotherms of the monolith of 2_{213}. The inset shows the BJH pore size distribution peaked at 37 nm.

SEM images of the fractured monolith of 2_{213} revealed the IBC crystalline structures of the BCP bilayers. These structures were assigned to a double-diamond lattice (D surface, *Pn3m* symmetry, lattice constant (a) = 51.7 nm) by synchrotron small angle X-ray scattering (SAXS) (Figure 3-4f). Under the identical condition, 1_{217}, an isomeric analogue to 2_{213} that differs only in the structure of the benzyl ether dendritic block (Figure 3-1a), self-assembled to form a monolith exhibiting similar morphology to the monolith of 2_{213} (Figure 3-5). The internal structure of the monolithic film of 1_{217} was assigned to a primitive cubic lattice (P surface, *Im3m* symmetry, a = 82.4 nm) coexisting with a double-diamond lattice (D surface, *Pn3m* symmetry, a = 64.1 nm) by SAXS and SEM. We, therefore, used the monolith of 2_{213} for further structural characterization and our studies owing to the homogeneity of the internal crystalline lattice. The D surface structure also has been proposed to provide materials with interesting functions such as full bandgap photonic crystals and multifunctional hybrid materials such as a highly electrically conductive but poorly thermally conductive materials.[11,12]

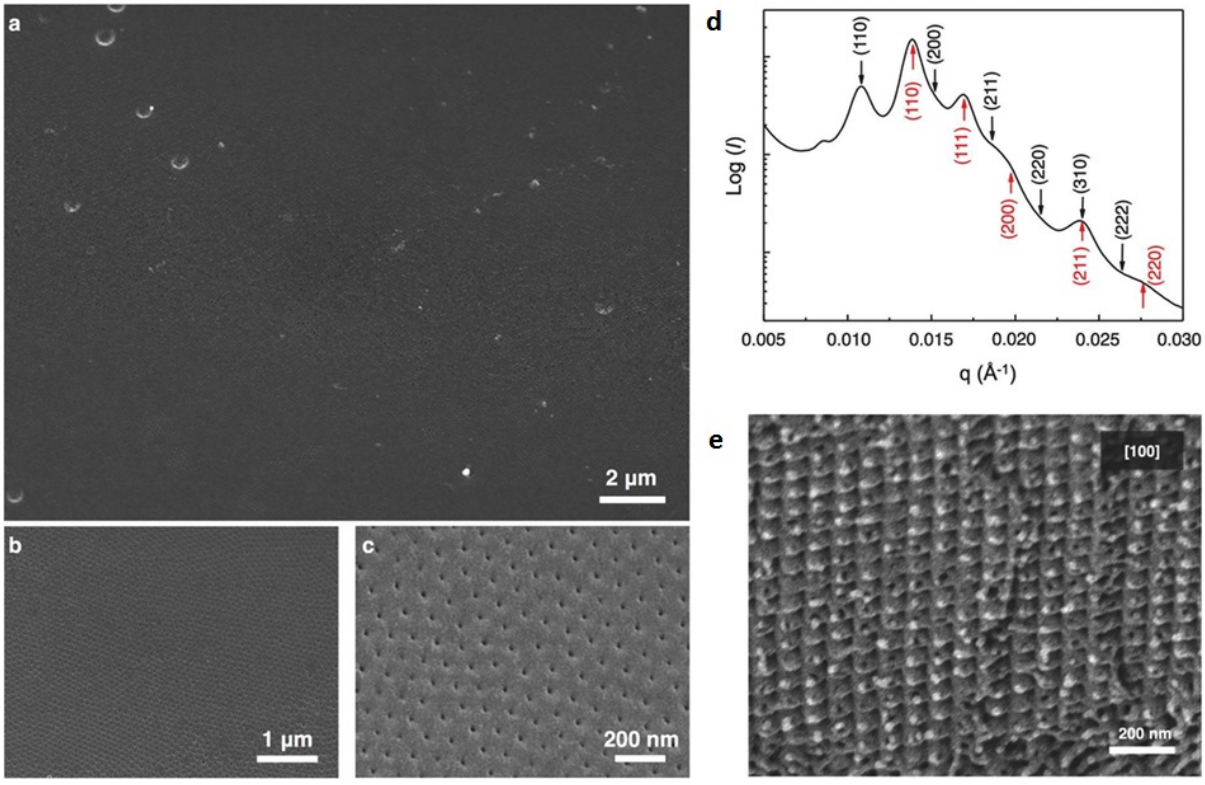

Figure 3-5. Structural characterization of the monolith of 1_{217}. (a-c) SEM images of the top perforated layer of the monolith from 1_{217}. The top layer of the monolith consisting of perforated BCP layer exhibits an array of nanopores (~10 nm diameter) over the entire top surfaces (8.5×10^9 pores cm^{-2}). (d) SAXS data showing the mixed phases of *Im3m* and *Pn3m*. Black and red arrows respectively indicate a primitive cubic lattice (*Im3m*) and double diamond lattice (*Pn3m*). (e) SEM image for the monolith of 1_{217} at the [100] projection of *Im3m*.

The formation of the internal IBC structure of the bilayer of 2_{213} was traced using time-interval quenching of the self-assembled structure by immersion of the monolith in liquid N_2, followed by a rapid exchange of the solvent by immersing the frozen structure in water. The rapid cooling of the self-assembled structure of 2_{213} with liquid N_2 ensured that the BCP chains were in the glassy state, resulting in a minimal rearrangement of BCP chains while removing dioxane from the monolith. The quenched samples at each time interval were examined by SAXS and SEM. The results showed a gradual growth of the D surface of the BCP bilayer within the monolith over 1 h (Figure 3-4f and 3-6). From the SAXS results of the monolith of 2_{213} prepared by SDEMS, we observed a weak peak appearing at low q region, which might result from the presence of disordered single continuous phases (Figure 3-4f).[38] Residual solvent molecules localized in the PS-rich domain would plasticize the PS blocks constituting the bilayer, and, therefore, could develop a pressure for the local grains of *Pn3m* symmetry to be rearranged to a single-diamond phase with some disorder.[39]

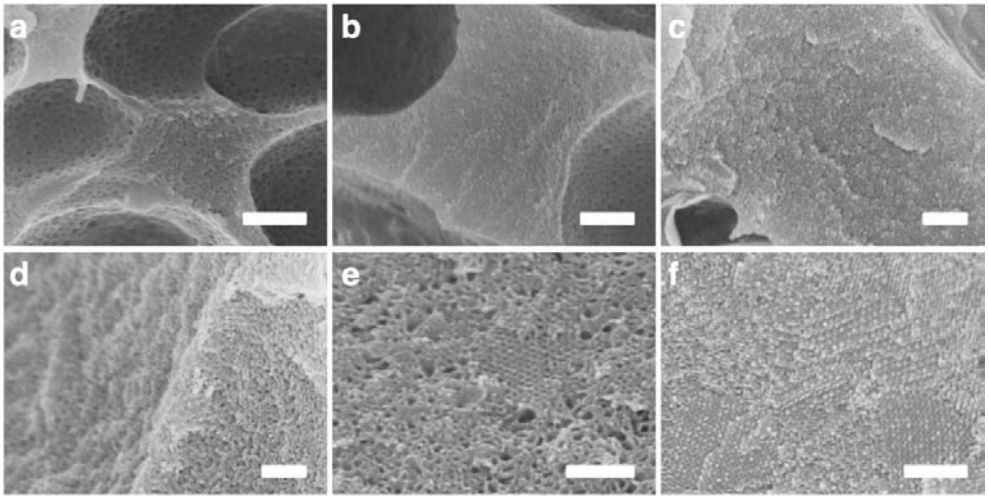

Figure 3-6. Time-course SEM analysis of mesoporous monoliths from 2_{213} after quenching at (a) 10 min, (b) 15 min, (c) 20 min, (d) 25 min, (e) 30 min, and (f) 60 min during SDEMS (scale bars, 500 nm). The regular structures of *Pn3m* were gradually evolved.

As expected from the materials composed of glassy PS polymer blocks, the monoliths of dendritic-linear BCPs maintained the structural integrity at room temperature upon drying the solvents. The N_2 adsorption–desorption isotherms at 77 K revealed that the monolith of 2_{213} exhibited a large surface area ($73 m^2 g^{-1}$) and pore volume ($0.45 cm^3 g^{-1}$) determined by Brunauer–Emmett–Teller (BET) analysis. The Barrett, Joyner and Halenda (BJH) analysis revealed the pore size distribution at 32 nm, which coincided with the observed pore dimension by SEM studies (Figure 3-4g). The size and the thickness of the monolith were scalable as the BCP solution could be cast on a substrate of any size, and the thickness of the resulting monolithic film was proportional to the wet thickness of the polymer solution cast on a substrate. Using the SDEMS method, we were able to prepare a monolith of

dendritic-linear BCPs with a thickness of 400 μm on a 25 cm^2 glass slide (Figure 3-7).

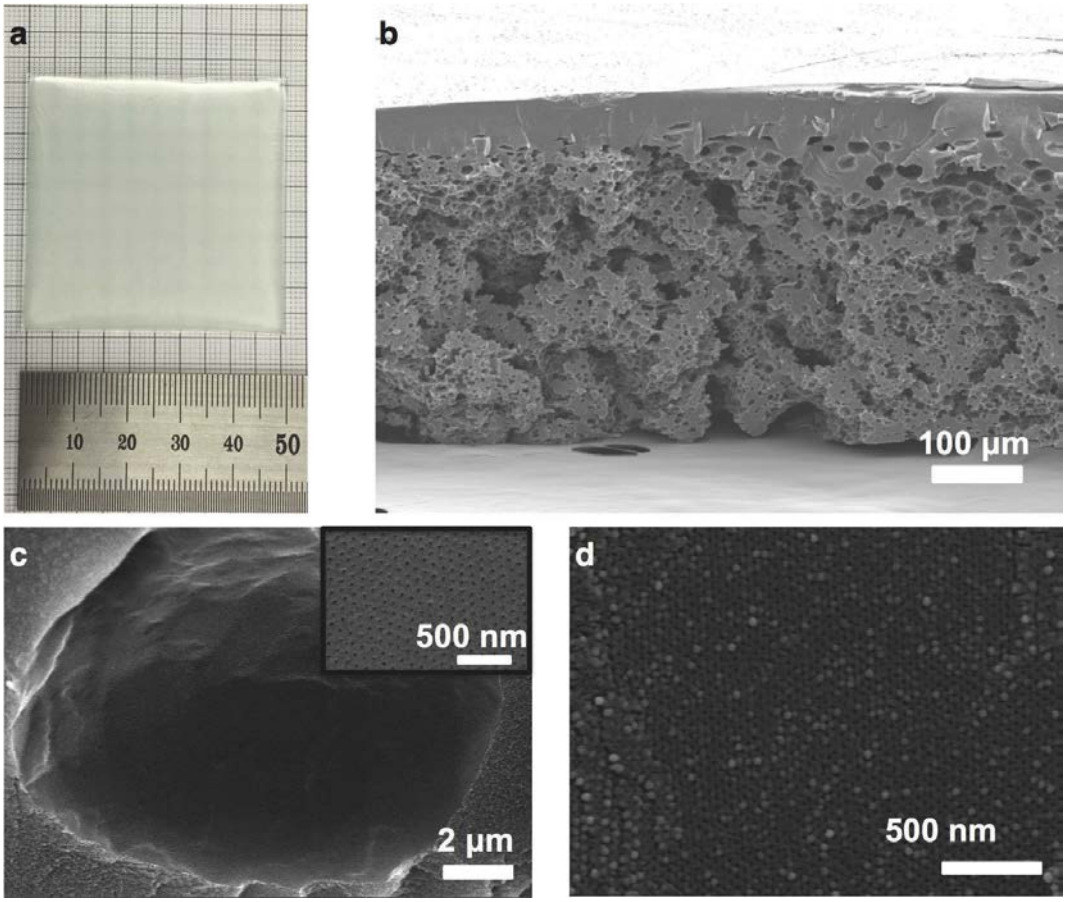

Figure 3-7. (a) The photograph shows the polymer monolith of 2_{213} on a glass slide (25 cm^2). (b) The cross-section view of SEM indicates the thickness of the monolith is ~ 400 μm. (c) The top-surfaces of macroporous portions showing perforated bilayers. The inset shows a regular pore arrangement. (d) All other portions showed the regular structures of *Pn3m*, as shown in the SEM image.

Surface functionalization of the mesoporous monoliths. The bicontinuous cubic networks of large pores embedded within the IBC structure of the BCP bilayers could allow these porous polymer monoliths to be used as platforms for applications such as protein separation, biochemical transformation and nanotemplating.[36,37] To demonstrate the accessibility and usability of the internal networks of the water channels within the polymer monoliths, we introduced surface amino groups throughout the BCP bilayer by the co-assembly of 2_{213} and NH_2–PEG_{45}–PS_{210}, a linear BCP with an α-amino group at the hydrophilic PEG block under the SDEMS condition (2_{213}/NH_2–PEG_{45}–PS_{210} 93:7 w/w in dioxane).[36] The resulting surface-functionalized porous monolith exhibited the identical structural characteristics to the monolith of 2_{213}, and showed an internal D surface structure (*Pn3m*) by SAXS and SEM (a = 63.2 nm; Figure 3-8).

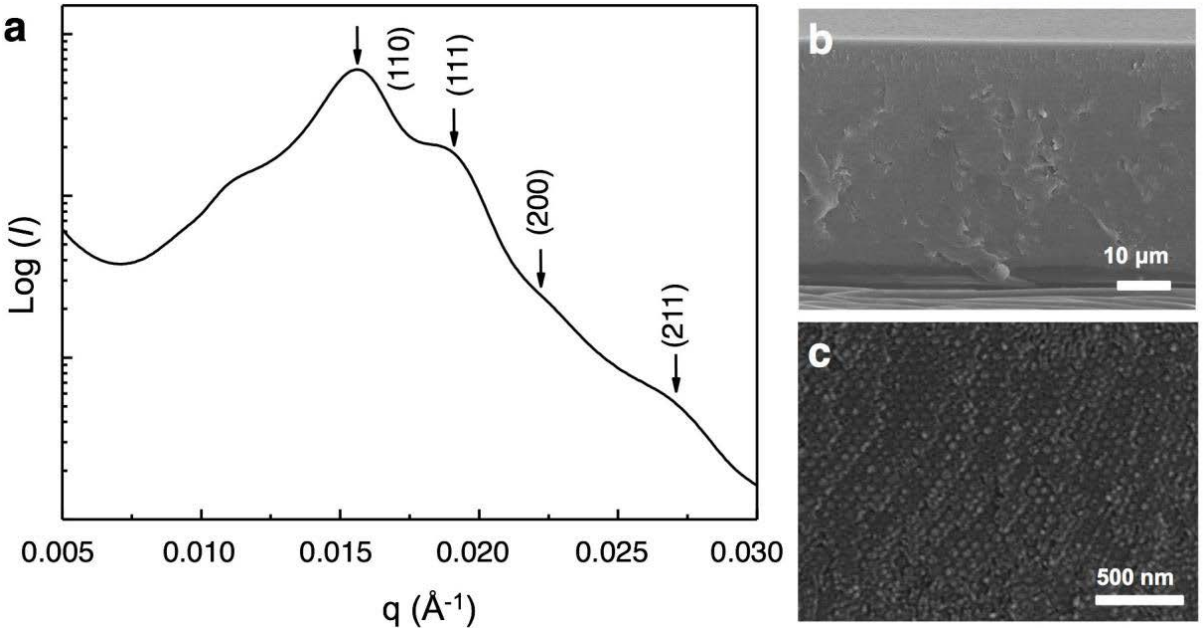

Figure 3-8. SAXS data and SEM images of the co-assembled polymer monoliths of 2_{213} / NH_2-PEG_{45}-PS_{210} (93:7 w/w in dioxane). (a) The SAXS result of the co-assembled polymer monoliths shows double diamond (*Pn3m*) lattice (a = 63.2 nm). (b) SEM image of a cross section of the functionalized monoliths. (c) High-magnification SEM image of internal structure shows a double diamond lattice viewed in the [111] direction.

The surface amino groups of the monolith were converted to biotins to anchor streptavidin homo-tetramer labelled with fluorescein (54 kDa, Sigma) using the strong non-covalent interaction between biotin and streptavidin. On confocal laser scanning microscopy (CLSM), the resulting monolith showed a strong green fluorescence over the entire area (~1 cm^2) and thickness (~40 μm), which indicated that the fluorescein-labelled streptavidin was successfully bound to the surface biotin within the water channel networks. This streptavidin-bound monolith was immersed in a solution of the biotin-mCherry fluorescent protein (35 kDa; Ref. 40), which yielded the monolith clearly showing cherry-colored fluorescence owing to the binding of biotin-mCherry to the remaining binding sites of the surface-bound streptavidin (Figure 3-9a). The axial intensity profile of fluorescence revealed the coexistence of streptavidin and biotin-mCherry fluorescent protein along the optical axis, which indicated the sequential binding of both proteins on the internal surface of the mesoporous networks within the monolith. The gradual decrease of fluorescence intensity along the depth of the monolith was derived from photobleaching during the measurement (Figure 3-9c). This result demonstrated that the easy access of large guest molecules such as proteins and their complexes could easily access the internal networks of the large water channels of the polymer monolith.

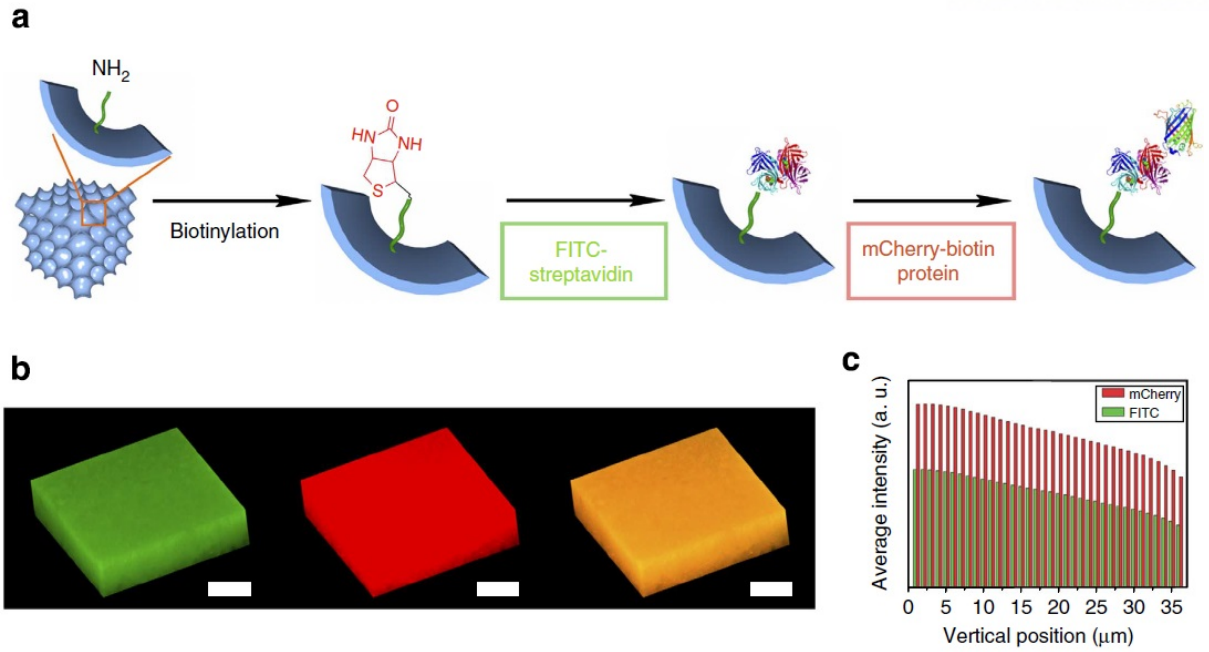

Figure 3-9. (a) Schematic illustration of surface functionalization of the monolith of 2_{213}/NH_2-PEG_{45}-PS_{210} (93:7 w/w in dioxane) with protein complexes. The biotinylated monolith was complexed with fluorescein isothiocyanate-labelled streptavidin homo-tetramer. mCherry-biotin fluorescent protein was further assembled with the streptavidin on the surface of the monolith. Excess proteins was removed by rigorous washing procedures. (b) CLSM images of the biotinylated monolith of 2_{213}/NH_2-PEG_{45}-PS_{210} (93/7 w/w) after binding of fluorescein isothiocyanate-streptavidin (λ_{em} = 519 nm, left of panel). Subsequent binding of biotinylated-mCherry fluorescent protein (λ_{em} = 610 nm, center of panel) showed cherry-colored fluorescence. Two images were merged (right of panel). The image was taken from 127×127×34 μm (width/height/depth) region near the top surface of the monolith. Scale bars, 40 μm. (c) Axial intensity profile of CLSM images along the optical axis was recorded from x, y, z image stacks, revealing the distributions of proteins.

Templated synthesis of skeletal inorganic structures. These internal large-pore networks of the BCP monolith could be translated into the 3D self-supporting skeletal networks of functional organic and inorganic materials, which have structural symmetry inherited from the IBC structure comprising the BCP monolith (Figure 3-10). Therefore, we introduced liquid precursors of inorganic oxides such as titanium (IV) isopropoxide (Ti(O*i*Pr)$_4$) into the D surface monolith of 2_{213} (thickness 40 μm, 1 cm^2 area). Following the acid-catalyzed crosslinking of Ti(O*i*Pr)$_4$ to form TiO_2, the resulting white monolith was sintered at 500 °C under ambient condition for 3 h to remove the BCP template (Figure 3-10; Refs 41,42). The SEM and transmission electron microscopy (TEM) images of the resulting TiO_2 monolith (Figure 3-11a–c and 3-12) showed that the monolith consisted of a skeletal replica of the water channel networks residing in the polymer monolith. SAXS analysis of the skeletal TiO_2 monolith revealed a diffraction pattern of the single-diamond phase (*Fd3m* symmetry) (Figure 3-12g

and ref. 38). Thermal treatment during calcination possibly affects structural constraints and causes a rearrangement of *Pn3m* to *Fd3m* owing to the increased mobility of polymer chains during calcination at the temperature well above glass transition temperature (T_g) of PS block (Figure 3-10 and 3-11; ref. 39).

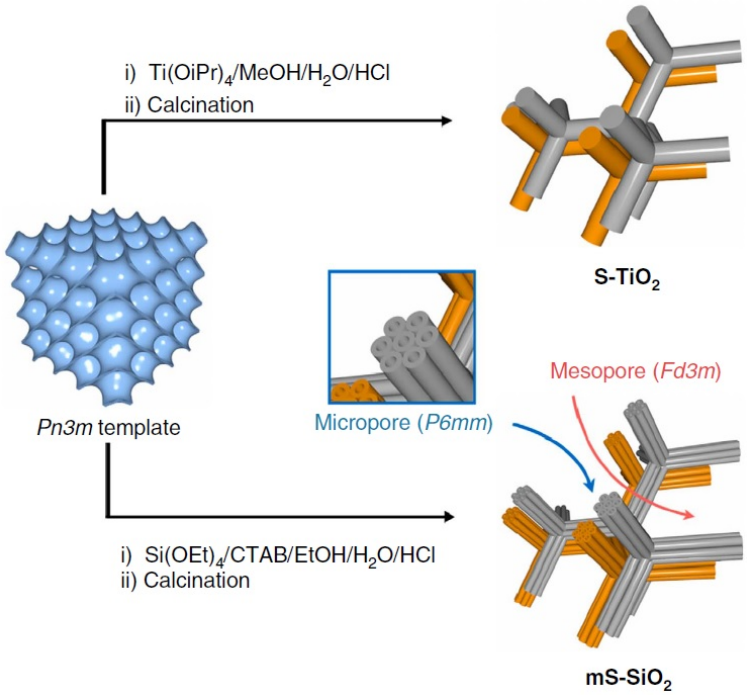

Figure 3-10. 3D skeletal inorganic nanostructures replicated from the monolith of 2_{213}. The monoliths of 2_{213} were used as templates for the fabrication of 3D skeletal porous inorganic nanostructures. The monoliths were immersed in each precursor solutions and excess solutions were removed before the calcination. mS-SiO_2 was schematically drawn to represent the hierarchically porous structure in which hexagonally ordered nanopores were incorporated into the skeletons consisting the self-supporting networks.

The energy-dispersive X-ray spectroscopy mapping on TEM confirmed that the resulting 3D skeletal structures consisted of TiO_2 (S-TiO_2) (Figure 3-11c). The mean diameter of the constituting TiO_2 skeletons was determined to 15.5 nm by porosimetry, which was in line with the SEM and TEM images. We further revealed the characteristics of S-TiO_2 at the atomic scale by X-ray diffraction, which showed a pattern of the crystalline phase of TiO_2 in an anatase form. High-resolution TEM images of the skeletons of S-TiO_2 clearly showed a well-defined lattice space (0.38 nm) of the typical (100) crystalline plane of anatase TiO_2 (Figure 3-11d).

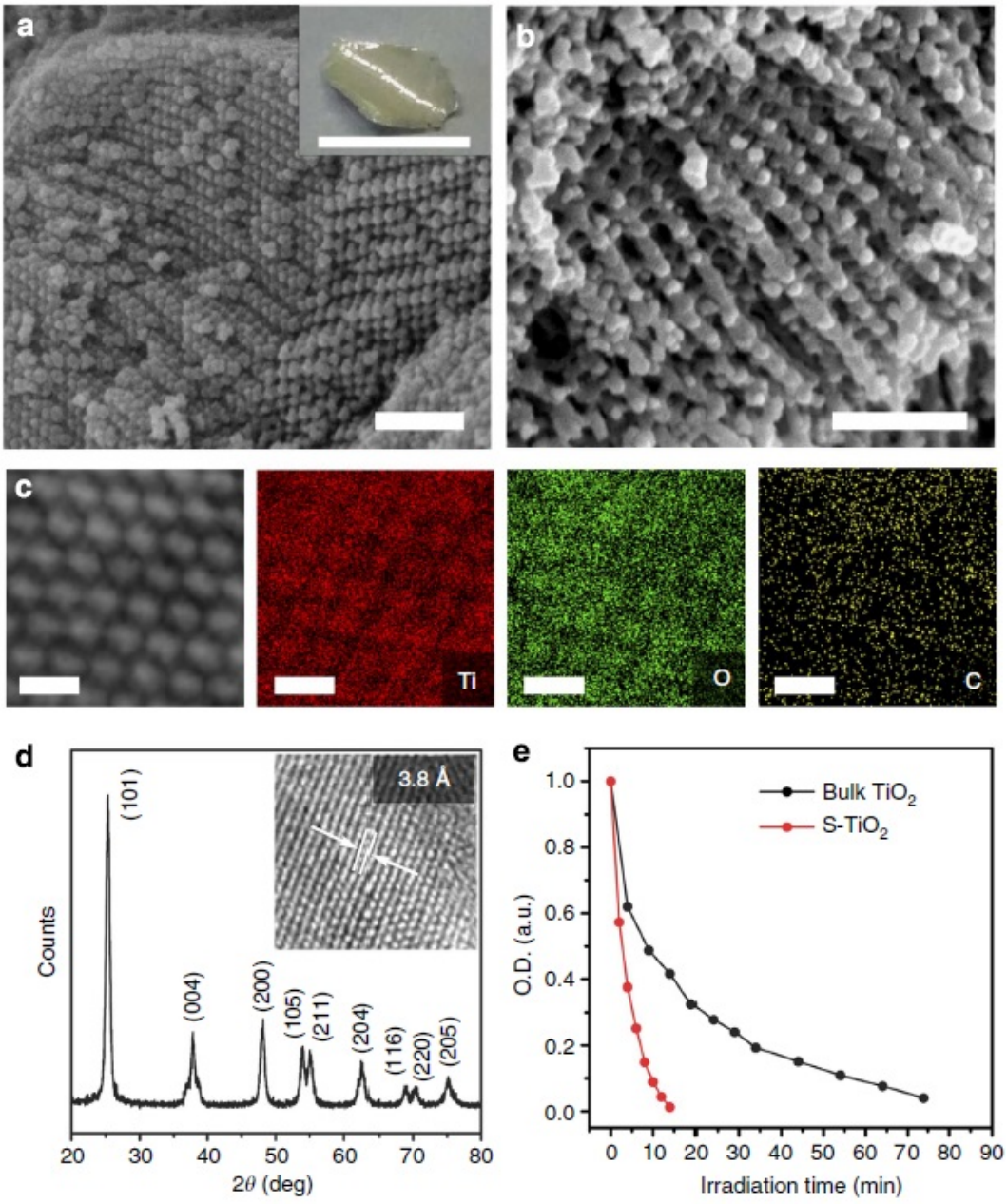

Figure 3-11. Photocatalytic porous TiO_2 nanostructures replicated from the monolith of 2_{213}. (a, b) SEM images of S-TiO_2 synthesized within the mesoporous monolith of 2_{213}. Scale bars, 300 nm. The inset in (a) shows a photograph of S-TiO_2 monolith. (scale bar, 5 mm). (c) EDS (Energy-dispersive X-ray spectroscopy) mapping of S-TiO_2 replicated from the monolith of 2_{213}. Scale bars, 50 nm. (d) X-ray diffraction data of the anatase TiO_2 skeletons consisting of the skeletal nanostructures. The inset shows a TEM image of the lattice structures of anatase TiO_2 skeletons. (e) Comparison of the photocatalytic activity of S-TiO_2 with that of bulk TiO_2 under the same experimental conditions. The y axis indicates the optical density of the methylene blue solution, whereas the x axis indicates the ultraviolet light irradiation time.

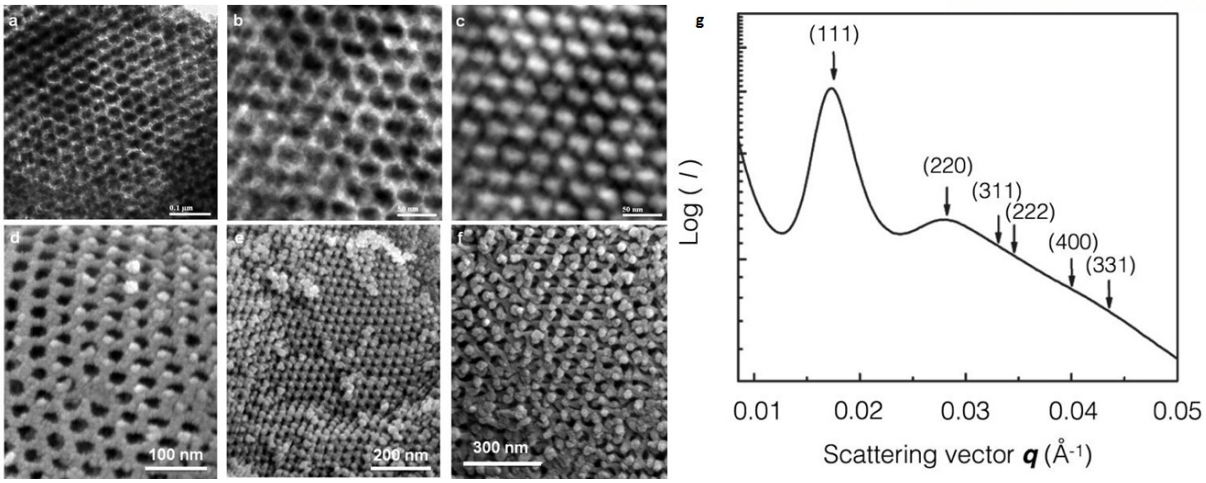

Figure 3-12. (a-b) Bright filed TEM images and (c) high-angle annular dark-field scanning transmission electron microscopy (HAADF-STEM) image of S-TiO_2. (d-f) SEM images of S-TiO_2 showing the shift of bicontinuous phase to single diamond network. (g) The SAXS result of S-TiO_2 shows single diamond (*Fd3m*) phase.

We investigated the photocatalytic activity of S-TiO_2 by monitoring the change in optical absorbance of methylene blue, which can be found as a water contaminant from dyeing processes.[43] Upon irradiation of a 3 ml methylene blue solution in the presence of S-TiO_2 (3 mg), the photodegradation of methylene blue was complete after 14 min, while the commercial TiO_2 nanoparticles (Sigma, <25nm particle size) under the same experimental condition took nearly 80 min (Figure 3-11e). The kinetics of the photodegradation reaction was plotted to a pseudo-first order rate law using $\ln(C_0/C) = kt$, where k is the apparent rate constant and t is the irradiation time.[44] The average reaction rate constant of k for S-TiO_2 was 0.2764 min^{-1}, which was 6.4 times that of the reference anatase TiO_2 nanoparticles (k = 0.0434 min^{-1}). BET analyses revealed that the surface area (80m^2 g^{-1}) of S-TiO_2 is greater than that of TiO_2 nanopowder (35m^2 g^{-1}; Figure 3-13). These results clearly indicated that the 3D skeletal nanostructure of S-TiO_2 provided an advantage to photodegradation of dyes arising from the large surface area and high accessibility to the catalytically active crystal planes.

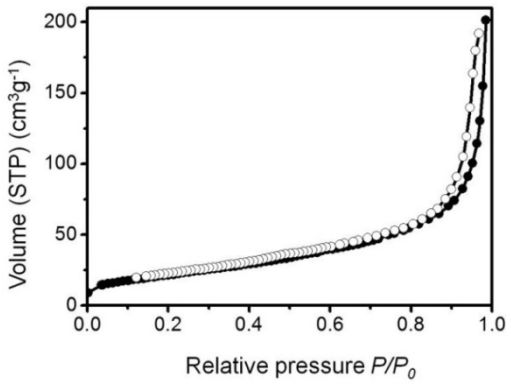

Figure 3-13. N_2 adsorption-desorption isotherms of S-TiO_2.

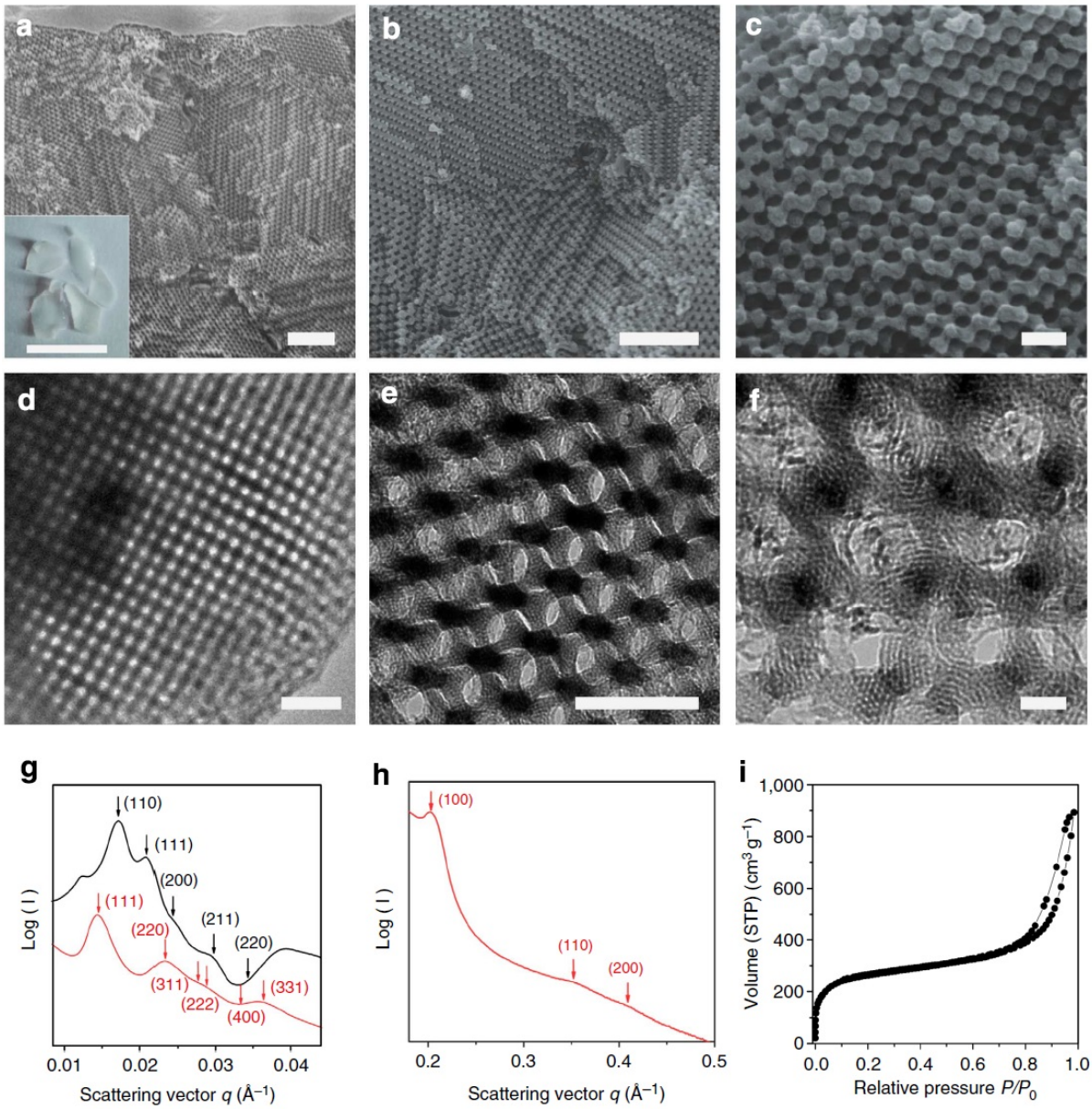

Figure 3-14. Hierarchically porous SiO_2 skeletal nanostructures replicated from the monolith of 2_{213}. (a) SEM image of the cross-section view of mS-SiO_2. The inset shows a photograph of the SiO_2 replica (scale bar, 5 mm). (b, c) SEM images of mS-SiO_2. Scale bars, 500nm (a, b) and 100nm (c). (d–f) TEM images of mS-SiO_2 replicated from the monolith of 2_{213}. Scale bars, 100 nm (d, e) and 20nm (f). (g) SAXS results of the monolith of 2_{213} (black, a = 51.7 nm) used as the template and mS-SiO_2 (red, a = 75.8 nm). The peaks were assigned to *Pn3m* (black line) and *Fd3m* (red line) symmetries, respectively. (h) SAXS result of hexagonally ordered nanopores residing in the mS-SiO_2 (a = 3.58 nm). (i) N_2 adsorption–desorption isotherms of mS-SiO_2.

We could also realize the novel example of 3D hierarchically ordered structures with multiscale pores (Figure 3-10 and Figure 3-14a–c). By infiltrating the monolith of 2_{213} with tetraethyl

orthosilicate ($Si(OEt)_4$) in the presence of cetyltrimethylammonium bromide (CTAB), the skeletal mesoporous silica could be synthesized within the large channels of the porous polymer monolith.[45] After the crosslinking of $Si(OEt)_4$ and the calcination of the polymer template, we obtained the hierarchically mesoporous skeletal SiO_2 replica (mS-SiO_2), of which the constituting silica skeletons (~18nm in diameter) possessed the hexagonally ordered nanochannels (a = 3.58 nm, pore diameter ~ 1.4 nm determined by SAXS) parallel to the long axis of the skeleton (Figure 3-14f, h). SAXS results of the resulting mS-SiO_2 showed that the symmetry breaking from *Pn3m* to *Fd3m* occurred upon heating during calcination. SEM and TEM analyses revealed the random shifting of two non-intersecting skeletal networks by showing various projections of *Fd3m* in a similar manner to the report by Ho and co-workers (Figure 3-14b–f and 3-15).[39]

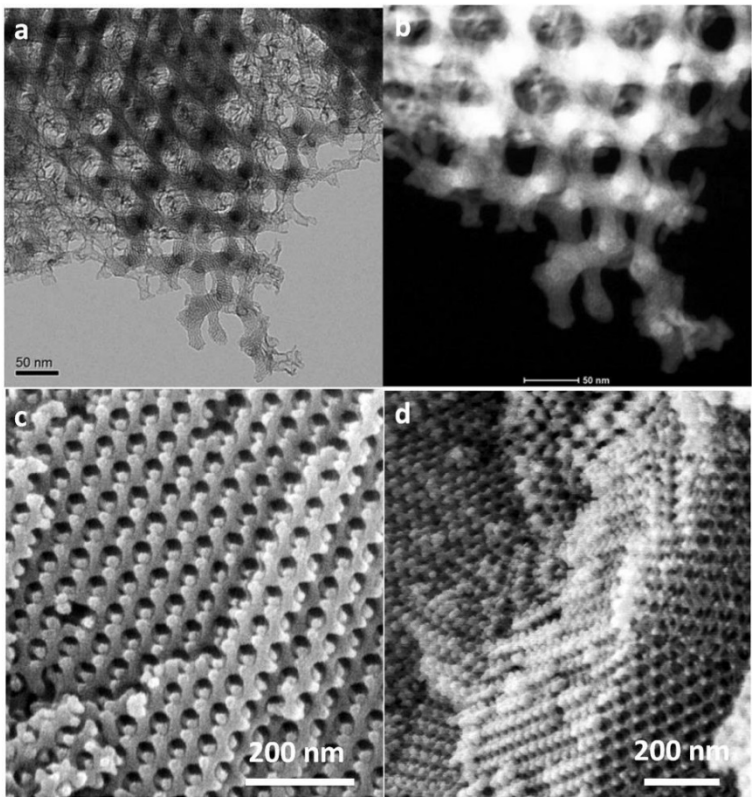

Figure 3-15. (a) Bright field TEM and (b) STEM image of the mS-SiO_2 replicated from the monolith of 2_{213} showing the hexagonally ordered nanopores within the skeleton. (c, d) SEM images mS-SiO_2 of at various projections showing shifted networks to form single diamond phase.

The hierarchically porous structure of mS-SiO_2 was also confirmed by N_2 adsorption–desorption isotherms (Figure 3-14i). The BET analysis of the isotherms showed an increased pore volume (1.38 $cm^3\ g^{-1}$) and surface area (953.7 $m^2\ g^{-1}$), which was threefold and 13-fold greater than the values of the mesoporous monolith scaffold, respectively. BJH analysis of N_2 adsorption– desorption isotherms of mS-SiO_2 showed a broad pore distribution in a range of 6–20 nm, exhibiting the mean pore diameter

of 5.9 nm (Figure 3-16). The average diameter of hexagonally ordered smaller mesopores residing in the silica skeletons was estimated to be ~1.5 nm by the Horvath– Kawazoe model analysis. This unique hierarchically porous structure could be beneficial for applications where large surface area and high accessibility to the structure are required simultaneously.[46]

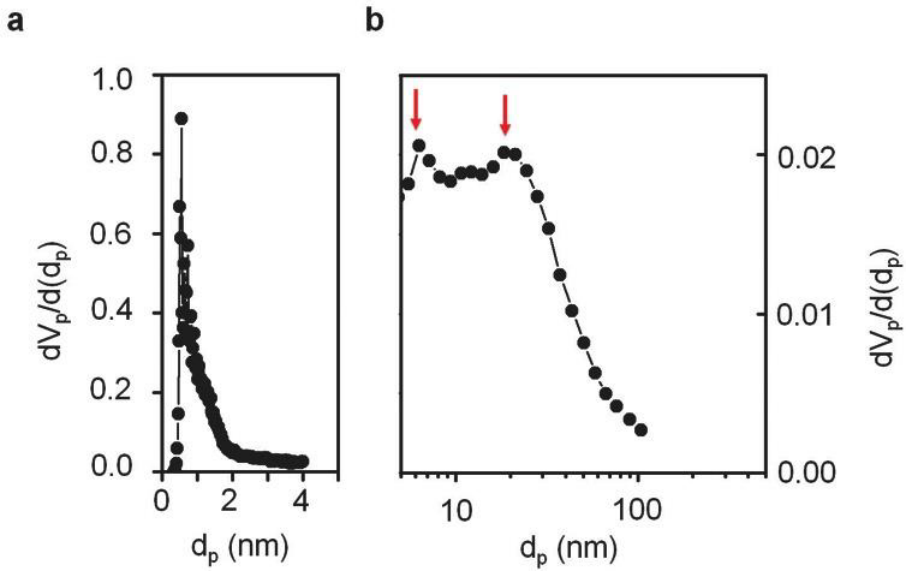

Figure 3-16. (a) Micro- and (b) meso-pore size distributions by the Horvath-Kawazoe (HK) and BJH methods on a N_2 adsorption-desorption isotherm of the $mSiO_2$-*Fd3m*.

3.4 Summary

Solution self-assembly of amphiphilic BCPs into IBC mesophases is an emerging strategy to synthesize highly ordered mesoporous polymers with reticulated mesoscale porous networks without postsynthetic processes for pore generation. This direct self-assembly of BCPs in solution generated highly ordered triply periodic porous structures with the desired surface functional groups, which rendered these porous polymers potentially useful for separation, catalysis and nanotemplating. Our method (SDEMS) to induce self-assembly of BCPs in solution without physical agitation is based on the diffusion of a poor solvent for the PS block (water) into a solution in a common solvent to both polymer blocks. The diffusion of water at the air-solution interface gradually deteriorates the solvent quality towards the PS block, which propels the dendritic-linear BCPs to form bilayers in solution.

In appearance, our method shares some resemblance to evaporation-induced self-assembly for the synthesis of mesoporous silica films.[47] Evaporation-induced self-assembly increases the surfactant concentration above the critical micelle concentration by gradually evaporating a common solvent, which allows the resulting mesoporous structures to be a form of films and monoliths. In our case, the diffusion of a poor solvent into the BCP solution is a key step to induce self-assembly because of the low critical micelle concentration values of BCPs. The rate of evaporation of a common solvent has to

be suppressed to prevent a premature kinetic quenching of self-assembly of BCPs. Non-solvent-induced phase separation method by Peinemann, Abetz, and others[14,26–31] involves a quick phase separation of BCPs at the air–solution interface caused by evaporation of solvents, which was followed by a rapid solvent exchange with non-solvent within a phase-separated domain. SIM^{2}PLE method by Wiesner and co-workers[13,17] is based on the phase separation of BCPs under solvent swollen conditions also rendered the resulting structures to be hierarchically porous polymer monoliths.

Our method ensures that the self-assembly retain the characteristics of solution self-assembly, but only without physical agitation. The results and the demonstrations shown here substantiate that the highly ordered internal large pore networks residing within the polymer monolith consisting of the IBC of the BCP bilayer could be valuable platforms for advanced separations and nanotemplating. We also point out that the results reported here suggest a new way to create highly ordered IBCs of BCP bilayers in a large scale by exploiting from the simple and fast solution self-assembly of BCPs in solution into inverse mesophases.

3.5 Experimental

General methods and materials. Nuclear magnetic resonance spectra were recorded on a Varian VNMRS 600 spectrometer with $CDCl_3$ as a solvent. Molecular weights of BCPs were measured on an Agilent 1260 Infinity GPC system equipped with a PL gel 5 mm mixed D column (Polymer Laboratories) and differential refractive index detectors. Tetrahydrofuran (THF) was used as an eluent with a flow rate of 1mL min^{-1}. A PS standard (Polymer Laboratories) was used for calibration. TEM was performed on a JEOL JEM-2100 and JEM-2100F microscope at an acceleration voltage of 200 kV. Sample specimens were prepared by placing a drop of the solution on a carbon-coated Cu grid (200 mesh, Electron Microscopy Sciences). After 30 min, remaining solution on a grid was removed with a filter paper, and the grid was air-dried for 18 h. SEM images were obtained on a FEI Nova NanoSEM 230 microscope and Hitachi S-4800 FE SEM at an acceleration voltage of 10 kV. The sample was placed on a conductive carbon layer and coated with Pt with a thickness of 3 nm by using a K575X Sputter Coater. CLSM was performed on a FluoView 1000 Confocal Microscope (Olympus). The Porous structures of the samples were analyzed by a nitrogen adsorption experiment at 77K using a BEL BELSORP-Max system. The surface areas and pore size distributions of the samples were calculated by using the BET equation and the BJH method, respectively. Small-angle X-ray scattering data were obtained on the SAXS beam line (PLS-II 9A) at Pohang acceleration laboratory (Pohang, Korea). Powder X-ray diffraction pattern was obtained on a D/MAZX 2500V/PC of Rigaku (Japan), the sample was ground before the measurement.

Synthesis of BCPs. All BCPs were synthesized and characterized by the literature procedures reported earlier (Scheme 3-1 and 3-2; refs 36,48). The characterization of resulting BCPs are summarized in Table 3-1.

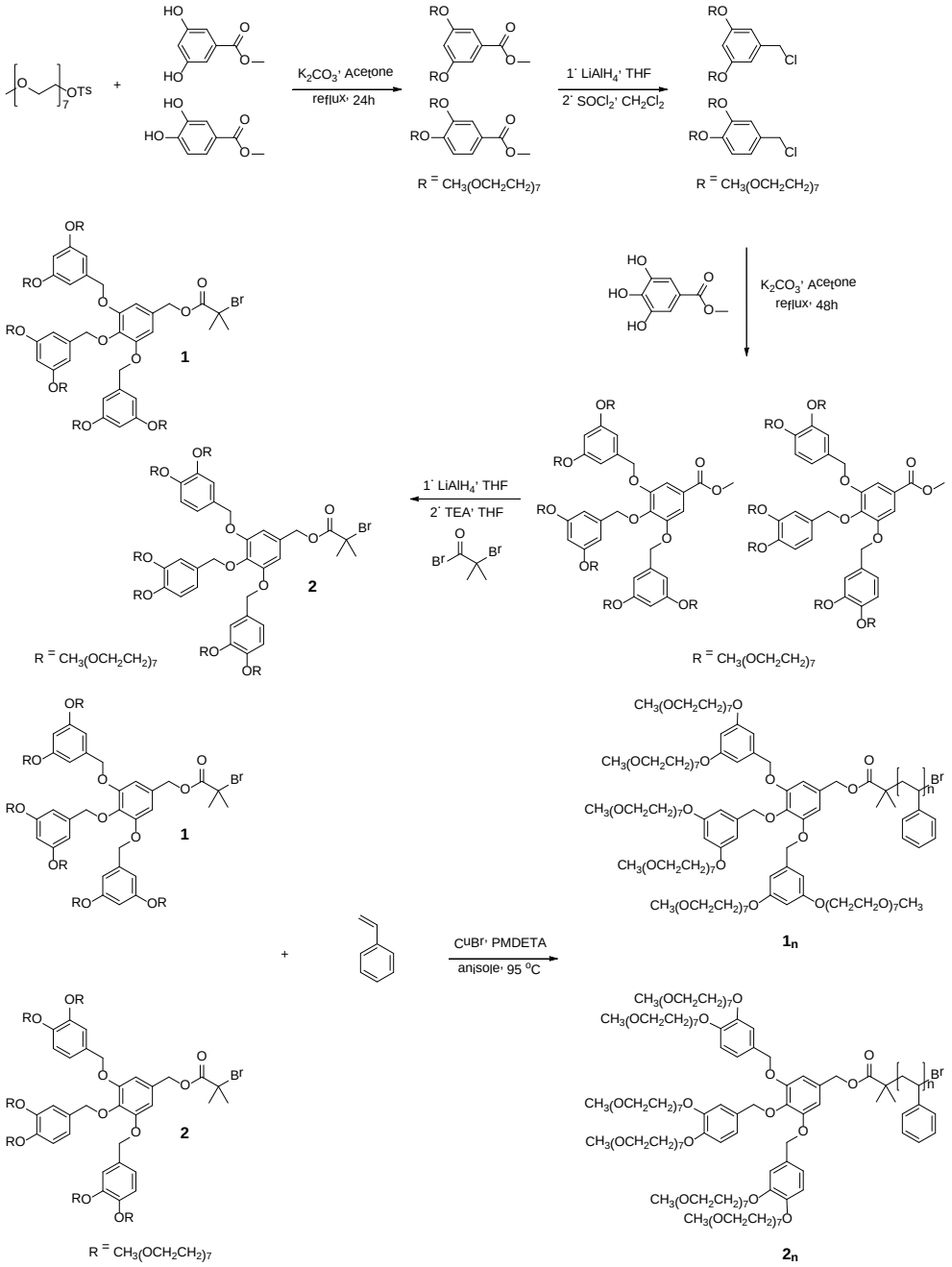

Scheme 3-1. Synthesis of dendritic macroinitiators (**1** and **2**) and dendritic-linear block copolymers (**1**$_n$ and **2**$_n$).

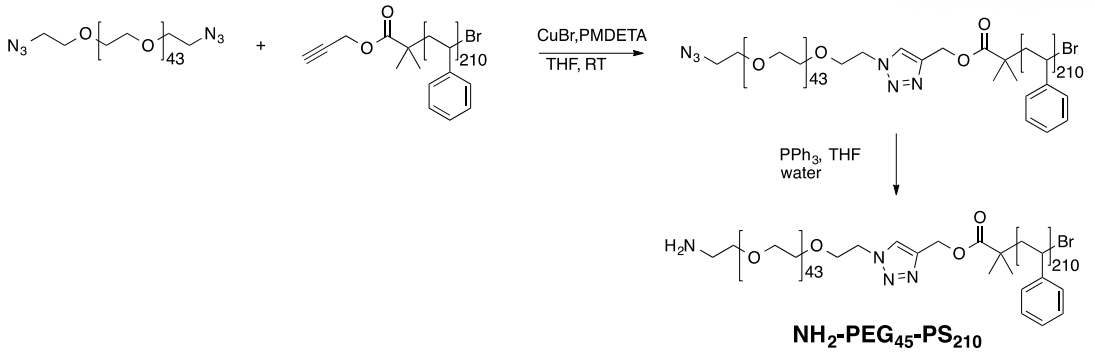

Scheme 3-2. Synthesis of NH_2-PEG_{45}-PS_{210}.

Table 3-1. Characterization of block copolymers

sample	M_n (g/mol)[a]	DP_n (PS)[b]	$Đ$[a]	f_{PEG}[c]
$\mathbf{1_{217}}$	21380	217	1.07	9.3
$\mathbf{2_{213}}$	21320	213	1.08	9.4
$\mathbf{NH_2\text{-}PEG_{45}\text{-}PS_{210}}$	23970	220	1.12	8.8

[a] The number average molecular weight and molecular weight distribution determined by GPC (THF, 35 °C, 1 mL min^{-1} flow rate) using PS standards. [b] The number average degree of polymerization of PS block determined by ^{1}H NMR integration. [c] The molecular weight ratio of the PEG domain to that of the PS block

SDEMS of BCPs. In a typical procedure, 2_{213} (20 mg) was dissolved in 1,4-dioxane (180 mg) in a 15 mL vial, and the resulting solution was kept at room temperature for 1 h before the use. A sealed humidity chamber was prepared by mixing 35 mL of 1,4-dioxane and 35 mL of water in a 100 ml vial, and then a cylindrical column to put a glass substrate was carefully added. A desired amount of the solution of 2_{213} was carefully cast on the glass slide, which was rapidly placed on the column in the humidity chamber. The humidity chamber was then sealed for 1 h. After completing SDEMS, the glass slide covered with the monolith of 2_{213} was immersed into excess water to quench the assembly process by vitrification of the PS block. The opaque monolithic film was then obtained after removing 1,4-dioxane by solvent exchange in water.

Surface functionalization of the mesoporous monolith of 2_{213}/NH_2-PEG_{45}-PS_{210}. The solution of 2_{213}/NH_2-PEG_{45}-PS_{210} (93:7 w/w in 1,4-dioxane) was applied under SDEMS condition. The monolith was then reacted with excess amount of NHS–PEG_4–biotin (1,020 eq., Thermo Scientific) for 48 h, followed by washing with methanol and PBS (pH 7.4) several times. The monolith was incubated with excess amount of streptavidin homo-tetramer having fluorescein dye (54 kDa, Sigma) in PBS (pH 7.4) for 26 h. The excess streptavidin was removed by washing with PBS (pH 7.4). The streptavidin-bound monolith was immersed in a PBS solution of the biotin-mCherry fluorescent protein (35 kDa), followed by washing with PBS (pH 7.4).

Synthesis of S-TiO_2 and mS-SiO_2. The monolith of 2_{13} (thickness 40 μm, 1 cm^2 area) was impregnated with titanium (IV) isopropoxide, and then the acid-catalyzed crosslinking of $Ti(OiPr)_4$ was allowed to form TiO_2 under HCl vapor for 2 h. The resulting white monolith was sintered at 500 °C under air condition for 3 h. Polymeric silica sol was prepared by refluxing TEOS, ethanol, water and HCl (molar ratios: $1:3:1:5\times10^{-5}$) at 80 °C for 1 h. Subsequently, CTAB solution (molar ratios, CTAB:EtOH:HCl = 0.1:17:0.00395) was added to the silica sol. The monolith of 2_{13} (thickness 40 μm, 1 cm^2 area) was soaked with the fresh sol, and aged at 40 °C for 1 h. The impregnated monolith was calcined under air condition at 520 °C for 4 h.

Typical procedure for photodegradation reaction. TiO_2 powder (3.0 mg) was suspended in aqueous solution (3 mL) of methylene blue (0.01 g L^{-1}) in a quartz cuvette. Before ultraviolet irradiation, the suspension was stirred in dark for 30 min to ensure the adsorption-desorption equilibrium of methylene blue onto the TiO_2 surfaces. The suspension was then irradiated under ultraviolet light (λ = 254 nm, 30 W). A portion of the reaction mixture was picked up from the mixture, centrifuged and analyzed by ultraviolet-visible absorption spectroscopy. The kinetics of the degradation reaction was evaluated using the equation $\ln(C_0/C) = kt$, where k is the rate constant and t is the irradiation time.

3.6 References

1. Wu, D. et al. Design and Preparation of Porous Polymers. *Chem. Rev.* **2012**, *112*, 3959–4015.
2. Jackson, E. A.; Hillmyer, M. A. Nanoporous Membranes Derived from Block Copolymers: from Drug Delivery to Water Filtration. *ACS Nano* **2010**, *4*, 3548–3553.
3. Querelle, S. E.; Jackson, E. A.; Cussler, E. L. & Hillmyer, M. A. Ultrafiltration Membranes with a Thin Poly(styrene)-*b*-Poly(isoprene) Selective Layer. *ACS Appl. Mater. Interfaces* **2013**, *5*, 5044–5050.
4. Svec, F. Porous Polymer Monoliths: Amazingly Wide Variety of Techniques Enabling Their Preparation. *J. Chromatogr. A* **2010**, *1217*, 902–924.
5. Shannon, M. A. et al. Science and Technology for Water Purification in the Coming Decades. *Nature* **2008**, *452*, 301–310.
6. Tokarev, I.; Minko, S. Multiresponsive, Hierarchically Structured Membranes: New, Challenging, Biomimetic Materials for Biosensors, Controlled release, Biochemical Gates, and Nanoreactors. *Adv. Mater.* **2009**, *21*, 241–247.
7. Lee, H.-C.; Hsueh, H.-Y.; Jeng, U.; Ho, R.-M. Functionalized Nanoporous Gyriod SiO_2 with Double-Stimuli-Responsive Properties as Environment-Selective Delivery Systems. *Macromolecules* **2014**, *47*, 3041–3051.

8. Crossland, E. J. W. et al. A Bicontinuous Double Gyroid Hybrid Solar Cell. *Nano Lett* .**2009**, *9*, 2807–2812.
9. Crossland, E. J. W. et al. Mesoporous TiO2 Single Crystals Delivering Enhanced Mobility and Optoelectronic Device Performance. *Nature* **2013**, *495*, 215–219.
10. Lee, M. M. et al. Efficient Hybrid Dolar Cells Based on Meso-Superstructured Organometal Halide Perovskites. *Science* **2012**, *338*, 643–647.
11. Torquato, S.; Hyun, S.; Donev, A. Multifunctional Composites: Optimizing Microstructures for Simultaneous Transport of Heat and Electricity. *Phys. Rev. Lett.* **2002**, *89*, 266601.
12. Martı´n-Moreno, L.; Gracía-Vidal, F. J.; Somoza, A. M. Self-Assembled Triply Periodic Minimal Surfaces as Molds for Photonic Band Gap Materials. *Phys. Rev. Lett.* **1999**, *83*, 73–75.
13. Dorin, R. M.; Sai, H.; Wiesner, U. Hierarchically Porous Materials from Block Copolymers. *Chem. Mater.* **2014**, *26*, 339–347.
14. Peinemann, K.-V.; Abetz, V.; Simon, P. F. W. Asymmetric Superstructure Formed in a Block Copolymer via Phase Separation. *Nat. Mater.* **2007**, *6*, 992–996.
15. Phillip, W. A. et al. Tuning Structure and Properties of Graded Triblock Terpolymer-based Mesoporous and Hybrid Films. *Nano Lett.* **2011**, *11*, 2892–2900.
16. Seo, M.; Hillmyer, M. A. Reticulated Nanoporous Polymers by Controlled Polymerization-Induced Microphase Separation. *Science* **2012**, *336*, 1422–1425.
17. Sai, H. et al. Hierarchical Porous Polymer Scaffolds from Block Copolymers. *Science* **2013**, *341*, 530–534.
18. Samitsu, S. et al. Flash Freezing Route to Mesoporous Polymer Nanofiber Networks. *Nat. Commun.* **2013**, *4*, 2653.
19. Zhou, N.; Bates, F. S.; Lodge, T. P. Mesoporous Membrane Templated by a Polymeric Bicontinuous Microemulsion. *Nano Lett.* **2006**, *6*, 2354–2357.
20. Wan, Y.; Shi, Y.; Zhao, D. Supramolecular Aggregates as Templates: Ordered Mesoporous Polymers and Carbons. *Chem. Mater.* **2008**, *20*, 932–945.
21. Zalusky, A. S.; Olayo-Valles, R.; Taylor, C. J.; Hillmyer, M. A. Mesoporous Polystyrene Monoliths. *J. Am. Chem. Soc.* **2001**, *123*, 1519–1520.
22. Olson, D. A.; Chen, L.; Hillmyer, M. A. Templating Nanoporous Polymers with Ordered Block Copolymers. *Chem. Mater.* **2008**, *20*, 869–890.
23. Li, L. et al. Gyroid Nanoporous Membranes with Tunable Permeability. *ACS Nano* **2011**, *5*, 7754–7766.
24. Mai, Y.; Eisenberg, A. Self-Assembly of Block Copolymers. *Chem. Soc. Rev.* **2012**, *41*, 5969–5985.
25. Schacher, F. H.; Rupar, P. A.; Manners, I. Functional Block Copolymers: Nanostructured Materials with Emerging Applications. *Angew. Chem. Int. Ed.* **2012**, *51*, 7898–7921.

26. Jung, A.; Rangou, S.; Abetz, C.; Filiz, V.; Abetz, V. Structure Formation of Integral Asymmetric Composite Membranes of Polystyrene-*block*-Poly(2-vinylpyridine) on a Nonwoven. *Macromol. Mater. Eng.* **2012**, *297*, 790–798.
27. Hahn, J. et al. Structure Formation of Integral-Asymmetric Membranes of Polystyrene-*block*-Poly(ethylene oxide). *J. Polym. Sci. Part B: Polym. Phys.* **2013**, *51*, 281–290.
28. Phillip, W. A. et al. Tuning Structure and Properties of Graded Triblock Terpolymer-based Mesoporous and Hybrid Films. *Nano Lett.* **2011**, *11*, 2892–2900.
29. Dorin, R. M. et al. Solution Small-Angle X-ray Scattering as a Screening and Predictive Tool in the Fabrication of Asymmetric Block Copolymer Membranes. *ACS Macro Lett*. **2012**, *1*, 614–617.
30. Marques, D. S. et al. Self-Assembly in Casting Solutions of Block Copolymer Membranes. *Soft Matter* **2013**, *9*, 5557–5564.
31. Qiu, X. et al. Selective Separation of Similarly Sized Proteins with Tunable Nanoporous Block Copolymer Membranes. *ACS Nano* **2012**, *7*, 768–776.
32. Mackay, A. L. Periodic Minimal Surfaces. *Physica* **1985**, *131B*, 300–305.
33. Zhang, L. et al. Mesosized Crystal-like Structure of Hexagonally Packed Hollow Hoops by Solution Self-Assembly of Diblock Copolymers. *Phys. Rev. Lett.* **1997**, *79*, 5034–5037.
34. Hales, K.; Chen, Z.; Wooley, K. L.; Pochan, D. J. Nanoparticles with Tunable Internal Structure from Triblock Copolymers of PAA-*b*-PMA-*b*-PS. *Nano Lett.* **2008**, *8*, 2023–2026.
35. McKenzie, B. E. et al. Temperature-Responsive Nanospheres with Bicontinuous Internal Structures from a Semicrystalline Amphiphilic Block Copolymer. *J. Am. Chem. Soc.* **2010**, *132*, 10256–10259.
36. La, Y. et al. Colloidal Inverse Bicontinuous Cubic Membranes of Block Copolymers with Tunable Surface Functional Groups. *Nat. Chem.* **2014**, *6*, 534–541.
37. Yu, H.; Qiu, X.; Nunes, S. P.; Peinemann, K.-V. Biomimetic Block Copolymer Particles with Gated Nanopores and Ultrahigh Protein Sorption Capacity. *Nat. Commun.* **2014**, *5*, 4110.
38. Yaghmur, A.; Laggner, P.; Zhang, S.; Rappolt, M. Tuning Curvature and Stability of Monoolein Bilayers by Designer Lipid-like Peptide Surfactants. *PLoS ONE* **2007**, *5*, e479.
39. Han-Yu Hsueh, H.-Y. et al. Shifting Networks to Achieve Subgroup Symmetry Properties. *Adv. Mater.* **2014**, *26*, 3225–3229.
40. Shaner, N. C. et al. Improved Monomeric Red, Orange and Yellow Fluorescent Proteins Derived from Discosoma sp. red Fluorescent Protein. *Nat. Biotechnol.* **2004**, *22*, 1567–1572.
41. Li, W.; Wu, Z.; Wang, J.; Elzatahry, A. A.; Zhao, D. A Perspective on Mesoporous TiO_2 Materials. *Chem. Mater.* **2014**, *26*, 287–298.
42. Gajjela, S. R.; Ananthanarayanan, K.; Yap, C.; Gra¨tzel, M.; Balaya, P. Synthesis of Mesoporous Titanium Dioxide by Soft Template Based Approach: Characterization and

Application in Dye-Sensitized Solar Cells. *Energy Environ. Sci.* **2010**, *3*, 838–845.

43. Chen, X.; Liu, L.; Yu, P. Y.; Mao, S. S. Increasing Solar Absorption for Photocatalysis with Black Hydrogenated Titanium Dioxide Nanocrystals. *Science* **2011**, *331*, 746–750.
44. Wang, X. H. et al. Wavelength-Sensitive Photocatalytic Segradation of Methyl Orange in Aqueous Suspension over Iron(III)-Doped TiO_2 Nanopowders under UV and Visible Light Irradiation. *J. Phys. Chem. B.* **2006**, *110*, 6804.
45. Lu, Y. et al. Continuous Formation of Supported Cubic and Hexagonal Mesoporous films by Sol-Gel Dip-Coating. *Nature* **1997**, *389*, 364–368.
46. Na, K. et al. Directing Zeolite Structures into Hierarchically Nanoporous Architectures. *Science* **2011**, *333*, 328–332.
47. Brinker, C. J.; Lu, Y.; Sellinger, A.; Fan, H. Evaporation-Induced Self-Assembly: Nanostructures Made Easy. *Adv. Mater.* **1999**, *11*, 579–585.
48. Jeong, M. G.; van Hest, J. C. M.; Kim, K. T. Self-Assembly of Dendritic-Linear Block Copolymers with Fixed Molecular Weight and Block Ratio. *Chem. Commun.* **2012**, *48*, 3590–3592.

Chapter 4. A morphological transition of inverse mesophases of a branched-linear block copolymer guided by using cosolvents

4.1 Abstract

We report here a strategy for influencing the phase and lattice of the inverse mesophases of a single branchedlinear block copolymer (BCP) in solution which does not require changing the structure of the BCP. The phase of the self-assembled structures of the block copolymer can be controlled ranging from bilayer structures of positive curvature (polymersomes) to inverse mesophases (triply periodic minimal surfaces and inverse hexagonal structures) by adjusting the solvent used for self-assembly. By using solvent mixtures to dissolve the block copolymer we were able to systematically change the affinity of the solvent toward the polystyrene block, which resulted in the formation of inverse mesophases with the desired lattice by self-assembly of a single branched-linear block copolymer. Our method was also applied to a new solution self-assembly method for a branched-linear block copolymer on a stationary substrate under humidity, which resulted in the formation of large mesoporous films. Our results constitute the first controlled transition of the inverse mesophases of block copolymers by adjusting the solvent composition.

4.2 Introduction

The direct self-assembly of amphiphilic block copolymers (BCPs) into inverse bicontinuous structures in solution is an emerging strategy for creating highly ordered porous polymers with three-dimensionally interconnected networks of large pores.[1–9] In a manner similar to the self-assembly of lipids such as monoolein into colloidal particles of inverse bicontinuous cubic mesophases (cubosomes) in water,[10–15] BCPs in solution could be directly self-assembled into colloidal particles of inverse bicontinuous cubic phases of the BCP bilayer (polymer cubosomes).[1–7,16–19] We recently reported that diblock copolymers, composed of a dendritic or branched hydrophilic block and a hydrophobic linear polymer block, preferentially self-assemble into triply periodic minimal surfaces (TPMSs) of the BCP bilayers in solution, resulting in the creation of polymer cubosomes having highly defined internal large-pore networks.[16–18] The TPMSs of the BCP bilayers exhibited distinct crystalline structures such as primitive cubic (*Im3m*, P surface), double diamond (*Pn3m*, D surface), and gyroid (*Ia3d*, G surface) lattices, depending on the architecture of the dendritic hydrophilic block as well as the block ratio between two distinct polymer domains. The polymer cubosomes of these BCPs exhibited a large surface area, which could be functionalized by implementing the desired functional groups through co-assembly with linear BCPs with a-functionalized hydrophilic blocks. Moreover, the TPMSs of the BCP bilayer could be expanded to large-scale films by the diffusion of water under saturated humidity into a concentrated solution of BCP cast on a stationary substrate.[18]

Our previous studies suggested that the branched architecture of the hydrophilic block played a crucial role in the preferential self-assembly of branched-linear BCPs (Scheme 1) into inverse mesophases by affecting the chain dimension of the hydrophobic block with respect to the bilayer plane.[17] This altered chain dimension caused the critical packing parameter (P, defined as $P=V/a_0l_c$, in which V is the volume of the hydrophobic part, a_0 is the molecular area per amphiphile, and l_c is the critical length of the hydrophobic part) of the BCP to be greater than unity, which was presumed to be a qualitative prerequisite for inverse mesophase formation by self-assembly of BCPs and lipids in solution.[15,17]

In spite of this architectural effect on self-assembly, the block ratio (f_{PEG}, defined by the ratio of the molecular weight of the hydrophilic poly(ethylene glycol) (PEG) domain to that of the hydrophobic polystyrene (PS) chain) remained as a dominant factor governing the phase behavior of the BCP.[16,17] Therefore, the block ratio of the BCP should be carefully adjusted by using controlled radical polymerization of the hydrophobic PS block to restrict the molecular weight of the PS block to the narrow range required for the preferential self-assembly of the BCPs into inverse bicontinuous cubic mesophases. This stringent requirement of the architecture of branched-linear BCPs might hinder the availability of the resulting self-assembled structures for further studies and applications. Here we demonstrate that the phase of the self-assembled structures of a branched-linear BCP consisting of branched PEG and linear PS blocks can be controlled to favor the formation of inverse mesophases over conventional polymer vesicles by adjusting the composition of the solvent mixture.

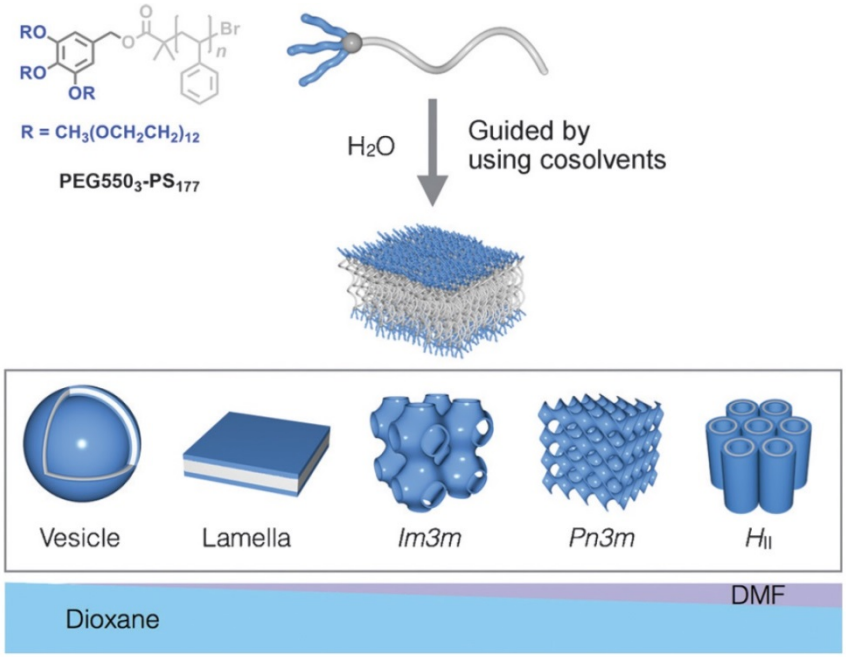

Scheme 4-1. A branched-linear block copolymer and its self-assembly into inverse mesophases with desired lattices guided by using cosolvents.

4.3 Results and discussion

Self-assembly of branched-linear block copolymers. In this study, we synthesized branched-linear BCPs (bPEG–PS_n; n = number of repeat units in the polystyrene chain) through atom-transfer radical polymerization (ATRP) of styrene in the presence of a macroinitiator, which has three PEG550 chains (M_n = 550 g mol^{-1}) tethered to a 3,4,5-trihydroxybenzyl ester core (Scheme 4-1). This method allowed to control the block ratio (f_{PEG}) by adjusting the molecular weight of the PS chain (Table 4-1).

Table 4-1. Characterization of $PEG550_3$-PSs

sample	M_n (g mol^{-1}) [a]	$Đ$ [a]	DP_n (PS) [b]	f_{PEG} (%) [c]	Phase [d]
$PEG550_3$-PS_{160}	16560	1.09	160	9.8	v
$PEG550_3$-PS_{167}	17060	1.09	167	9.5	v
$PEG550_3$-PS_{177}	17880	1.08	177	8.9	v
$PEG550_3$-PS_{200}	19760	1.07	200	7.9	c
$PEG550_3$-PS_{204}	19940	1.08	204	7.7	c
$PEG550_3$-PS_{211}	20830	1.08	211	7.5	c
$PEG550_3$-PS_{215}	21750	1.07	215	7.3	lc
$PEG550_3$-PS_{219}	22390	1.05	219	7.2	lc
$PEG550_3$-PS_{231}	22320	1.08	231	6.9	lc
$PEG550_3$-PS_{238}	24130	1.08	238	6.6	lc
$PEG550_3$-PS_{255}	25170	1.08	255	6.2	H
$PEG550_3$-PS_{283}	26370	1.08	283	5.6	H

[a] The number average molecular weight and molecular weight distribution determined by GPC (THF, 35 °C, 1 mL min^{-1} flow rate) using PS standards. [b] The number average degree of polymerization of PS block determined by ^{1}H NMR integration. [c] The molecular weight ratio of the PEG domain to that of the PS block (M_n(PEG) = 1650 g mol^{-1} for 550_3-PS_n). [d] Observed morphology of self-assembled structures of a suspension prepared from a dioxane solution of the BCP (0.5 wt. %). v: vesicle, c: cubosomes, lc: large cubosomes. H: hexasomes

The resulting bPEG–PS_n was allowed to self-assemble in solution by the cosolvent method involving the addition of a PEG-block-selective solvent (water) to a solution of BCPs dissolved in an organic solvent (0.5 wt% in dioxane) at a controlled rate. Under this condition, the f_{PEG} value of the BCP should be maintained at 6.5-8.5% for the preferential formation of inverse bicontinuous cubic mesophases (Figure 4-1a). As observed by small-angle X-ray scattering (SAXS) and electron microscopy, $PEG550_3$-PS_{211} (f_{PEG} = 7.5%) self-assembled into polymer cubosomes with an internal P minimal surface consisting of BCP bilayers (*Im3m* space group, lattice constant a = 82.5 nm; Figures 4-1b,c and 4-2a). On the other hand, bPEG–PS_n with a higher molecular-weight PS chain ($PEG550_3$-PS_{231}, f_{PEG} = 6.9%) self-assembled into large cubosomes (diameter >20 mm), exhibiting the D minimal

surface structure (*Pn3m* space group, a = 47.9 nm; Figures 4-1d,e and 4-2b). As shown in a simple phase diagram (Figure 4-1a), bPEG–PS_n only formed polymer vesicles (Figure 4-1f) when the value of f_{PEG} was greater than 8.9%, and bPEG–PS_n preferentially self-assembled into large hexasomes with an internal H_{II} phase if the f_{PEG} value was less than 5.6% (*P6mm*, a = 28.8 nm; Figures 4-1g and 4-2c). Even though controlled radical polymerization methods such as ATRP could provide accurate control over the molecular weight of the PS block and, thus, the f_{PEG} value of the bPEG–PS_n, the stringent block ratio requirement for the preferential self-assembly of BCP into inverse bicontinuous cubic phases imposed difficulty in synthesizing BCPs for the preparation of the polymer cubosomes and mesoporous films having well-defined internal bicontinuous structures.

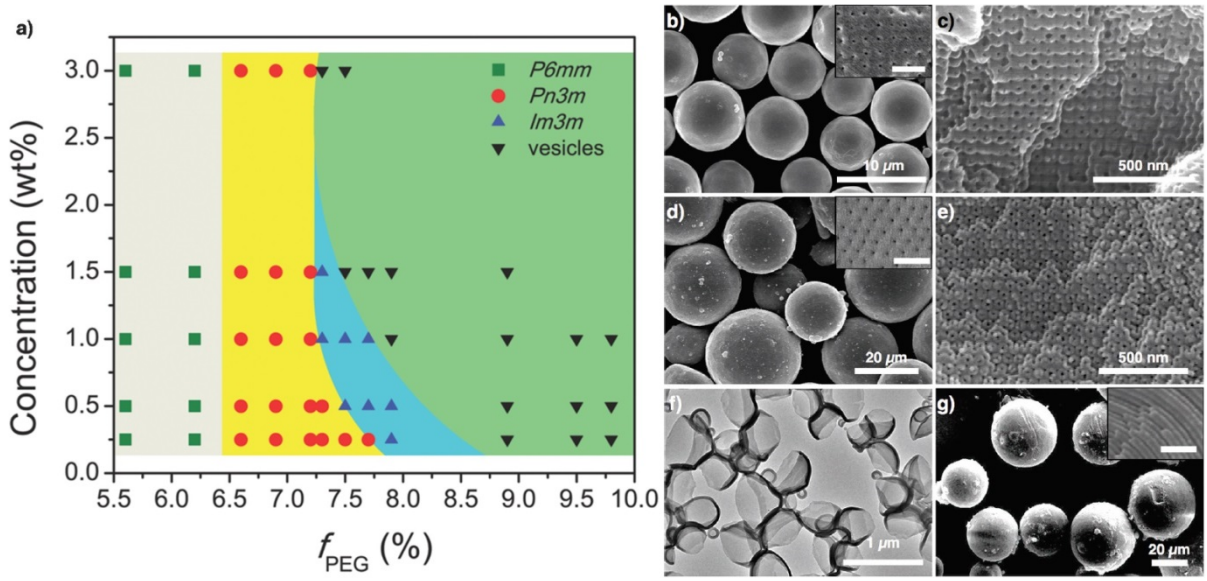

Figure 4-1. (a) A simple phase diagram of self-assembly of $PEG550_3$-PS_n from dioxane solutions. (b–e) SEM images of the polymer cubosomes of (b) $PEG550_3$-PS_{211} (f_{PEG} = 7.5%) and (d) $PEG550_3$-PS_{231} (f_{PEG} = 6.9 %). The insets show the perforated surface layer of the polymer cubosomes (scale bars, 200 nm). SEM images of the internal structures of the polymer cubosomes of (c) $PEG550_3$-PS_{211} showing [100] projection of *Im3m* and (e) $PEG550_3$-PS_{231} showing [111] projection of *Pn3m*. (f) TEM image of the polymersomes of $PEG550_3$-PS_{177} (f_{PEG} = 8.9 %). (g) SEM image of the hexasomes of $PEG550_3$-PS_{283} (f_{PEG} = 5.6 %). The inset shows the internal H_{II} structure (scale bar, 200 nm).

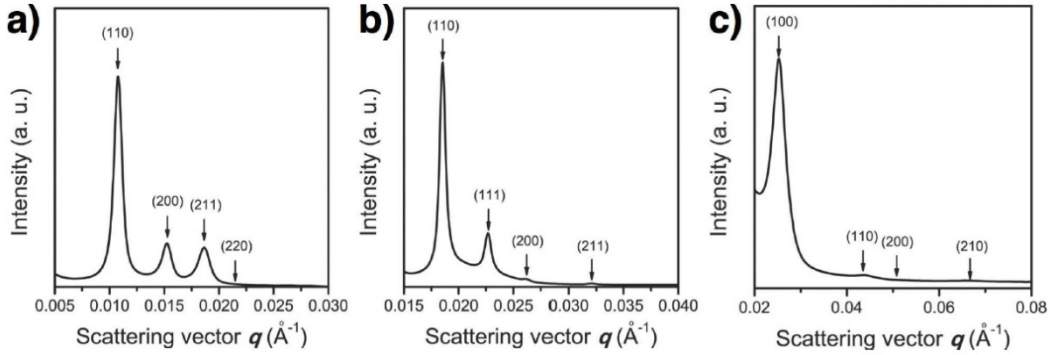

Figure 4-2. SAXS results of (a) $PEG550_3$-PS_{211} (*Im3m*, a = 82.5 nm), (b) $PEG550_3$-PS_{231} (*Pn3m*, a = 47.9 nm), and (c) $PEG550_3$-PS_{283} (H_{II}, a = 28.8 nm).

Morphological change of the self-assembled structures of bPEG-PS_n. Control over the thermodynamic parameters and kinetic pathways of the self-assembly of BCPs has been pursued as a means for influencing the self-assembly process to create nanostructures with desired morphologies without synthesizing new BCPs.[21–27] Controlling the solvent composition and thereby the affinity of the solvent toward the polymer chain is a facile method for controlling the conformation and properties of polymer chains in solution.[28,29] The solvent composition was simply adjusted by mixing solvents with different interaction parameters toward the target polymers. The solvent composition has already been shown to play an important role in determining the morphology of self-assembled block copolymer structures in solution. Cheng and co-workers demonstrated the morphological transition of the self-assembled structure of a single diblock copolymer in a binary mixture of solvents, ranging from spherical micelles to cylindrical micelles and vesicles, depending on the composition of the solvent.[23] The Eisenberg group also showed that the size of polymersomes could be reversibly adjusted using a binary solvent mixture of varying ratio.[25,26] Recently, Truong et al. reported that a single BCP, consisting of a cationic hydrophilic block and a glassy PS block, could reproducibly exhibit different morphologies, depending on the nature of the solvent and the kinetic conditions of the self-assembly process.[27]

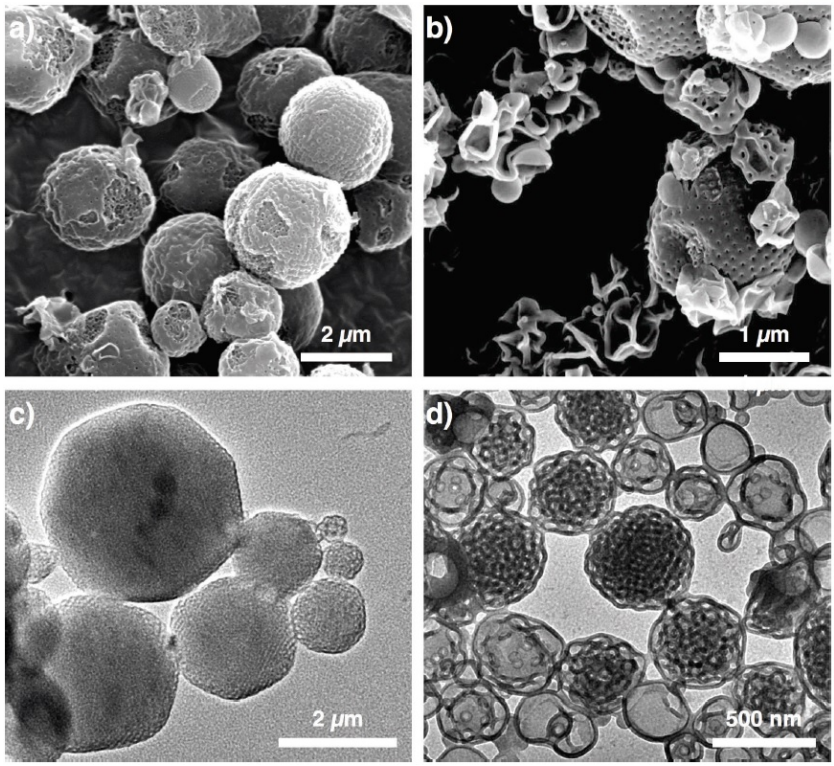

Figure 4-3. SEM and TEM images of self-assembled structures of $PEG550_3$-PS_{211} by using THF as a common solvent. (a and c) Fully developed polymer cubosomes as a majority. (b and d) Polymersomes and sponge phase particles as minor structures.

Inspired by these previous studies, we postulated that the composition of the solvent could affect the chain dimension of the hydrophobic PS block, which might result in a morphological change of the self-assembled inverse structures of bPEG–PS_n. Using dioxane (with the Hildebrand solubility parameter δ = 20.5 $MPa^{-1/2}$)[30] as a common solvent for both PEG and PS domains, $PEG550_3$-PS_{211} preferentially formed polymer cubosomes under our standard conditions for self-assembly. When tetrahydrofuran (THF; δ = 18.6 $MPa^{-1/2}$) was used as a solvent, the transmission electron microscopy (TEM) images of the self-assembled structures of $PEG550_3$-PS_{211} showed the appearance of polymer vesicles and sponge phase particles as minor structures along with a majority of fully developed polymer cubosomes (Figure 4-3). Dimethylformamide (DMF) is a pseudo-theta solvent for PS, in which PS adopts a reduced chain dimension such as R_g compared to the value of the same PS chain dissolved in dioxane.[31,32] When DMF (δ = 24.7 $MPa^{-1/2}$) was used as a common solvent, $PEG550_3$-PS_{211} only forms irregular aggregates without any internal order at a low water content (>3%). From these observations, we suspected that the affinity of the solvent toward the PS block (δ = 16.6–20.2 $MPa^{-1/2}$) might have an influence on the compatibility of the PS chain in solution, which could, in turn, affect the chain stretching of the PS block when the BCP forms aggregates.

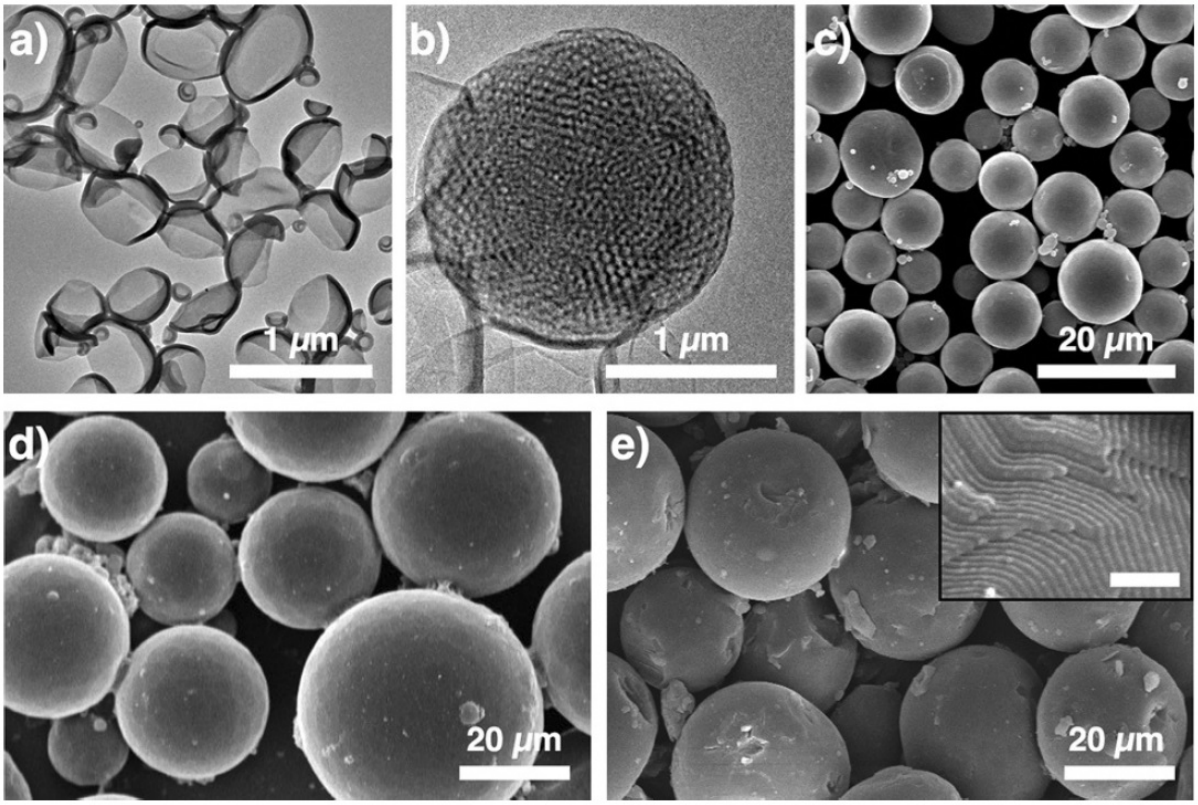

Figure 4-4. (a–e) TEM and SEM images of the self-assembled structures of PEG550$_3$-PS$_{177}$ prepared from the dioxane/DMF mixtures at varying ratios: (a) 0 vol% DMF (vesicle), (b) 2 vol% DMF (vesicles, polymer cubosomes), (c) 5 vol% DMF (*Im3m* + *Pn3m*), (d) 8 vol% DMF (*Pn3m*), and (e) 15 vol% DMF (H_{II}). The inset in (e) shows the internal hexagonal structures (scale bar, 200 nm).

To support this assumption, we changed the solvent composition of the initial BCP solution by mixing dioxane with DMF. We tested PEG550$_3$-PS$_{177}$ (f_{PEG} =8.9%), which, under our standard conditions for self-assembly, only formed polymersomes when THF or dioxane was used as the only solvent (Figure 4-4a). However, when the solvent was changed to a dioxane/DMF mixture (98:2 v/v), PEG550$_3$-PS$_{177}$ self-assembled into the inverse mesophase structure, forming small polymer cubosomes coexisting with polymer vesicles (Figure 4-4b). When we increased the DMF content in dioxane to 5 vol%, we observed the formation of polymer cubosomes (average diameter of 8 μm) without the coexistence of polymer vesicles (Figure 4-4c). Further increasing the amount of DMF in dioxane (dioxane/DMF = 92:8 v/v) only increased the average diameter (26 μm) of the polymer cubosomes of PEG550$_3$-PS$_{177}$ (Figure 2d). Essentially, the self-assembled structure of PEG550$_3$-PS$_{177}$ was transformed into large hexasomes with an internal inverse hexagonal phase (H_{II}) when the solvent mixture had a high DMF content (dioxane/DMF = 85:15 v/v). This morphological transition exhibited by self-assembly of PEG550$_3$-PS$_{177}$ in a series of solvent mixtures coincided with the transition of the self-assembled structures of PEG550$_3$-PS$_n$ with an increasing degree of polymerization of the PS

block (Figure 4-1). We also note that the self-assembly of a linear BCP, PEG2000-PS_{180}, did not show any phase transition under the identical conditions used for the self-assembly of $PEG550_3$-PS_{177} (Figure 4-5), suggesting that the architecture of bPEG–PS_n is responsible for the self-assembly into inverse mesophases.

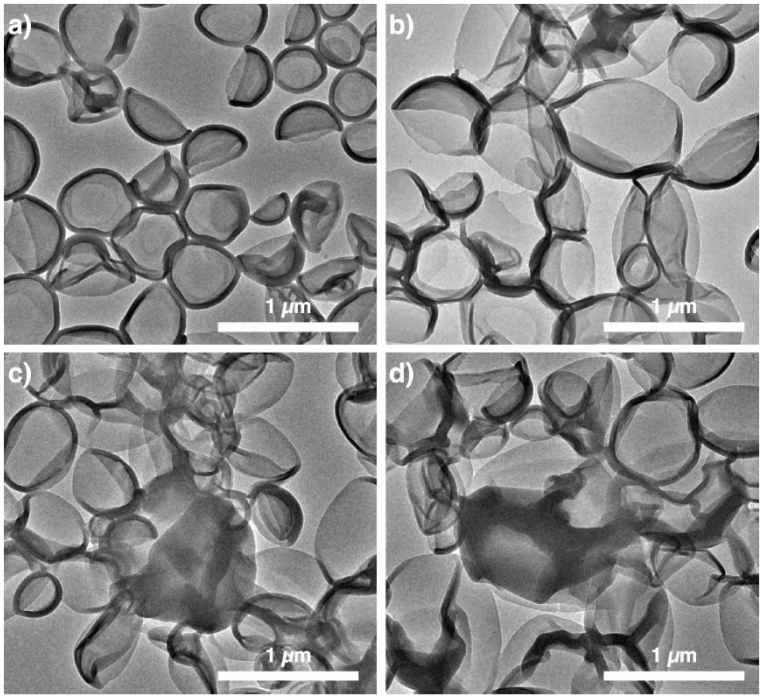

Figure 4-5. TEM images of self-assembled structures of PEG2000-PS_{180} in various mixtures of dioxane and DMF: (a) 0 vol% DMF, (b) 2 vol% DMF. (c) 5 vol% DMF, and (d) 8 vol% DMF.

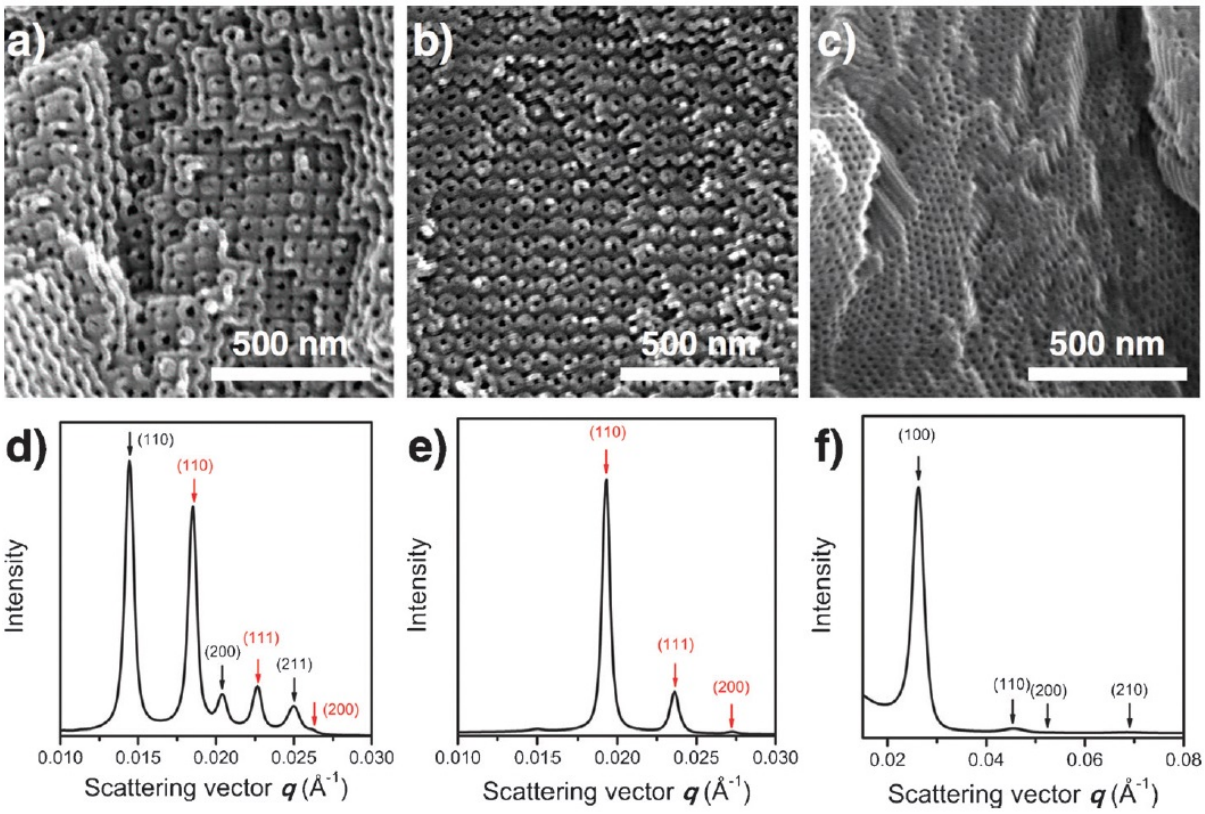

Figure 4-6. (a–c) SEM images of the internal structures of the polymer cubosomes of $PEG550_3$-PS_{177} prepared from (a) 5 vol% DMF in dioxane showing the [100] projection of *Im3m*, (b) 8 vol% DMF in dioxane showing the [111] projection of *Pn3m*, and (c) 15 vol% DMF in dioxane showing the cross-section view of the inverse hexagonal phase. (d–f) SAXS results corresponding to the polymer cubosomes in (a–c): (d) Mixed phase of *Im3m* and *Pn3m* symmetries (a = 61.5 nm (*Im3m*) and 48.0 nm (*Pn3m*)); (e) *Pn3m* symmetry (a = 46.0 nm); (f) *P6mm* (H_{II}) symmetry (a=27.7 nm).

The internal crystalline structure of the polymer cubosomes of $PEG550_3$-PS_{177} prepared from the binary mixture of dioxane and DMF as a solvent for self-assembly was studied by SAXS and SEM (Figure 4-6). From the SAXS results, we observed that the internal crystalline structure of the polymer cubosomes of $PEG550_3$-PS_{177} self-assembled from the mixed solvent with 5 vol% DMF in dioxane was a mixed phase of Schwartz P and Schwartz D surfaces (*Im3m* + *Pn3m*) (Figure 4-6a,d). Upon increasing the amount of DMF in the solvent mixture (dioxane/DMF = 92:8 v/v), the internal structure was completely changed to the Schwartz D surface (*Pn3m* symmetry, a = 46.0 nm; Figure 4-6b,e). The inverse hexagonal phase (H_{II}) appeared within the large particles when $PEG550_3$-PS_{177} was self-assembled from a solvent mixture with a higher DMF content (dioxane/DMF = 85:15 v/v; Figure 4-6c,f). This result corresponds with the phase behavior of $PEG550_3$-PSn upon increasing the degree of polymerization (DP_n) of the PS block, leading to the phase change of the self-assembled structures from polymersomes to polymer cubosomes and hexasomes.[17] Given the fixed molecular weight of

both polymer blocks in $PEG550_3$-PS_{177}, the addition of DMF might affect the chain dimension of the PS block in a binary mixture of common solvents. If a constant PS block volume is assumed, the chain stretching of the PS block would decrease in the presence of DMF, which could reduce the critical chain length of the hydrophobic domain (l_c) and, thus, would increase the critical packing factor (P) of the BCP upon self-assembly.

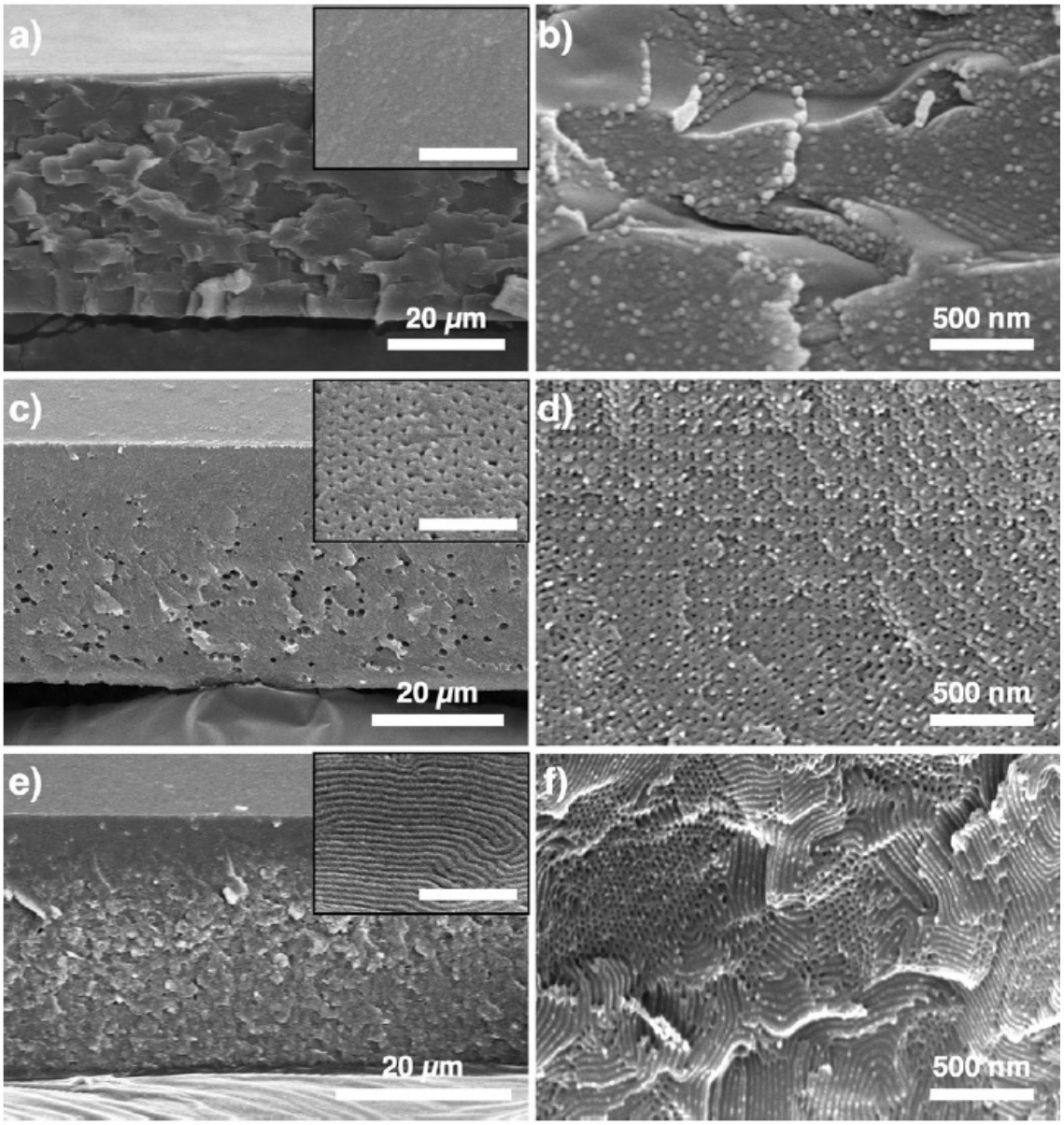

Figure 4-7. (a, c, e) Low-resolution SEM images of the cross-section of the mesoporous films of $PEG550_3$-PS_{177} prepared by the SDEMS method using DMF/dioxane mixtures as a common solvent. (a) 0 vol% DMF, (c) 10 vol% DMF, and (e) 15 vol% DMF. (The insets show the top layer of the films; scale bars, 500 nm). (b, d, f) High-resolution SEM images of the films of (a), (c), and (e). (b) Stacked lamellae, (d) *Pn3m* symmetry (a=50.6 nm), and (f) *P6mm* symmetry (a=29.3 nm).

Similar effects of the presence of DMF in the solvent mixture were also observed in the self-assembly of $PEG550_3$-PS_{177} mediated by the diffusion of water vapor into the BCP solution cast on a stationary substrate.[18] This method, the solvent-diffusion/evaporation-mediated self-assembly (SDEMS) of BCPs, allowed the solution self-assembly of bPEG-PS_n on a stationary substrate under static conditions. The dioxane solution of $PEG550_3$-PS_{177} (15 wt%) cast on a glass substrate (1 cm^2 area) only turned into a translucent film (thickness of 50 μm) consisting of stacked lamellae of BCP upon the diffusion of water in the humidity chamber (saturated with water/dioxane 1:1 v/v) for 1 h at 23 °C (Figure 4-7a,b). When a dioxane/DMF mixture (90:10 v/v) was used as solvent for $PEG550_3$-PS_{177}, the same procedure yielded a mesoporous film with an internal D minimal surface structure (*Pn3m*, a = 50.6 nm) throughout the film (Figures 4-7c,d and 4-8). The internal structure of the film changed to the inverse hexagonal phase (H_{II}) when the DMF content was increased (dioxane/DMF 85:15 v/v) (Figure 4-7e,f).

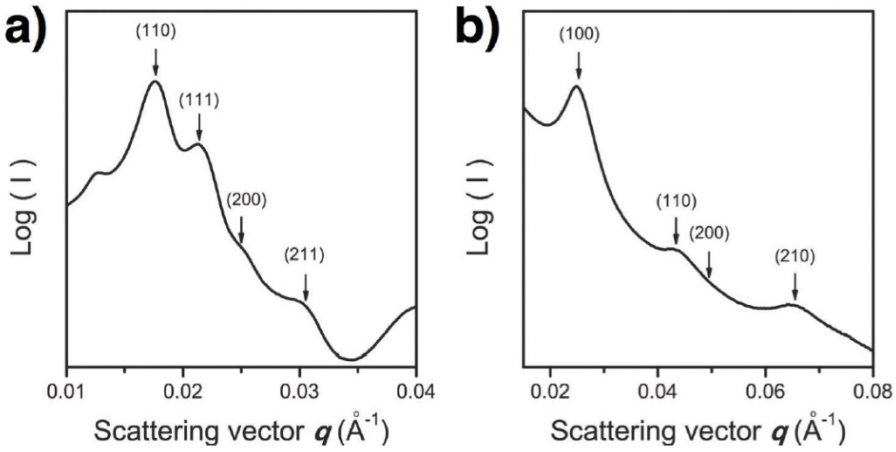

Figure 4-8. SAXS results of the mesoporous monoliths of $PEG550_3$-PS_{177} prepared by the SDEMS method from (a) 10 vol% DMF in dioxane (*Pn3m*, a = 50.6 nm), and (b) 15 vol% DMF in dioxane (*P6mm*, a = 29.3 nm).

4.4 Summary

In summary, we demonstrated that the solution self-assembly of a branched-linear BCP, namely $PEG550_3$-PS_{177}, could be controlled to favor the formation of inverse mesophases over conventional polymer vesicles by adjusting the solvent composition. By gradually deteriorating the solvent affinity toward the PS block by mixing two solvents with different interaction parameters, the resulting self-assembled structures of a single branched-linear BCP exhibit a morphological transition from vesicles and flat bilayers to triply periodic minimal surfaces of the block copolymer bilayer as well as inverse hexagonal structures. The crystalline lattice of the TPMSs of the BCPs could also be changed from the primitive cubic structure to double diamond structures depending on the composition of the

common solvent mixture. This nonsynthetic pathway for accessing the desired inverse mesophases of a single BCP could expand the availability of well-defined mesoporous structures of BCPs for applications such as separation and nanotemplating by providing block ratio tolerance for BCP synthesis.

4.5 Experimental

General methods and materials. Unless otherwise noted, all reagents and chemicals were used as received from Sigma Aldrich and TCI. DMF was dried over CaH_2 under N_2 and freshly distilled prior to use. Tetrahydrofuran (THF) was refluxed over a mixture of Na and benzophenone under N_2 and distilled before use. All reactions were performed under N_2 unless otherwise noted. ^1H and ^{13}C NMR spectra were recorded on a Varian VNMRS 600 spectrometer, using CD_2Cl_2 and $CDCl_3$ as solvents. Matrix-assisted laser desorption ionization time-of-flight mass spectroscopy (MALDI-TOF-MS) was performed on a Bruker Ultraflex III TOF-TOF mass spectrometer equipped with a nitrogen laser (335 nm). Scanning electron microscopy (SEM) was performed on a FEI Nova NanoSEM 230 microscope and Hitachi S-4800 FE SEM at an acceleration voltage of 10 kV. The samples were placed on a conductive carbon tape and then coated with Pt with a thickness of 3 nm by using a K575X Sputter Coater. Transmission electron microscopy (TEM) was recorded on a JEOL JEM-2100 microscope at 200 kV. Specimens were prepared by placing a drop of the solution on a carbon-coated Cu grid (200 mesh, EM science). After 30 min, remaining solution on a grid was removed with a filter paper, and the grid was air-dried overnight. Synchrotron small angle X-ray scattering data were obtained on PLSII 9A at Pohang acceleration laboratory (Pohang, Korea).

Synthesis of branched macroinitiator with peripheral PEG chains

Branched macroinitiators were synthesized in multi-gram quantity by following the literature methods.[17]

550_3-Br. ^1H NMR (δ=ppm, 600 MHz, $CDCl_3$) 6.60 (s, 2H), 5.10 (s, 2H), 4.16 (t, 4H, J = 4.8Hz), 4.13 (t, 2H, J = 4.8Hz), 3.86-3.50 (m, -CH_2CH_2O-), 3.39 (m, 9H), 1.95 (s, 6H). ^{13}C NMR (δ=ppm, 150 MHz, $CDCl_3$) 171.2, 152.6, 140.1, 130.8, 107.4, 77.4, 77.1, 76.7, 70.8-70.3, 69.6, 69.6, 68.8, 67.4, 59.0, 55.8, 30.7. M_n (GPC) = 2250 g mol^{-1}, PDI = 1.03, M_n (MALDI-TOF) = 2158 g mol^{-1}.

Synthesis of block copolymers (550_3-PS_n).

CuBr (50 mg, 0.35 mmol) and *N,N,N',N'',N''*-pentamethyldiethylenetriamine (PMDETA) (108 mg, 0.525 mmol) were mixed with 1 mL of anisole in a 20 mL Schlenk tube with a magnetic bar. The tube was sealed with a rubber septum. This mixture was bubbled with N_2 for 15 min with gentle stirring. To this solution, the solution of styrene (10 mL) and 550_3-Br (120 mg, 0.035 mmol) was added via a

syringe. The green solution was degassed by bubbling N_2 for 20 min. After degassing, the tube was immersed in a preheated oil bath (95 °C) and the polymerization was proceed at this temperature. The progress of polymerization was monitored by taking GPC at an interval of 1 h. When the molecular weight of the block copolymer reached to the desired value, the reaction was quenched by exposing the solution to air in an ice/water bath and diluted with $CHCl_3$ (15 mL). The cooled solution was filtered through a pack of aluminum oxide (basic) with $CHCl_3$ to remove the Cu catalyst. The filtered solution was concentrated on a rotary evaporator, and the resulting residue was diluted with 20 mL CH_2Cl_2. This solution was precipitated into methanol (200 mL). White powder was collected by vacuum filtration and dried in vacuo. All block copolymers were characterized by ^{1}H NMR and GPC to evaluate the molecular weight and the size distribution. The molecular characteristics of the block copolymers are listed in Table 4-1.

General procedure for self-assembly of 550_3-PSs into polymer cubosomes. The bPEG-PS was initially dissolved in 2 mL of a 1,4-dioxane/DMF mixture in a capped vial, and the solution was stirred for 3 h at room temperature. Water (total 2 mL) was added at a controlled rate (1 mL h^{-1}) to the solution with vigorous stirring (850 rpm). The resulting milky suspension was dialyzed (molecular weight cutoff (MWCO) = ~12-14 kDa, SpectraPor) against water for 24 h to remove the organic solvent.

Preparation of mesoporous films of 550_3-PS$_n$. 550_3-PS_{177} (15 wt%) was dissolved in a 1,4-dioxane/DMF mixture (90:10 v/v) in a 15-mL vial, and the resulting solution was kept at room temperature for 1 h before the use. A sealed humidity chamber was prepared by mixing 35 mL of 1,4-dioxane and 35 mL of water in a 100-ml vial, and then a cylindrical column to put a glass substrate was carefully added. A desired amount of the solution of 550_3-PS_{177} was carefully cast on the glass slide, which was rapidly placed on the column in the humidity chamber. The humidity chamber was then sealed for 1 h at 23 °C. After completing self-assembly, the glass slide covered with the film of 550_3-PS_{177} was immersed into excess water to quench the assembly process by vitrification of the PS block. The opaque film was then obtained after removing 1,4-dioxane by solvent exchange in water.

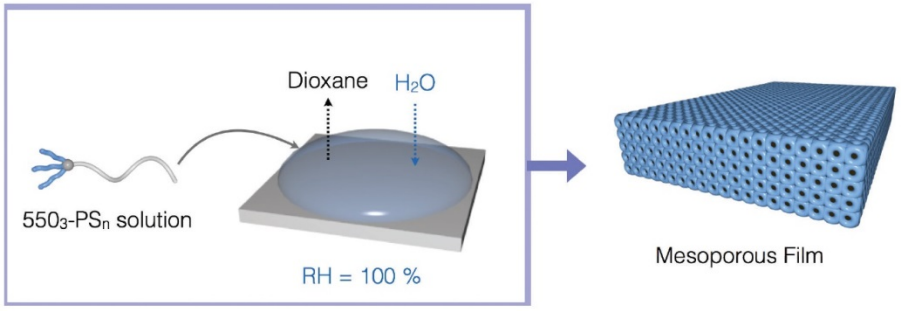

Figure 4-9. Schematic illustration for preparation of the mesoporous film of PEG550_3-PS$_n$.

4.6 References

1. McKenzie, B. E.; Holder, S. J.; Sommerdijk, N. A. J. M. Assessing Internal structure of Polymer Assemblies from 2D to 3D Cryo TEM: Bicontinuous Micelles. *Curr. Opin. Colloid Interface Sci.* **2012**, *17*, 343–349.
2. Denkova, A. G.; Bomans, P. H. H.; Coppens, M.-O.; Sommerdijk, N. A. J. M. Complex Morphologids of Self-Assembled Block Copolymer Micelles in Binary Solvent Mixtures: the Role of Solvent-Solvent Correlations. *Soft Matter* **2011**, *7*, 6622–6628.
3. McKenzie, B. E.; Nudelman, F.; Bomans, P. H. H.; Holder, S. J.; Sommerdijk, N. A. J. M. Temperature-Responsive Nanospheres with Bicontinuous Internal Structures from a Semicrystalline Amphiphilic Block Copolymer. *J. Am. Chem. Soc.* **2010**, *132*, 10256–10259.
4. McKenzie, B. E.; Friedrich, H.; Wirix, M. J. M.; de Visser, J.; Monaghan, O. R.; Bomans, P. H. H.; Nudelman, F.; Holder, S. J.; Sommerdijk, N. A. J. M. Controlling Internal Pore Sizes in Bicontinuous Polymeric Nanospheres. *Angew. Chem. Int. Ed.* **2015**, *54*, 2457–2461; *Angew. Chem.* **2015**, *127*, 2487–2491.
5. McKenzie, B. E.; de Visser, J. F.; Friedrich, H.; Wirix, M. J. M.; Bomans, P. H. H.; deWith, G.; Holder, S. J.; Sommerdijk, N. A. J. M. Bicontinuous Nanospheres from Simple Amorphous Amphiphilic Diblock Copolymers. *Macromolecules* **2013**, *46*, 9845–9848.
6. Holder, S. J.; Woodward, G.; McKenzie, B. E.; Sommerdijk, N. A. J. M. Semi-Crystalline Block Copolymer Bicontinuous Nanospheres for Thermoresponsive Controlled Release. *RSC Adv.* **2014**, *4*, 26354–26358.
7. Parry, A. L.; Bomans, P. H. H.; Holder, S. J.; Sommerdijk, N. A. J. M.; Biagini, S. C. G. Cryo Electron Tomography Reveals Confined Complex Morphologies of Tripeptide-Containing Amphiphilic Double-Comb Diblock Copolymers. *Angew. Chem. Int. Ed.* **2008**, *47*, 8859–8862; *Angew. Chem.* **2008**, *120*, 8991–8994.
8. Hales, K.; Chen, Z.; Wooley, K. L.; Pochan, D. J. Nanoparticles with Tunable Internal Structure from Triblock Copolymers of PAA-*b*-PMA-*b*-PS *Nano Lett.* **2008**, *8*, 2023–2026.
9. Zhang, L.; Bartels, C.; Yu, Y.; Shen, H.; Eisenberg, A. Mesosized Crystal-like Structure of Hexagonally Packed Hollow Hoops by Solution Self-Assembly of Diblock Copolymers. *Phys. Rev. Lett.* **1997**, *79*, 5034–5037.
10. Larsson, K.; Fredrik, T. Periodic Minimal Surface Structures in Bicontinuous Lipid-Water Phases and Nanoparticles. *Curr. Opin. Colloid Interface Sci.* **2005**, *9*, 365–369.
11. Larsson, K. Two Cubic Phases in Monoolein-Water System. *Nature* **1983**, *304*, 664.
12. Barauskas, J.; Johnsson, M.; Joabsson, F.; Tiberg, F. Cubic Phase Nanoparticles (Cubosome): Principles for Controlling Size, Structure, and Stability. *Langmuir* **2005**, *21*, 2569–2577.
13. Spicer, P. T. Progress in Liquid Crystalline Dispersions: Cubosomes. *Curr. Opin. Colloid Interface Sci.* **2005**, *10*, 274–279.

14. Gustafsson, J.; Ljusberg-Wahren, H.; Almgren, M.; Larsson, K. Cubic Lipid-Water Phase Dispersed into Submicron Particles. *Langmuir* **1996**, *12*, 4611–4613.
15. Kulkarni, C. V.; Wachter, W.; Iglesias-Salto, G.; Engelskirchen, S.; Ahualli, S. Monoolein: a Magic Lipid? *Phys. Chem. Chem. Phys.* **2011**, *13*, 3004–3021.
16. La, Y.; Park, C.; Shin, T. J.; Joo, S. H.; Kang, S.; Kim, K. T. Colloidal Inverse Bicontinuous Cubic Membranes of Block Copolymers with Tunable Surface Functional Groups. *Nat. Chem*. **2014**, *6*, 534–541.
17. An, T. H.; La, Y.; Cho, A.; Jeong, M. G.; Shin, T. J.; Park, C.; Kim, K. T. Solution Self-Assembly of Block Copolymers Containing a Branched Hydrophilic Block into Inverse Bicontinuous Cubic Mesophases. *ACS Nano* **2015**, *9*, 3084–3096.
18. Park, C.; La, Y.; An, T. H.; Jeong, H. Y.; Kang, S.; Joo, S. H.; Ahn, H.; Shin, T. J.; Kim, K. T. Mesoporous Monoliths of Inverse Bicontinuous Cubic Phases of Block Copolymer Bilayers. *Nat. Commun.* **2015**, *6*, 6392.
19. Yu, H.; Qiu, X.; Nunes, S. P.; Peinemann, K.-V. Biomimetic Block Copolymer Particles with Gated Nanopores and Ultrahigh Protein Soption Capacity. *Nat. Commun.* **2014**, *5*, 4110.
20. Kulkarni, C. V.; Tang, T.-Y.; Seddon, A. M.; Seddon, J. M.; Cesa, O.; Templer, R. H. Engineering Bicontinuous Cubic Structures at the Nanoscale-the Role of Chain Splay. *Soft Matter* **2010**, *6*, 3191–3194.
21. Hayward, R. C.; Pochan, D. J. Tailored Assemblies of Block Copolymers in Solution: It Is All about the Process. *Macromolecules* **2010**, *43*, 3577–3584.
22. Cui, H.; Chen, Z.; Zhong, S.; Wooley, K. L.; Pochan, D. J. Block Copolymer Assembly via Kinetic Control. *Science* **2007**, *317*, 647 –650.
23. Bhargava, P.; Zheng, J. X.; Li, P.; Quirk, B. P.; Harris, F. W.; Cheng, S. Z. D. Self-Assembled Polystyrene-block-poly(ethylene oxide) Micelle Morphologies in Solution. *Macromolecules* **2006**, *39*, 4880–4888.
24. Yu, Y.; Zhang, L.; Eisenberg, A. Morphogenic Effect of Solvent on Crew-Cut Aggregates of Amphiphilic Diblock Copolymers. *Macromolecules* **1998**, *31*, 1144–1154.
25. Luo, L.; Eisenberg, A. Thermodynamic Size Control of Block Copolymer Vesicles in Solution. *Langmuir* **2001**, *17*, 6804–6811.
26. Choucair, A.; Lavigueur, C.; Eisenberg, A. Polysyrene-*b*-poly(acrylic acid) Vesilcle Size Control Using Solution Properties and Hydrophilic Block Length. *Langmuir* **2004**, *20*, 3894–3900.
27. Truong, N. P.; Quinn, J. F.; Dussert, M. V.; Sousa, N. B. T.; Whittaker, M. R.; Davis, T. P. Reproducible Access to Tunable Morphologies via the Self-Assembly of an Amphiphilic Diblock Copolymer in Water. *ACS Macro Lett.* **2015**, *4*, 381–386.
28. [28] Yu, Y.; Kieviet, B. D.; Kutnyanszky, E.; Vancso, G. J.; de Beer, S. Cosolvency-Induced

Switching of the Adhesion between Poly(methyl methacrylate) Brushes. *ACS Macro Lett.* **2015**, *4*, 75–79.

29. Van Franeker, J. J.; Turbiez, M.; Li, W.; Wienk, M. M.; Janssen, R. A. J. A Real-Time Study of the Benefits of Cosolvents in Polymer Solar Cell Processing. *Nat. Commun.* **2015**, *6*, 6229.
30. J. Brandrup, E. H. Immergut, Polymer Handbook, 3rd ed., Wiley, New York, 1989.
31. Terao, K.; Mays, J. W. On-line Measurement of Molecular Weight and Radius of Gyration of Polystyrene in a Good Solvent and in a Theta Solvent Measured with a Two-Angle Light Scattering Detector. *Eur. Polym. J.* **2004**, *40*, 1623–1627.
32. Zhou, J.; van Duijneveldt, J. S.; Vincent, B. The Phase Behavior of Dispersions of Silica Particles in Mixtures of Polystyrene and Dimethylformamide. *Langmuir* **2010**, *26*, 9397–9402.

Chapter 5. Polymer cubosomes-templated synthesis of cubic crystalline single networks

5.1 Abstract

Triply periodic materials having open-space mesoscale lattices, in particular, a single diamond lattice, have been pursued as ideal photonic crystals exhibiting large omnidirectional optical bandgaps. Such structures are ubiquitously found from biophotonic crystals of the wing scales of butterflies and the exoskeleton of beetles. Their biogenesis involves a selective diffusion of chitin into one of two identical water-channel networks embedded within ordered cellular membranes adopting bicontinuous cubic mesophases. In contrast, the artificial synthesis of single cubic frameworks has been a significant challenge due to the inability to distinguish degenerate channel networks within the bicontinuous cubic porous templates. Here we show that the interfacial topology of polymer cubosomes, finite-sized particles composed of bicontinuous cubic mesophases of block polymer bilayers, render one of two non-intersecting pore networks to be inaccessible to diffusion. This topological feature of bicontinuous cubic mesophases forces the external guests to enter only into the open cubic channel network within the polymer cubosomes. Consequently, single framework structures of diamond and primitive cubic lattices are synthesized by cross-linking of molecular precursors. Because of their topological and crystallographic similarities with ordered biological membranes, polymer cubosomes serve as the templates for the bio-inspired synthesis of single network cubic structures of diverse materials, which could lead to the creation of photonic crystals and metamaterials that are previously unavailable.

5.2 Introduction

Achieving low-coordinate cubic crystalline arrangements of nanostructures has been a prime target for the creation of metamaterials and photonic crystals due to their unique optical properties such as refractive index modulation and large photonic bandgap.[1,2] In particular, the single diamond network structure (*Fd3m* space group) is expected to be a 'champion' photonic structure as this symmetry is predicted to provide largest complete photonic bandgap in all directions.[3,4] However, self-assembly of colloidal particles into non-close packed cubic lattices having lattice dimensions commensurate with visible wavelengths is thermodynamically unfavorable unless the assembly process is carefully designed to guide the colloidal components to form weakly coordinated lattices using strong inter-particle interactions and additional components to stabilize the lattice.[5–7] The use of ordered porous materials as sacrificial templates could be a facile pathway to synthesize cubic crystalline network structures of desired lattice and periodicity.[8,9] However, bicontinuous mesophases of molecular building blocks such as surfactants and block copolymers (BCPs) template the formation of double

network structures, of which the increased symmetry hamper the modulation of the property of propagating electromagnetic waves.[1,2,8] Although single gyroid networks have been prepared by using selectively etched double gyroid phases of BCPs as templates,[8,9] single network structures of a diamond and primitive cubic lattice remain unavailable by simple templated syntheses.

In contrast, single network structures of diverse lattices and periodicities are ubiquitously found from the biophotonic structures of butterfly wing scales and exoskeletons of beetles.[10–12] The biogenesis of these single network cubic structures utilizes the ordered smooth endoplasmic reticulum (OSER) of the epithelial cell as the template for polymerization of chitin.[11] The OSER adopts inverse bicontinuous cubic mesophases having identical crystallographic symmetries to those of lipid bilayers in vivo and vitro.[13,14] Lipid cubic mesophases could be described as triply periodic minimal surfaces (TPMS) consisting of lipid bilayers, in which two non-intersecting water channel networks are embedded in a bicontinuous cubic crystalline order.[15,16] Recent studies of the structural details of lipid cubic mesophases and their colloidally stabilized particles (cubosomes),[17] by using calculations, atomic force microscopy (AFM) and cryo-electron tomography (CET), suggested that the topology of the cubic mesophases of lipid bilayers close one of the two non-intersecting channel networks to form an interface with water, leaving the other channel network fully exposed to the surrounding.[18–20] We postulated that this topological distinction at the interface of the lipid cubic mesophases could be a reason for the preferential diffusion of chitin only to the open channel network from the extracellular matrix, resulting in the formation of a single cubic network.

We imagined that the topological resemblance at the interface should arise between lipid cubosomes and polymer cubosomes, colloidal particles composed of well-defined inverse bicontinuous cubic mesophases of BCP bilayers, resulting in the preferential diffusion of cross-linkable precursors into only one of two single diamond or simple cubic channel networks embedded in the polymer cubic mesophases. Polymer cubosomes are structurally more robust than lipidic analogues, and their periodicities and pore sizes are proportionally increased to the molecular weights of the polymer blocks constituting the block copolymers.[21–23] Therefore, polymer cubosomes could serve as ideal templates for the synthesis of single diamond and simple cubic networks composed of diverse materials, of which the synthesis would phenomenologically resemble the biogenesis of photonic network structures.[24]

5.3 Results and discussion

In order to test our assumption, we investigated the structural details of the polymer cubosomes formed by the solution self-assembly of the branched-linear diblock copolymers composed of a hydrophilic tri-arm branched poly(ethylene glycol) and a hydrophobic polystyrene, $PEG550_3$-PS_n (n refers to the number average degree of polymerization of the PS).[22] In this study, we chose the polymer cubosomes of $PEG550_3$-PS_{150} (number average molecular weight (M_n) = 15,960 Da,

polydispersity index ($Đ$) = 1.04, f_{PEG} = 10.6%) and PEG550$_3$-PS$_{168}$ (M_n = 17820 Da, $Đ$ = 1.06, f_{PEG} = 9.4%), which represent two distinct lattice symmetries of the cubic mesophases. Small angle X-ray scattering (SAXS) results and scanning electron microscopy (SEM) images of the polymer cubosomes of PEG550$_3$-PS$_{150}$ confirmed that the internal bicontinuous cubic structure of the BCP bilayer had a symmetry of the Schwarz P surface (*Im3m* space group) with the lattice parameter (a) of 60.7 nm. The internal cubic mesophase of the polymer cubosomes of PEG550$_3$-PS$_{168}$ was assigned to the symmetry of the Schwarz D surface of the BCP bilayers (*Pn3m* space group, a = 45.2 nm) (Figure 5-1). From the SAXS results, we inferred the size of internal crystalline domains of polymer cubosomes from the scattering correlation length, $\xi \approx 2\pi/\Delta q$, where Δq is the full-width at half maximum of the first diffraction peak.[25] The crystallite size inside the polymer cubosomes was 673 nm for the internal P surface of PEG550$_3$-PS$_{145}$ (Δq = 9.34×10^{-4} Å^{-1}) and 833 nm for the D surface of PEG550$_3$-PS$_{168}$ (Δq = 7.54×10^{-4} Å^{-1}). Considering their diameter (5~20 μm), estimated by SEM images, the internal bicontinuous phases of the polymer cubosomes were composed of multiple crystalline domains, which was corroborated by the SEM images of fractured polymer cubosomes (Figure 5-2).

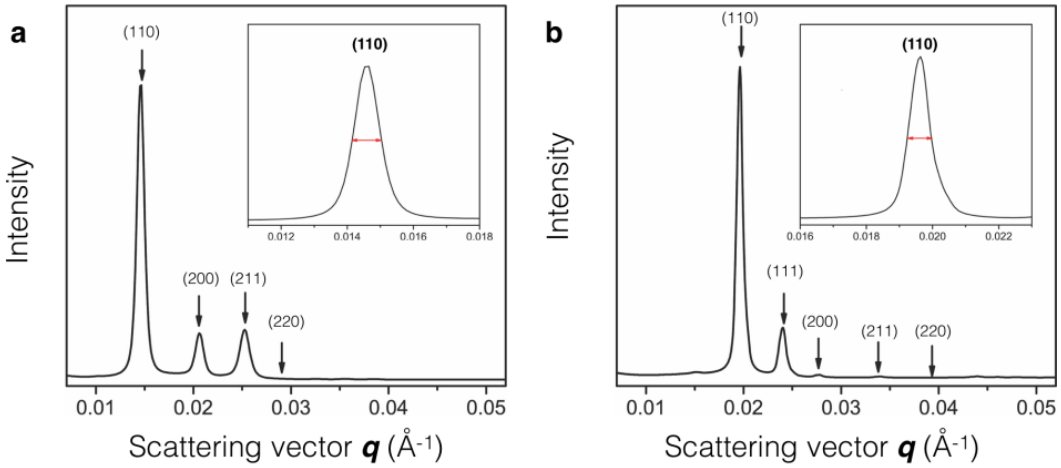

Figure 5-1. SAXS results of the polymer cubosomes of (a) PEG550$_3$-PS$_{150}$ (*Im3m*, a = 60.7 nm) and (b) PEG550$_3$-PS$_{168}$ (*Pn3m*, a = 45.2 nm). The insets show first diffraction peak position of *Im3m* and *Pn3m*. Double headed arrows indicate the full width at half-maximum of the peak (Δq).

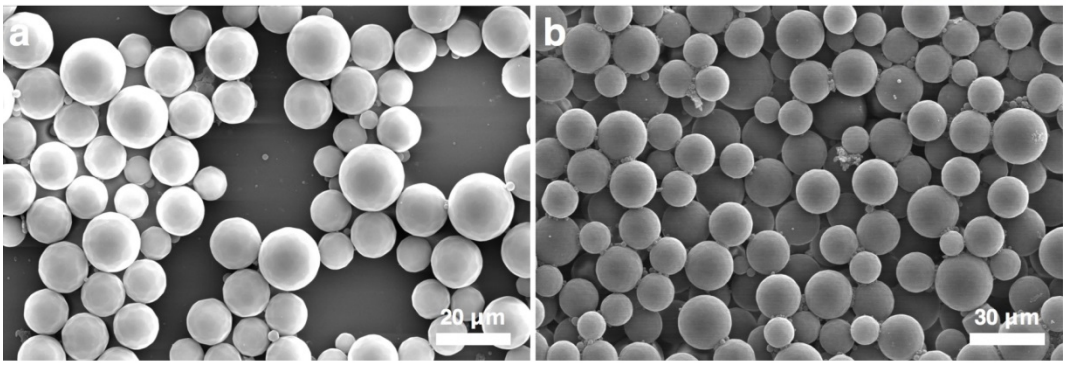

Figure 5-2. Low-magnification SEM images of polymer cubosomes of (a) $PEG550_3$-PS_{150} and (b) $PEG550_3$-PS_{168}.

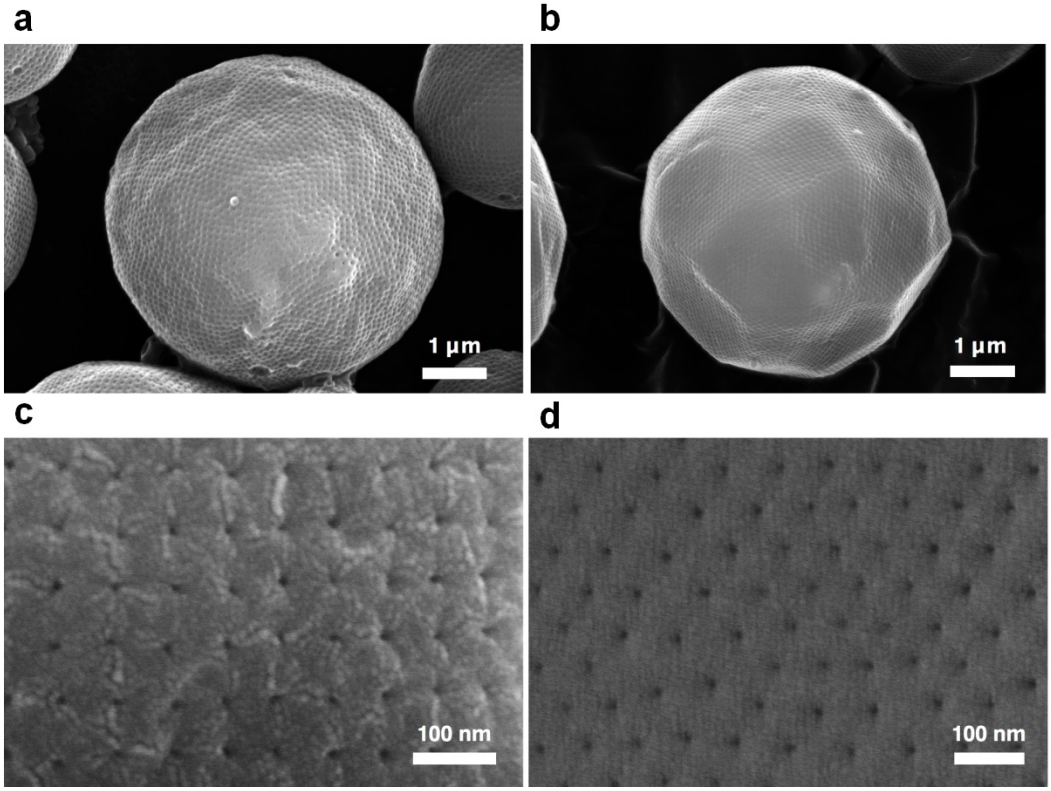

Figure 5-3. SEM images of polymer cubosomes of (a, c) $PEG550_3$-PS_{150} showing Schwarz P surface and (b, d) $PEG550_3$-PS_{168} showing Schwarz D surface.

We analyzed the topology of the BCP bilayer at the interface of the polymer cubosomes by SEM. Polymer cubosomes possessed perforated bilayer shells at the interface with water (Figure 5-3). The comparison between the computer-generated (100) plane of the lattice of the Schwarz P surface and the SEM image of the surface of the polymer cubosome of $PEG550_3$-PS_{150} indicated that, at the interface, only one simple cubic networks embedded in the Schwarz P surface remain accessible to the surrounding, leaving the other channel network closed (Figure 5-4). We measured the distance between two adjacent pores to estimate the surface topology of the P-type surface. The distance of the

adjacent pores was 65 ± 3 nm, and the diagonal distance of the tetragonal pores was 90 ± 4 nm. The fully open lattice of the Schwarz P surface (a = 60.7 nm) would have the adjacent and diagonal pore distances of 60.7 and 85.8 (60.7×$\sqrt{2}$) nm, respectively. The analysis of the SEM image of the topology of the perforated lamellar shell of the polymer cubosomes of $PEG550_3$-PS_{168} revealed the distance between the pores at the surface of the polymer cubosomes consisting of the Schwarz D surface was 71 ± 5 nm, which corresponded to the $\sqrt{2}a$ (63.9 nm), the diagonal distance of the pores of the (111) plane of the Schwarz D surface with one open channel.[22] This distance of the pores at the surface of the polymer cubosome indicated that the presence of a single open diamond cubic networks at the interface.

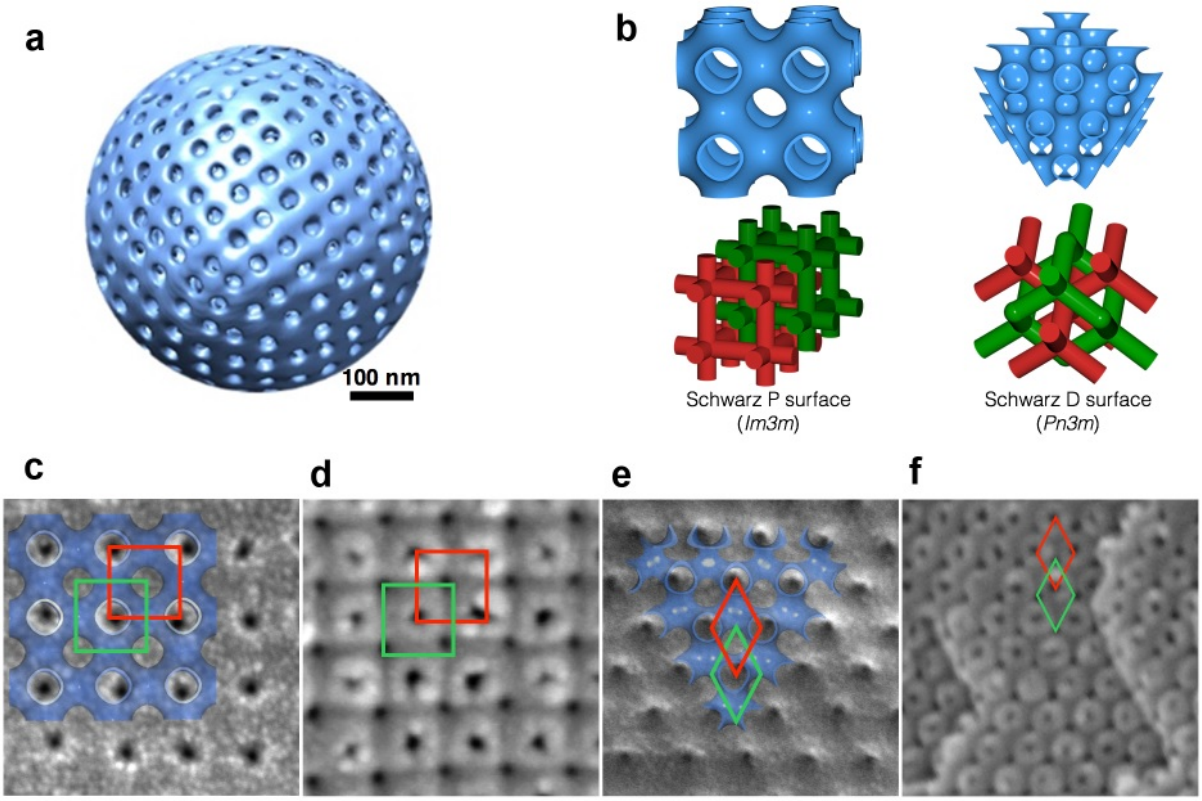

Figure 5-4. (a) Reconstructed 3D image of the polymer cubosome of $PEG550_3$-PS_{150}. (b) Schematic illustration of Schwarz P surface (*Im3m*, [100] direction) and Schwarz D surface (*Pn3m*, [111] direction). The red- and green-colored regions indicate two non-interpenetrating networks of water channels. (c-f) SEM images of the surface layer and internal structure of polymer cubosomes of (c, d) $PEG550_3$-PS_{150} and (e, f) $PEG550_3$-PS_{168}. Squares and diamonds indicate the open channels (red color) and closed channels (green color) to the surrounding.

To understand how the surface topology distinguishes diffusivity toward open and closed channel networks within polymer cubosomes, we used transmission electron microscope (TEM) tomography. Individual images of a dried polymer cubosome were taken by tilting the sample stage from –66 to

70° at the interval of 2°, which were aligned and reconstructed to generate the 3D tomogram of the polymer cubosome (Figure 5-4a). The surface topology obtained from the reconstructed 3D image of the polymer cubosome of $PEG550_3$-PS_{150} corroborated the SEM results by showing that the only one of two cubic channel networks remains open at the interface between the polymer cubosome and the surrounding. The closed channel network appeared beneath the surface layer, and two non-intersecting channel networks alternated along the direction pointing to the center of the polymer cubosome (Figure 5-5). The reconstructed 3D image of the internal cubic mesophases demonstrated the lattices of *Im3m* space group, coinciding with the results revealed by the SAXS experiments.

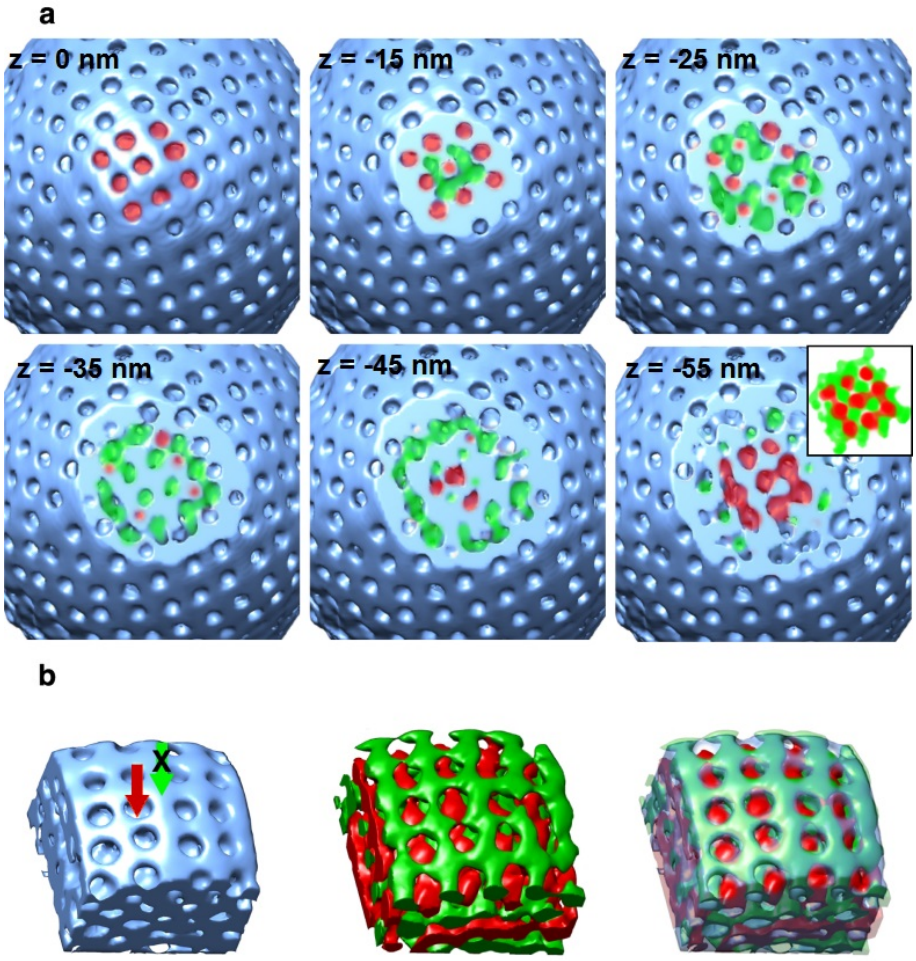

Figure 5-5. (a) Sequence of images extracted from the reconstructed 3D image of the polymer cubosome of $PEG550_3$-PS_{150} along the z direction. Red- and green-colored areas indicate the open and closed channel of the polymer cubosome. The inset shows merged image of two non-intersecting cubic channels. (b) Reconstructed 3D images of cutting plane of membranes (left), inverted image showing internal networks (middle), and merged image (right). The red arrows show the pore accessibility of the open channel.

To decipher the connectivity of the surface pores to the internal channel networks embedded within the BCP cubic mesophases, we mapped the 3D tomogram of the polymer cubosomes from the surface to the inside bicontinuous channel networks. The analysis of the occupied space TEM tomogram indicated that only one simple cubic network was able to be filled by the diffusion from the surface, suggesting that the topological distinction at the interface of the polymer cubosome force the external guest molecules preferentially enter into the open channel network (Figure 5-5). The TEM tomogram also showed that the perimeter of the polymer cubosomes having smaller diameter had more disordered mesophases compared to the larger polymer cubosomes because the compensation for the increased interfacial energy along the curved perimeter by the increase of entropy caused by the disorder of the lattices. We note that this disorder of the mesophases near the interface does not disrupt the connectivity between the surface pore and the internal channel networks.[16,22]

With these structural elucidations, we tested the accessibility of the open channel network of the polymer cubosomes by backfilling the polymer cubosomes with the solution of tetraethyl orthosilicate (TEOS) to replicate the internal channel network as an inorganic skeletal framework by sol-gel reaction.[26] The ethanol solution of TEOS and hydrochloric acid was introduced to the embedded channel network of the polymer cubosomes by placing a drop of TEOS solution, followed by removal of excess TEOS solution with a filter paper. The cross-linking of TEOS was carried out by placing the backfilled polymer cubosomes in the humidity chamber filled with HCl vapor for 14 h. The solvent-soluble BCP templates, then, were removed by immersing the cross-linked particles in tetrahydrofuran (THF) to avoid the isotropic shrinkage of the silica network during calcination. The ultracentrifugation of the remaining white power in a density-gradient medium was performed to remove large silica particles formed during the cross-linking.

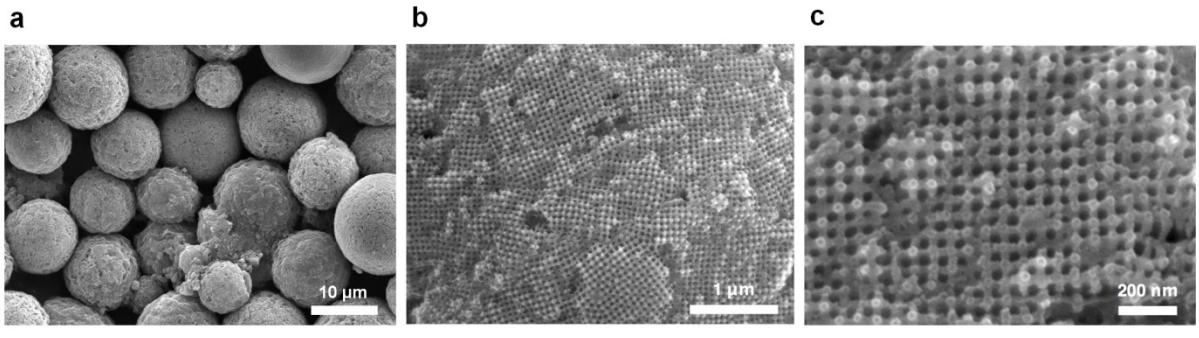

Figure 5-6. SEM images of the silica replica of the polymer cubosomes of $PEG550_3$-PS_{150}. (a) Low-magnification SEM image showing spherical SiO_2 particles. (b, c) High-magnification SEM images showing silica framework on the surface of the replicated structures.

The SEM images of the silica replica of the polymer cubosomes of $PEG550_3$-PS_{150} showed spherical morphology reflecting the shape of the polymer cubosome used as templates. (Figure 5-6).

The SEM and TEM images of the fractured particles revealed the silica framework having six-fold nodes, of which the structural symmetry was inherited from the primitive cubic lattice of the channel networks embedded in the polymer cubosome template. The SAXS results of the skeletal silica frameworks indicated that the lattice of the skeletal structure was transformed from primitive cubic double network (*Im3m* space group) to a single network of simple cubic lattice (*Pm3m* space group) (Figure 5-7). The lattice parameter of the single simple cubic network was 56.5 nm, which was nearly identical to the value of the polymer cubosome templates having *Im3m* symmetry (60.7 nm).[27] The silica replica of the channel network embedded in the polymer cubosome of $PEG550_3$-PS_{168} was also identified by SEM and TEM, which showed the skeletal frameworks having the nodes of four-fold symmetry. The SAXS peaks of the silica replica were assigned to a single diamond lattice (*Fd3m* space group) with the lattice parameter of 90.7 nm, a two-fold increase from the value (45.2 nm) of the double diamond lattice of the polymer cubosome template. The SEM and TEM images of the silica skeletal frameworks indicated that the resulting structure was indeed a single network having a simple cubic lattice instead of the double network structures that were overlapped by azimuthal shifting upon removal of the template (Figure 5-8).[28–30] Having identical structural symmetries to those of biophotonic structures of arthropod, these single skeletal frameworks of simple cubic and diamond lattices have not been synthesized by simple templated method of molecular precursors.

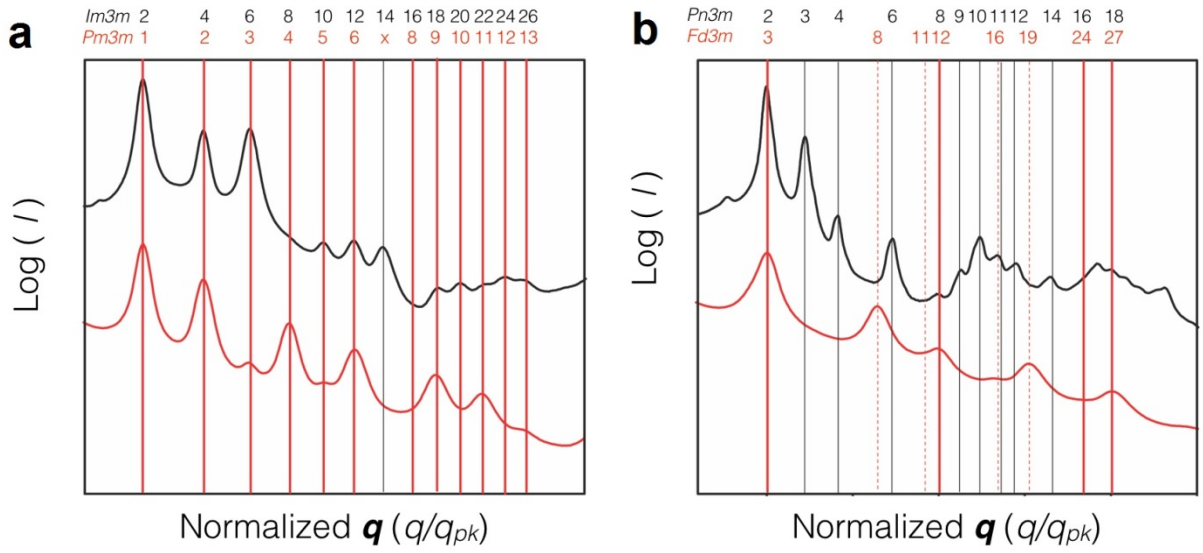

Figure 5-7. Normalized SAXS results of the polymer cubosomes (black line) and SiO_2 replicas (red line). (a) $PEG550_3$-PS_{150} (*Im3m*, a = 60.7 nm, *Pm3m*, a = 56.5 nm). (b) $PEG550_3$-PS_{168} (*Pn3m*, a = 45.2 nm, *Fd3m*, a = 90.7 nm). The colored lines correspond to the expected peak position for different space groups. The numbers above the graph are squares of the moduli of the Miller indices (*hkl*) for each space groups.

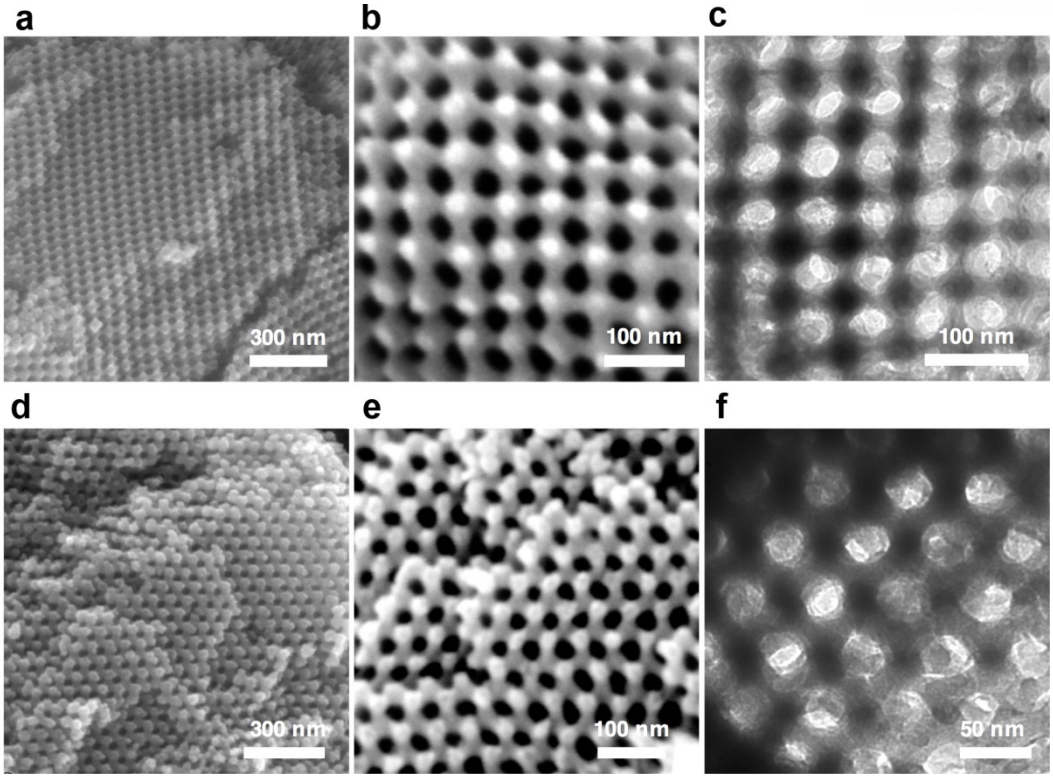

Figure 5-8. Electron micrographs of internal single networks of SiO_2 replicated from polymer cubosomes of $PEG550_3$-PS_n; (a-c) $PEG550_3$-PS_{150}, (d-f) $PEG550_3$-PS_{168}. (a, b) SEM and (c) TEM images showing a single network of simple cubic lattice having six-fold nodes. (d, e) SEM and (f) TEM images showing a single network of single diamond lattice having four-fold nodes.

The replication of the internal single diamond channel network with titanium tetraisopropoxide ($Ti(OiPr)_4$) was performed under acidic condition. The resulting skeletal titania having single diamond lattice was calcinated to form the frameworks composed of skeletons of anatase-form titania. The resulting anatase titania framework was characterized by SEM which confirmed the presence of single diamond network structures (Figure 5-9).

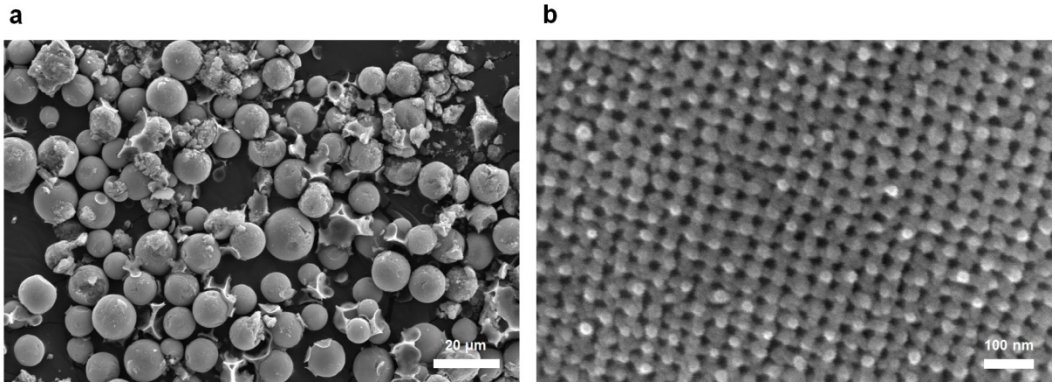

Figure 5-9. SEM images of TiO_2 frameworks replicated from the polymer cubosomes of $PEG550_3$-PS_{150}.

The skeletal single diamond networks of inorganic materials having high dielectric constants could develop omnidirectional full photonic bandgap in visible-light wavelengths if the lattice dimension is commensurate with the wavelength of the incident light. Unlike the OSER, lipid cubic mesophases and cubosomes exhibited lattice parameters smaller than the wavelength of visible light.[31] As the dimension of the polymer chain scales with the square-root of its molecular weight, the lattice parameter of the BCP cubic mesophases should be proportionally enlarged with increasing the molecular weights of the polymer blocks constituting the BCP.[22] Therefore, we are preparing the high molecular weight BCP, $PEG2000_3$-PS_n with anticipation of the increased lattice parameter of the Schwarz D surface comprising the polymer cubosomes.

5.4 Summary

In summary, we have shown that only one networks embedded in the minimal surfaces remain accessible to the surrounding, leaving the other channel network closed. The surface topology obtained from the reconstructed 3D image of polymer cubosomes indicated that this topological feature force the external guest molecules preferentially enter into the open channel network. By backfilling the polymer cubosomes with the silica and titania sol, we observed single framework structures (*Pm3m*, *Fd3m*) replicated from Schwarz P (*Im3m*) and Schwarz D (*Pn3m*) surfaces. The single framework structures having large lattice parameter could show structural color arising from the photonic bandgap, like butterfly scale cells. Recently, we are synthesizing the high molecular weight BCP, $PEG2000_3$-PS_n to create polymer cubosomes having large lattice parameter. Our polymer cubosomes may serve as the templates for the bio-inspired synthesis of single network cubic structures, which could lead to the creation of photonic crystals and metamaterials that are previously unavailable.

5.5 Experimental

General methods and materials. Unless otherwise noted, all reagents and chemicals were used as received from Sigma Aldrich and TCI. Tetrahydrofuran (THF) was refluxed over a mixture of Na and benzophenone under N_2 and distilled before use. All reactions were performed under N_2 unless otherwise noted. ^1H and ^{13}C NMR spectra were recorded on an Agilent 400-MR DD2 Magnetic Resonance System and Varian/Oxford As-500 using CD_2Cl_2 and $CDCl_3$ as solvents. Matrix-assisted laser desorption ionization time-of-flight mass spectroscopy (MALDI-TOF-MS) was performed on a Bruker Ultraflex III TOF-TOF mass spectrometer equipped with a nitrogen laser (335 nm). Scanning electron microscopy (SEM) was performed on a microscope and Hitachi S-4300 at an acceleration voltage of 15 kV. The samples were placed on a conductive carbon tape or silver paste and then coated with Pt with a thickness of 3 nm by using a Hitachi E-1030 ion sputter. Transmission electron

microscopy (TEM) was recorded on a JEOL JEM-2100 microscope at 200 kV. Specimens were prepared by placing a drop of the solution on a carbon-coated Cu grid (200 mesh, EM science). The grid was air-dried overnight. Electron-Tomography (ET) was obtained by JEM-1400 operating at 120 kV. The tilt series of projection images were reconstructed using weighted back-projection method as implemented in IMOD software. Synchrotron small angle X-ray scattering data were obtained on PLSII 6D at Pohang acceleration laboratory (Pohang, Korea).

Synthesis of branched macroinitiator with peripheral PEG chains

Branched macroinitiators were synthesized in multi-gram quantity by following the literature methods.[20]

550_3-Br. ^{1}H NMR (δ=ppm, 600 MHz, $CDCl_3$) 6.60 (s, 2H), 5.10 (s, 2H), 4.16 (t, 4H, *J* = 4.8Hz), 4.13 (t, 2H, *J* = 4.8Hz), 3.86-3.50 (m, -*CH_2CH_2O*-), 3.39 (m, 9H), 1.95 (s, 6H). ^{13}C NMR (δ=ppm, 150 MHz, $CDCl_3$) 171.2, 152.6, 140.1, 130.8, 107.4, 77.4, 77.1, 76.7, 70.8-70.3, 69.6, 69.6, 68.8, 67.4, 59.0, 55.8, 30.7. M_n (GPC) = 2380 g mol^{-1}, PDI = 1.03, M_n (MALDI-TOF) = 1972 g mol^{-1}.

Synthesis of block copolymers (550_3-PS_n).

CuBr (50 mg, 0.35 mmol) and *N,N,N',N'',N''*-pentamethyldiethylenetriamine (PMDETA) (108 mg, 0.525 mmol) were mixed with 1 mL of anisole in a 20 mL Schlenk tube with a magnetic bar. The tube was sealed with a rubber septum. This mixture was bubbled with N_2 for 15 min with gentle stirring. To this solution, the solution of styrene (10 mL) and 550_3-Br (120 mg, 0.035 mmol) was added via a syringe. The green solution was degassed by bubbling N_2 for 20 min. After degassing, the tube was immersed in a preheated oil bath (95 °C) and the polymerization was proceed at this temperature. The progress of polymerization was monitored by taking GPC at an interval of 1 h. When the molecular weight of the block copolymer reached to the desired value, the reaction was quenched by exposing the solution to air in an ice/water bath and diluted with $CHCl_3$ (15 mL). The cooled solution was filtered through a pack of aluminum oxide (basic) with $CHCl_3$ to remove the Cu catalyst. The filtered solution was concentrated on a rotary evaporator, and the resulting residue was diluted with 20 mL CH_2Cl_2. This solution was precipitated into methanol (200 mL). White powder was collected by vacuum filtration and dried in vacuo. All block copolymers were characterized by ^{1}H NMR and GPC to evaluate the molecular weight and the size distribution. The molecular characteristics of the block copolymers are listed in Table 4-1.

General procedure for self-assembly of 550_3-PSs into polymer cubosomes. The bPEG-PS was initially dissolved in 2 mL of a 1,4-dioxane/DMF mixture in a capped vial, and the solution was stirred for 3 h at room temperature. Water (total 2 mL) was added at a controlled rate (1 mL h^{-1}) to the solution with vigorous stirring (850 rpm). The resulting milky suspension was dialyzed (molecular weight cutoff (MWCO) = ~12-14 kDa, SpectraPor) against water for 24 h to remove the organic solvent.

Templated Synthesis of single networks. TEOS sol was prepared by mixing TEOS, ethanol, water and HCl (molar ratios: $1:3:1:5\times10^{-5}$) for 12h. The polymer cubosomes of $PEG550_3$-PS_{150} was placed on the filter paper. After adding a drop of TEOS solution to the polymer cubosomes, residual sol was quickly removed with a filter paper. The backfilled polymer cubosomes was placed in the humidity chamber filled with 5M HCl vapor for 14 h. The resulting powder immersed in THF. The block copolymers were removed from the suspension by repeated centrifugation and dilution with THF. The titania sol was prepared by adding 2 mL of titanium (IV) isopropoxide to a mixture of 1.6 mL of trifluoroacetic acid and 0.4 mL of hydrochloric acid while vigorously stirring. After 20 min, a drop of titania sol was added to the polymer cubosomes placed on the filter paper. Residual sol was quickly removed with a filter paper. The infiltrated polymer cubosomes was allowed to dry for 14 h. After drying, the sample was calcined in air at 500 °C for 5 h.

5.6 References

1. Maldovan, M.; Thomas, E. L. Diamond-Structured Photonic Crystals. *Nat. Mater.* **2004**, *3*, 593–600.
2. Dolan, J. A. et al. Optical Properties of Gyroid Structured Materials: from Photonic Crystals to Metamaterials. *Adv. Opt. Mater.* 2014, *3*, 12–32.
3. Ho, K. M.; Chan, C. T.; Soukoulis, C. M. Existence of a Photonic Gap in Periodic Dielectric Structures. *Phys. Rev. Lett.* **2990**, *65*, 3152–3155.
4. Maldovan, M.; Urbas, A. M.; Yufa, N.; Carter, W. C. ; Thomas, E. L. Photonic Properties of Bicontinuous Cubic Microphases. *Phy. Rev. B* **2002**, *65*, 165123.
5. Hynninen, A.-P.; Thijssen, J. H.; Vermolen, E. C. M.; Dijkstra, M.; van Blaaderen, A. Self-Assembly Route for Photonic Crystals with a Bandgap in the Visible Region. *Nat. Mater*. **2007**, *6*, 202-205.
6. Ducrot, É.; He, M.; Yi, G.-R.; Pine, D. J. Colloidal Alloys with Preassembled Clusters and Spheres. *Nat. Mater*. **2017**, *16*, 652–657.
7. Liu, W. *et al*. Diamond Family of Nanoparticle Superlattices. *Science* **2016**, *351*, 579–582.
8. Urbas, A. M.; Maldovan, M.; DeRege, P.; Thomas, E. L. Bicontinuous Cubic Block Copolymer Photonic crystals. *Adv. Mater.* **2002**, *14*, 1850–1853.

9. Hur, K. et al. Three-Dimensionally Isotropic Negative Refractive Index Materials from Block Copolymer Self-Assembled Chiral Gyroid Networks. *Angew. Chem. Int. Ed.* **2011**, *50*, 11985–11989.
10. Vukusic, P.; Sambles, J. R. Photonic Structures in Biology. *Nature* **2003**, *424*, 852–855.
11. Saranathan, V. *et al.* Structure, Function, and Self-Assembly of Single Network Gyroid ($I4_132$) Photonic Crystals in Butterfly Wing Scales. *Proc. Natl. Acad. Sci. U. S. A.* **2010**, *107*, 11676–11681.
12. Saranathan, V. *et al.* Structural Diversity of Arthropod Biophotonic Nanostructures Spans Amphiphilic Phase-Space. *Nano Lett.* **2015**, *15*, 3735–3742.
13. Almsherqi, Z. A.; Kohlwein, S. D.; Deng, Y. Cubic Membranes: a Legend Beyond the Flatland of Cell Membrane Organization. *J. Cell Biol.* **2006**, *173*, 839–844.
14. Borgese, N.; Francolini, M.; Snapp, E. Endoplasmic Reticulum Architecture: Structures in Flux. *Curr. Opin. Cell Biol.* **2006**, *18*, 358–364.
15. Larsson, K. Cubic Lipid-Water Phases: Structures and Biomembrane Aspects. *J. Phys. Chem.* **1989**, *93*, 7304–7314.
16. Gustafsson, M.; Ljusberg-Wharen, H.; Almgren, M.; Larsson, K. Submicron Particles of Reversed Lipid Phases in Water Stabilized by a Nonionic Amphiphilic Polymer. *Langmuir* **1997**, *13*, 6964–6971.
17. Demurtas, D. *et. al.* Direct Visualization of Dispersed Lipid Bicontinuous Cubic Phases by Cryo-Electron Tomography. *Nat. Commun.* **2015**, *6*, 8915.
18. Rittman, M.; Frischherz, M.; Burgmann, F.; Hartley, P. G.; Squires, A. Direct visualization of lipid bilayer cubic phases using atomic force microscopy. *Soft Matter* **2010**, *6*, 4058–4061.
19. Góźdź, W. T. Cubosome Topologies at Various Particle Sizes and Crystallographic Symmetries. *Langmuir* **2015**, *31*, 13321–13326.
20. An, T. H. *et al*. Solution Self-assembly of Block Copolymers Containing a Branched Hydrophilic Block into Inverse Bicontinuous Cubic Mesophases. *ACS Nano* **2015**, *9*, 3084–3096.
21. La, Y. *et al.* Colloidal Inverse Bicontinuous Cubic Membranes of Block Copolymers with Tunable Surface Functional Groups. *Nat. Chem.* **2014**, *6*, 534–541.
22. Cho, A.; La, Y.; Shin, T. J.; Park, C.; Kim, K. T. Structural Requirements of Block Copolymers for Self-assembly into Inverse Bicontinuous Cubic Mesophases in Solution. *Macromolecules* **2016**, *49*, 4510–4519.
23. Martín-Moreno, L.; García-Vidal, F. J.; Somoza, A. M. Self-Assembled Triply Periodic Minimal Surfaces as Molds for Photonic Band Gap Materials. *Phys. Rev. Lett.* **1999**, *83*, 73–75.
24. Nykypanchuk, D.; Maye, M. M.; van der Lelle, D.; Gang, O. DNA-Guided Crystallization of Colloidal Nanoparticles. *Nature* **2008**, *451*, 549–552.

25. Zeng, D.; Ribbe, A.; Hayward, R. C. Anisotropic and Interconnected Nanoporous Materials from Randomly End-Linked Copolymer Networks. *Macromolecules* **2017**, *50*, 4668–4678.
26. Park, C. *et al.* Mesoporous Monoliths of Inverse Bicontinuous Vubic Phases of Block Vopolymer Bilayers. *Nat. Commun.* **2015**, *6*, 6392.
27. Finnefrock, A. C.; Ulrich, R.; Toombes, G. E. S.; Gruner, S. M.; Wiesner, U. The Plumber's Nightmare: a New Morphology in Block Copolymer–Ceramic Nanocomposites and Mesoporous Aluminosilicates. *J. Am. Chem. Soc.* **2003**, *125*, 13084–13039.
28. Li, H.; Liu, Y.; Cao, X.; Han, L.; Jiang, C.; Che, S. A Shifted Double-Diamond Titania Scaffold. *Angew. Chem. Int. Ed.* **2017**, *56*, 806–811.
29. Mao, W.; Cao, X.; Sheng, Q.; Han, L.; Che, S. Silica Scaffold with Shifted "Plumber's Nightmare' Network and their Interconversion into Diamond Networks. *Angew. Chem. Int. Ed.* **2017**, *56*, 10670–10675.
30. Han, L. *et al.* Synthesis and Characterization of Macroporous Photonic Structure that Consists of Azimuthally Shifted Double-Diamond Dilica Frameworks. *Chem. Mater.* 2014, *26*, 7020–7028.
31. Barriga, H. M. G. et al. Temperature and Pressure Tunable Swollen Bicontinuous Cubic Phases Approaching Nature's Length Scales. *Soft Matter* **2014**, *11*, 600–607.

Acknowledgement

First of all, I would like to thank Prof. Kyoung Taek Kim for his generous support and trust on me in graduate school. His cheering and encouragement became a great energy whenever I had difficulties. It is great honor for me to be a Ph.D. student under his group in UNIST and Seoul National University.

I appreciate to Prof. Ja-Hyoung Ryu for his kind support as a supervisor in UNIST after I move to Seoul. Our discussions made me think more about my research and future works. I would like to thank all thesis committee members, Prof. Hoi Ri Moon, Prof. Sung You Hong, and Prof. Young S. Park, for reading my thesis and giving great comments.

Thanks to a number of people in UNIST and SNU. Hyunkyu Kim and Prof. Chiyoung Park transferred their enormous knowledges to me as a senior. Jae Yeong Cheon, my roommate and mentor, always helped me. Their supports in UNIST should be acknowledged. I also thank our lab members in UNIST (Eun Sun Jeong, Arah Cho, Moon Gon Jeong, Tae Hyun An, So Ryoung Lim) and SNU (Ji Won Kim, Jeong Eun Song, Hyun ji Ma, Chae Eun Lee, Yong Beom Kwon, Mi sun Yoon, Jun Young Kim, Sung Min Ha, Jeong Min Lee, Sul Woo Lee, Hee Lim Lee, Yu Lin Sun). I will never forget our precious time in laboratory and relationship.

Finally, I would like to thank my family. Very special thanks to my parents, for always believing and supporting me. Also, my sister’s advice was a great help during my doctoral studies.

Thank you again for all those who have supported me.